

VESICAL Part II: A critical approach to volatile solubility modelling using an open-source Python3 engine

P. E. Wieser^{1,2*}, K. Iacovino³, S. Matthews⁴, G. Moore³, C. M. Allison^{5,6}

¹Department of Earth Sciences, University of Cambridge, UK.

²College of Earth, Ocean and Atmospheric sciences, Oregon State University

³Jacobs, NASA Johnson Space Center, Houston, TX 77058, USA.

⁴Johns Hopkins University, Department of Earth and Planetary Sciences, Baltimore, MD 21218, USA.

⁵Cornell University, Department of Earth and Atmospheric Sciences, Ithaca, NY 14853

⁶City College of New York, City University of New York, New York, NY 10031

Key Points:

- The open-source Python3 tool VESICAL allows extensive comparisons to be drawn between different H₂O-CO₂ solubility models
- The P-T-X calibration range of each solubility model must be critically evaluated for the P-T-X conditions of interest
- Changes in solubility with melt composition should be accounted for by calculating a saturation pressure for each individual melt inclusion.

Abstract

Accurate models of H₂O and CO₂ solubility in silicate melts are vital for understanding volcanic plumbing systems. These models are used to estimate the depths of magma storage regions from melt inclusion volatile contents, investigate the role of volatile exsolution as a driver of volcanic eruptions, and track the degassing paths followed by magma ascending to the surface. However, despite the large increase in the number of experimental constraints over the last two decades, many recent studies still utilize the earlier generation of models, which were calibrated on experimental datasets with restricted compositional variations. This may be because many of the calculation tools for more recent models require large numbers of input parameters to be hand-typed (e.g., P, T, volatile contents, 8-14 oxide components for each calculation), making them difficult to implement on large datasets. Here, we use a new open-source Python3 tool, VESIcal, to critically evaluate the behaviours and sensitivities of different solubility models for a range of melt compositions. Using literature datasets of andesitic-dacitic experimental products and melt inclusions as case studies, we illustrate the importance of evaluating the calibration dataset of each model. We also show that popular isobar diagrams are a flawed way to visualize saturation pressures for melt inclusion populations with diverse major element contents, and instead suggest that VESIcal is used to calculate a saturation pressure for each individual melt inclusion. This review will aid the selection of the most applicable solubility model for different melt compositions, and identifies areas where additional experimental constraints are required (242/250 words)

Plain Language Summary

Being able to accurately model the solubility of H₂O and CO₂ in magmas is very important for understanding a wide variety of volcanic processes, such as the depths at which magma is stored in the crust, the driving force behind volcanic eruptions, and the release of volatile elements into the atmosphere. However, there has been no easy way for volcanologists to perform calculations on large datasets, or to compare different models. This review uses a new, open-source tool called VESIcal written in the popular programming language Python3. This allows us to compare different models for a wide variety of melt compositions, temperatures and pressures, helping researchers to identify the most suitable model for their study. We also suggest areas where further experimental constraints are required. Finally, we highlight the limitations of particular data presentation methods such as isobar diagrams, and provide suggestions for alternatives, and best practices regarding the presentation and archiving of data.

1 Introduction

The most abundant volatile components found in terrestrial magmatic systems are H₂O and CO₂. It has been known for nearly a century (Bowen, 1928; Tuttle & Bowen, 1958) that these volatile species have profound effects on the chemical and material properties of magmas (e.g., phase equilibria, melting temperatures, magma viscosity and density; Burnham, 1979; Husen et al., 2016; Burnham & Davis, 1974; Hess & Dingwell, 1996; Ochs & Lange, 1999), and thus significantly affect their geochemical and dynamical behavior (e.g., eruption and degassing style, erupted volume; Papale et al., 1999; Huppert & Woods, 2002). Thus, it is vital to be able to predict how H₂O and CO₂ solubilities change as a function of intensive variables such as pressure, temperature, melt and fluid composition in order to understand plutonic and volcanic systems.

The solubility of a volatile species is defined at a given pressure and temperature as the maximum concentration of that volatile that can be dissolved within a silicate melt of a specified composition. Ignoring disequilibrium effects, if the volatile content of the system exceeds this solubility limit, a separate fluid/vapour phase will exsolve from the magma. In this review, we favour the term fluid because of the supercritical nature of exsolved volatile phases at magmatic temperatures. In general terms, a magma is described as volatile undersaturated when there is no fluid phase, and volatile saturated once a fluid phase is present (also referred to as vapour undersaturated/saturated, or fluid undersaturated/saturated). In detail, different volatile species do not act as independent entities, but influence one another. For this reason, a magma may exsolve a mixed CO₂-H₂O fluid even if the dissolved concentrations of H₂O and CO₂ do not exceed the pure solubility limit of each species.

Despite the obvious importance of accurate volatile solubility modelling, very few studies on volcanic systems have evaluated results using several different solubility models to determine possible sources of systematic and random error, and assess the suitability of each model for the conditions of interest (e.g. temperature, pressure, and melt composition). This lack of intercomparison likely results from the fact that it is extremely time consuming to perform lots of comparisons using available calculation tools. For example, many solubility models were released as stand-alone excel spreadsheets (e.g., G. Moore et al., 1998; Newman & Lowenstern, 2002; Allison et al., 2019) or web apps (e.g., Iacono-Marziano et al., 2012; Ghiorso & Gualda, 2015), where saturation pressures, dissolved volatile contents, degassing paths, and isobars must be calculated for one sample and set of conditions at a time. The more recent models which include complex terms accounting for the effect of melt composition on volatile solubility require users to hand-type a large number of input parameters. For example, to calculate a saturation pressure in MagmaSat (Ghiorso & Gualda, 2015), users must hand-type 9–14 oxide concentrations in addition to entering H₂O and CO₂ concentrations, and a melt temperature.

81 Similarly, the Iacono-Marziano web app (Iacono-Marziano et al., 2012) requires users to input 8 major
82 element oxide concentrations. Calculating isobars using these web apps is a particularly daunting task,
83 as users must evaluate dissolved volatile contents at multiple fluid compositions, and then use curve
84 fitting to produce a smooth isobar to display on plots. Other models were released with no calculator
85 at all, requiring each user to correctly interpret and combine the relevant equations in the manuscript
86 (Dixon, 1997; Shishkina et al., 2014).

87 Here, we take advantage of the recent release of VESIcal (Volatile Equilibria and Saturation
88 Identification calculator; Iacovino et al., 2021), an open-source tool written in Python3. VESIcal con-
89 tains functions to calculate saturation pressures, dissolved volatile contents, isobars, and degassing
90 paths automatically for seven different models. Calculations can be performed based on melt com-
91 positions provided in an excel spreadsheet, and users can take full advantage of Python's extensive
92 flexibility to perform large numbers of calculations automatically (e.g., creating for loops to perform
93 calculations across a range of pressures, temperatures, and fluid compositions). To our knowledge,
94 the only other model with similar functionality to VESIcal is the Linux program Solwcad supplied by
95 Papale et al. (2006), which performs calculations automatically on a user-supplied .txt file containing
96 melt compositions, pressures and temperatures (<http://www.pi.ingv.it/progetti/eurovolc/>).
97 This program was used alongside VESIcal in this review, through the Windows Subsystem for Linux
98 (WSL2).

99 The overall aim of this review is to summarize the formulation, strengths and weaknesses of pop-
100 ular solubility models to inform users who wish to model volatile solubility in silicate melts, whether
101 that be the calculation of melt inclusion saturation pressures, degassing paths, incorporating volatile
102 exsolution in physical model of magma chambers (e.g. Huber et al., 2019), or calculating the dissolved
103 volatile contents of experimental products where the pressure, temperature and fluid composition are
104 known (e.g. Waters & Lange, 2015). We start by briefly summarizing the major results from volatile
105 solubility experiments over the last century (section 2, before describing nine of the most popular sol-
106 ubility models (section 3). We then compare the solubility of pure H₂O, mixed H₂O-CO₂, and pure
107 CO₂ predicted by different models for representative mafic and silicic compositions (section 4). We
108 also explore the sensitivity of these models to parameters such as temperature and redox state, which
109 are often uncertain when modelling igneous systems (section 5). Finally, we evaluate the suitability of
110 these models for intermediate melt compositions, where experimental constraints are sparse relative to
111 basaltic and rhyolitic melts (section 6). We conclude by discussing best practices for presenting and
112 archiving data related to volatile components in igneous systems (section 7). The aim of this review
113 is to give readers an insight into the strengths and weaknesses of different models, as well as the large

114 systematic errors associated with model choice. This will help users of VESIcal and other automated
115 tools select an appropriate model for their specific application. All the python code used to perform
116 these comparisons is provided in the supporting material, which users can easily adapt to evaluate
117 melt compositions for their specific application.

118 **2 Major findings from experimental studies investigating volatile solubility in** 119 **magmas**

120 One of the earliest volatile studies was that of Goranson (1931), who investigated the effect of
121 pressure on the solubility of water in granitic melts. The classic treatise of Tuttle and Bowen (1958)
122 investigated the impact of H₂O on mineral phase equilibrium. This study led to a wider recognition
123 of the importance of volatiles, and motivated the development of both the experimental and analyt-
124 ical approaches to determining volatile solubilities as a function of pressure, temperature, and melt
125 composition. Hamilton et al. (1964) was one of the first to compare H₂O solubilities for differing melt
126 compositions (basalt and andesite), while also investigating the effect of dissolved H₂O and oxidation
127 state on the magmatic phase equilibria. These studies were followed by the fundamental experimen-
128 tal measurements of the Burnham group on the dissolution of H₂O in albite melts (e.g., Burnham &
129 Davis, 1971, 1974).

130 Further investigation of volatile solubility over the next four decades in natural samples and
131 experimental products was aided significantly by analytical developments, allowing volatile contents
132 in quenched glasses to be measured by techniques such as Fourier Transform infra-red spectroscopy
133 (FTIR; e.g., Stolper, 1982; Fine & Stolper, 1986; Silver et al., 1990) and secondary ion mass spectrom-
134 etry (SIMS; Hervig & Williams, 1988; Hauri, 2002). In particular, the high spatial resolution of FTIR
135 and SIMS (a few tens of micrometers) meant that volatile concentrations could be measured within
136 quenched pockets of melt trapped within crystals (termed melt inclusions). Unlike subaerially-erupted
137 lavas which have degassed almost all their H₂O and CO₂ following their ascent to shallow pressures,
138 melt inclusions remain pressurized during ascent as they are trapped in relatively incompatible crys-
139 tals, so retain high volatile contents.

140 Melt inclusion analyses have greatly advanced our understanding of the behavior of volatiles in
141 volcanic systems (Lowenstern, 2003; Hauri et al., 2002; Roggensack, 2001; Wallace et al., 1995; Métrich
142 & Wallace, 2008; Sides et al., 2014a). For example, melt inclusions provide insights into pre-eruptive
143 volatile contents (e.g., Saal et al., 2002; Hervig et al., 1989), and links between melt volatile contents
144 and eruption styles (Lucic et al., 2016). The strong pressure-dependence on volatile solubility means
145 that H₂O and CO₂ contents within melt inclusions trapped from a volatile-saturated magma can be
146 used to determine the pressure at which the inclusion was trapped (termed the saturation pressure or

147 entrapment pressure). In turn, the distribution of saturation pressures in a suite of melt inclusions can
148 reveal the locations of the main regions of magma storage in a volcanic system. This explosion of new
149 information from melt inclusions greatly increased the demand for flexible and accurate solubilities
150 models that could be applied to a broad range of pressures, temperatures, and melt/fluid compositions
151 (G. Moore, 2008; Ghiorso & Gualda, 2015).

152 It has become increasingly apparent from solubility experiments that while the solubility of H₂O
153 is reasonably insensitive to melt composition (e.g., G. Moore & Carmichael, 1998; Shishkina et al.,
154 2010), CO₂ solubility in mafic magmas is highly sensitive to melt composition, particularly in mafic
155 melts where the carbonate ion is the dominant species (Dixon, 1997; Brooker et al., 2001; Shishkina
156 et al., 2010; Iacono-Marziano et al., 2012; Shishkina et al., 2014; Allison et al., 2019). This has led to
157 a great diversity in how various models treat the dependence of melt composition on CO₂ solubility.
158 In general, these models have become more complex with time as the region of compositional space
159 spanned by solubility experiments has increased to include more alkaline lavas. The individual role and
160 relative importance of each cation species in the melt is still associated with a large degree of uncer-
161 tainty (Allison et al., 2019), accounting for the larger discrepancies between model predictions for CO₂
162 vs. H₂O.

163 Experimental work has also highlighted the complexities of mixing between H₂O and CO₂ in
164 igneous systems. In the simplest case, the addition of one component in a melt-fluid system decreases
165 the activity, and therefore the solubility of the other component in the melt (Lowenstern, 2001). This
166 behavior is described by Henry's law, and is referred to as Henrian/ideal behavior. Henry's Law states
167 that the amount of a volatile dissolved in a liquid is proportional to its partial pressure in the gas
168 phase in equilibrium with that liquid. Neglecting the possible entropic effects of speciation, the addi-
169 tion of H₂O to the fluid/gas phase acts to lower the partial pressure of CO₂, and therefore lowers the
170 solubility of CO₂ in the liquid. Similarly, addition of CO₂ to the fluid/gas phase causes the solubility
171 of H₂O in the melt to decrease.

172 Experimental studies have shown that Henry's law is generally obeyed at low pressures (<1
173 kbar) in basaltic (Dixon et al., 1995) and rhyolitic melts (Blank et al., 1993). However, at higher pres-
174 sures, some experimental observations have shown that the mixing behavior of CO₂ and H₂O becomes
175 strongly non-henrian (Papale, 1999). For example, Eggler (1973), Mysen et al. (1976) and Mysen
176 (1976) show that the solubility of CO₂ in albitic melts increases with the addition of H₂O at higher
177 pressures. This has been attributed to the fact that the addition of small amounts of water as OH⁻
178 species decreases melt polymerization, and therefore enhances the solubility of CO₂ relative to an en-
179 tirely anhydrous melt. After a certain amount of H₂O is added, solubility decreases once more because

180 the addition of H₂O to the fluid phase causes the fugacity of CO₂ to decrease (Mysen, 1976; Dingwell,
181 1986; King & Holloway, 2002). More recently, this behavior has been demonstrated for dacitic and
182 rhyolitic melts by Behrens et al. (2004) and Liu et al. (2005).

183 The non-ideal behavior of H₂O and CO₂ in basaltic and andesitic melts at higher pressures is
184 less well constrained. King and Holloway (2002) show that at 1 kbar, andesitic melts (SiO₂=58.4 wt%)
185 exhibit a sharp increase in the solubility of CO₃²⁻ species with increasing melt H₂O contents between
186 0–3.39 wt%. In contrast, Jakobsson (1997) show that the solubility of CO₂ in an icelanditic melt (54.6
187 wt% SiO₂) at 10 kbar is essentially constant, despite variation in melt water contents between ~1–9
188 wt%. Similar behaviour to that observed by Jakobsson (1997) was noted for andesitic magmas (57.4
189 wt% SiO₂) at 5 kbar by Botcharnikov et al. (2006), who suggest that differences between H₂O-CO₂
190 mixing in their experiments and those of King and Holloway (2002) may result from differences in
191 oxygen fugacity of these experiments (Fe³⁺/Fe_T=0.2–0.6 vs. Fe³⁺/Fe_T=0.09–0.2). However, as we
192 discuss in section 4.1, the influence of oxygen fugacity on volatile solubility is still poorly constrained.
193 Recent basaltic H₂O-CO₂ experiments generally show a relatively flat plateau for CO₂ solubility with
194 increasing melt H₂O contents between ~0–4 wt% (Iacono-Marziano et al., 2012; Shishkina et al., 2010,
195 2014), although relatively large error bars on analyses of CO₂ in experimental products make it diffi-
196 cult to determine whether this plateau is truly flat, or shows a slight positive or negative gradient at
197 low H₂O contents (see Fig. 7a of Iacono-Marziano et al., 2012). The effect of H₂O-CO₂ mixing in the
198 9 solubility models evaluated here is discussed further in sections 4.2.2 and 4.3.2.

199 **3 Models discussed in this review**

200 In this review, we focus on the seven models implemented in VESIcal:

- 201 1. The simplified parameterization of the Dixon (1997) model for H₂O and CO₂, which was imple-
202 mented in the popular tool VolatileCalc (Newman & Lowenstern, 2002), hereafter VolatileCalc-
203 Basalt.
- 204 2. The H₂O model of G. Moore et al. (1998), hereafter M-1998.
- 205 3. The H₂O and CO₂ models of Liu et al. (2005), hereafter L-2005.
- 206 4. The H₂O and CO₂ models of Iacono-Marziano et al. (2012), hereafter IM-2012.
- 207 5. The H₂O and CO₂ models of Shishkina et al. (2014), hereafter S-2014.
- 208 6. The combined H₂O and CO₂ model of Ghiorso and Gualda (2015), hereafter MagmaSat.
- 209 7. The CO₂ models of Allison et al. (2019), hereafter A-2019.

210 We also consider the two additional models, reflecting both their popularity and relative ease of calcu-
211 lation using previously published tools:

212 8. The combined H₂O and CO₂ model of Papale et al. (2006), hereafter P-2006, accessed using the
213 Linux program solwcad.

214 9. The Rhyolite functions in the VolatileCalc spreadsheet, hereafter VolatileCalc-Rhyolite

215 We do not consider the models of X. Duan (2014), Eguchi and Dasgupta (2018), Burgisser et al.
216 (2015) because no tool exists to automate the necessary calculations. We also do not discuss mod-
217 els with more limited pressure (P), temperature (T) or compositional (X) ranges.

218 A summary table of the P, T and X range covered by the calibration dataset of each of the 9
219 models evaluated, as well as available tools to perform calculations, is provided in Fig. 1. The calibra-
220 tion dataset of each model is shown on a total alkali-silica diagram in Fig. 2. Detailed descriptions of
221 each model are provided below.

| Publication | Volatile | Speciation | P (bar) | T (°C) | Compositional range | Formulation | Redox sensitive? (No input FeO ₂) | Available Tools | Notes |
|-------------------------------------|---|---|---|---|---|---|---|---|-------|
| Moore et al., 1989 | H ₂ O | 0-3000 ¹ | 700-1200 ² | Broad compositional ranges: subalkaline basalts to rhyolites, alkaline trachybasalts-andesites, foidites, phonolites | Thermodynamic basis, Empirical effect of melt composition | No (input SiO ₂ only) ² | Macro-enabled Excel spreadsheet supplied by authors Pytho3 code (VESKcal; Iacono et al. 2021) | Auto-suggested calibration range: 1300 to 6067 bar and 800-1200 °C | |
| Newman and Lowenstein (2002) | H ₂ O CO ₂ | H ₂ O as OH and H ₂ O _{total} CO ₂ as CO ₂ ² | 0-5000 ¹ 0-2000 ² 0-1000 ³ | Alkali basalts: 40-49 wt% SiO ₂ | Thermodynamic basis, Empirical effect of melt composition | No (input SiO ₂ only) ² | Macro-enabled Excel (VolatCalc; Newman and Lowenstein, 2002) Pytho3 code, at 2020 Pytho3 code and web application (VESKcal; Iacono et al. 2021) | Warnings implemented in VolatCalc (Newman and Lowenstein, 2002): 1. Calibration range suggested by Lesne et al. (2011) 2. Calibration range suggested by Iacono-Marziano et al. (2012) 3. Calibration temperature of 1200 °C (different proportions of FeO and Fe ₂ O ₃ will slightly change the normalized SiO ₂ content) | |
| Newman and Lowenstein (2002) | H ₂ O CO ₂ | H ₂ O as OH and H ₂ O _{total} | 0-5000 ¹ | Rhyolites | Thermodynamic basis, no compositional term | No | Macro-enabled Excel spreadsheet (VolatCalc; Newman and Lowenstein, 2002) | Calibration range was not implemented in VolatCalc (Newman and Lowenstein, 2002). | |
| Liu et al. 2005 | H ₂ O CO ₂ | 0-5000 ¹ | 700-1200 ² | Haplogranites and rhyolites | Empirical basis, no compositional term | No | Pytho3 code (VESKcal; Iacono et al. 2021) | Auto-suggested calibration range for the mixed fluid model: The Carbon model, and 1-5000 bar and 700-1200 °C for the water model | |
| Papale et al. (2006) | H ₂ O CO ₂ | 0-10,000 ¹ | -630-1630 ² | Broad compositional range (SiO ₂ =37-85 wt%); poor coverage of CO ₂ and CO-H ₂ O fluids. Poor coverage of intermediate compositions (SiO ₂ =55-75 wt%). | Fully thermodynamic formulation for effect of melt composition | Yes (input FeO and Fe ₂ O ₃) | Web application (Link: http://www.earth.berkeley.edu/~papale/geochem/geochem.html) source code (SQUAD, Iacono et al. 2021) | Interpretation of H ₂ O-CO ₂ fields on Fig. 10 of Papale (1999) | |
| Iacono-Marziano et al., 2012 | H ₂ O CO ₂ | 100-10000 (mostly <5000) ¹ | 1100-1400 (preferably 1200-1300) ² | Predominantly mafic compositions: subalkaline and alkaline basalts-andesites | Thermodynamic basis, Empirical effect of melt composition | No (input FeO ₂) | Web application (http://www.earth.berkeley.edu/~iacono/geochem/geochem.html) Pytho3 code (VESKcal; Iacono et al. 2021) | Range of calibration dataset, as authors do not state a range. We note that the vast majority of experiments were conducted at 1200-1300 °C (whole range 1100-1600 °C). ?Authors state that most experiments were conducted between 1200-1300 °C (whole range 1100-1600 °C). | |
| Shishkina et al. 2014 | H ₂ O CO ₂ ¹ | 0-5000 ² | 1050-1400 (preferably 1150-1250) ³ | Mafic and intermediate compositions: subalkaline-phonolites, SiO ₂ =65 wt%. Predominantly mafic compositions: subalkaline basalts, alkaline basalts, trachybasalts | Fully empirical formulation for effect of melt composition | Only for CO ₂ (input Fe ²⁺) Calibrated with Fe=Fe ²⁺ | Pytho3 code (VESKcal; Iacono et al. 2021) | Although these empirical compositions are for pure fluids, they were mostly calibrated on mixed CO ₂ -H ₂ O experiments. ?Note, this model contains no temperature term. | |
| MagmaSat (Ghiorso and Guadri, 2015) | H ₂ O CO ₂ H ₂ O-CO ₂ | H ₂ O: as OH CO ₂ as CO ₂ and CO _{total} | 550-1420 ¹ 1139-400 ² 800-1400 ³ | Very broad compositional range of natural silicate melt compositions: subalkaline picodals-rhyolites, wide variety of mafic-silicic alkaline compositions | Fully thermodynamic formulation for effect of melt composition | Yes (input FeO and Fe ₂ O ₃) | Web application (http://www.earth.berkeley.edu/~ghiorso/magsat/) Pytho3 code (MagmaSat; Iacono et al. 2021) | Ranges extracted from Fig. 2d of Ghiorso and Guadri, 2015 | |
| Allison et al., 2019 | CO ₂ ¹ | 0-7000 ² | 1200 ³ (-1000-1400) | Alkali-rich mafic magmas from 6 volcanic fields (San Francisco Volcanic Field, Sunset Crater, Erebus, Vesuvius, Etna, Stromboli). Separate model coefficients for each composition. | Thermodynamic basis, separate parameters for each of 6 melt compositions. | No | Pytho3 code (VESKcal; Iacono et al. 2021) | Although this model is for pure CO ₂ , it was calibrated on mixed CO ₂ -H ₂ O experiments. ?Auto-suggested range: The calibration dataset spans: 4078-6175 bar, Vesuvius; 269-6175 bar, Etna; 485-6190 bar, Stromboli; 524-6080 bar. ?Note, all calculations and experiments were performed at 1200 °C. ?Authors suggest applicable between 1000-1400 °C. | |

Figure 1. Table summarizing the calibration range of each model, as well as available tools to perform calculations.

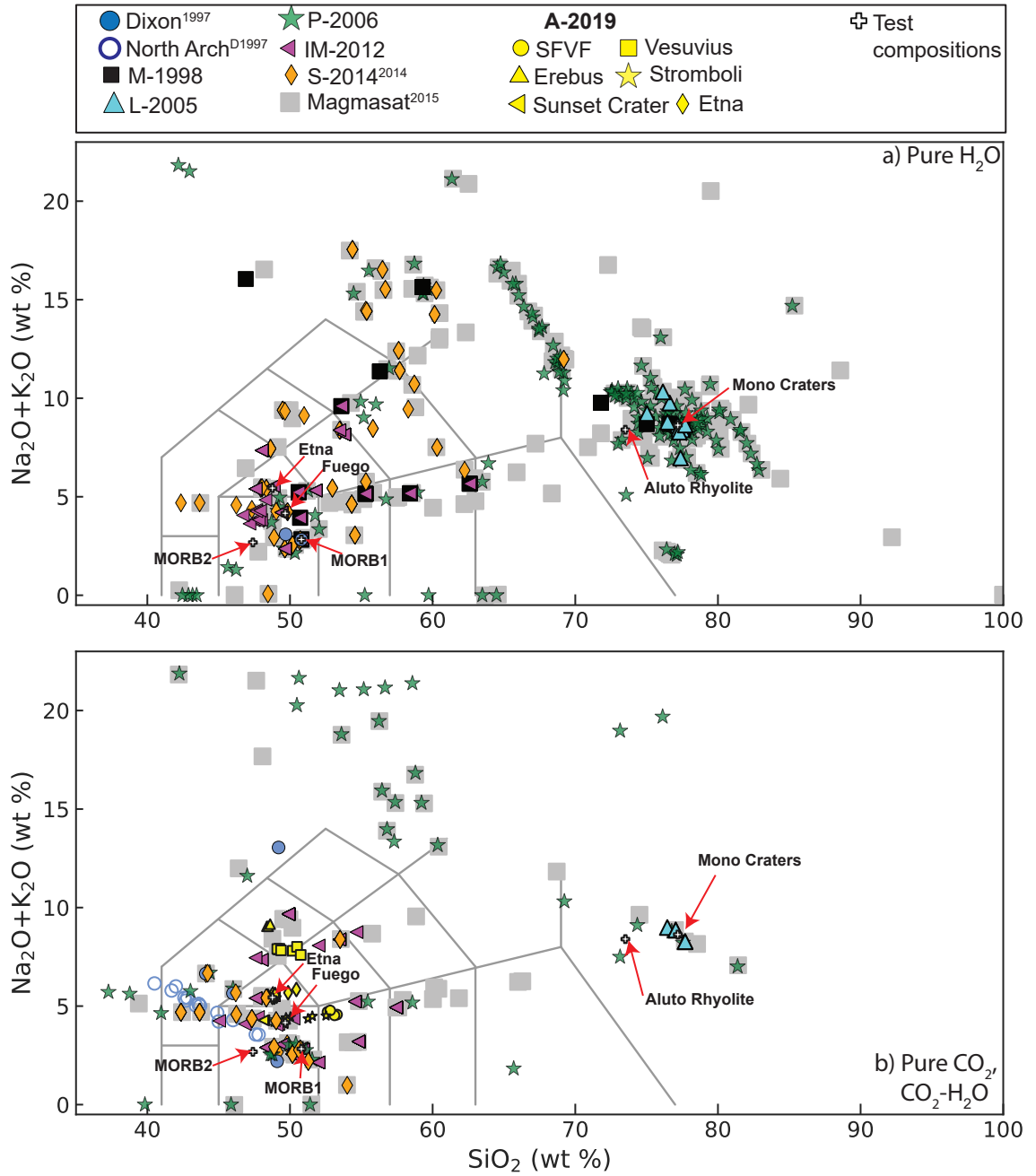


Figure 2. Total alkalis ($\text{Na}_2\text{O}+\text{K}_2\text{O}$) vs. SiO_2 (TAS) diagram showing the composition of melts in the calibration dataset of each model. We combine pure CO_2 and $\text{CO}_2\text{-H}_2\text{O}$ experiments into a single plot, because pure CO_2 experiments are often contaminated by variable amounts of H_2O due to exposure with the earth’s atmosphere, and the high mobility of H^+ through experimental apparatus (Mangan et al., 2021). As dissolved H_2O contents in glasses from pure CO_2 experiments are rarely reported, it is nontrivial to distinguish these from a mixed $\text{H}_2\text{O-CO}_2$ experiment. For P-2006 and MagmaSat, points were extracted from the TAS diagrams shown in these papers using Web Plot Digitizer (Rohatgi, 2017). For the other models, the calibration dataset is provided in the supplementary information of Iacovino et al. (2021). TAS plot drawn using python code from Stevenson (2015).

3.1 VolatileCalc-Basalt: a simplification of Dixon (1997)

The Dixon (1997) model calculates the solubility of H₂O and CO₂ in basaltic silicate melts, combining thermodynamic expressions as a function of pressure and temperature described in Dixon et al. (1995) with empirical parameters from Dixon (1997) accounting for the effect of melt composition in terms of melt SiO₂ content. The thermodynamic expressions are originally from Fine and Stolper (1986) for carbon, and Silver and Stolper (1989) for water. The Dixon (1997) model considers the solubility of the carbonate ion (CO₃²⁻) for CO₂, and both molecular water (H₂O_{mol}) and hydroxyl groups (OH⁻) for H₂O.

The solubility of molecular H₂O is calculated using an adapted version of equation 3 of Dixon et al. (1995). In the original equation, the X_{H₂O_{mol}}^m(P₀, T₀) term (representing the mole fraction of molecular H₂O in equilibrium with fluid with a fugacity of water specified by f_{H₂O}(P₀, T₀) at 1473.15 K and 1 bar) was fixed at 3.28 × 10⁻⁵. To account for the effect of melt composition on H₂O solubility, Dixon (1997) parametrize this term as a function of melt SiO₂ content:

$$X_{\text{H}_2\text{O}_{\text{mol}}}^{\text{m}}(\text{P}_0, \text{T}_0) = 3.04 \times 10^{-5} + 1.29 \times 10^{-6}[\text{SiO}_2]^{\text{wt}\%} \quad (1)$$

This relationship was derived from experimental observations of Cocheo and Holloway (1993), and predicts that there is a ~30% increase in the solubility of H₂O with increasing SiO₂ between nephelinite (~40 wt% SiO₂) and tholeiite (~49 wt% SiO₂) melt compositions. The concentration of OH⁻ is then calculated as a function of the mole fraction of molecular H₂O in the melt using the solution model of Silver and Stolper (1989) (see equation 4 of Dixon, 1997). Interesting, this is the only model discussed here which considers more than one species for dissolved H₂O in the melt.

For CO₂ solubility, Dixon (1997) adapted the model of Dixon et al. (1995) to account for the effect of melt composition, based on observations from experiments that CO₂ solubility increases from tholeiitic (49 wt% SiO₂) to basaltic (46 wt% SiO₂) to leucitic (44.1 wt% SiO₂) melts at 1200°C, 1 kbar. A linear regression with CO₂ solubility was achieved using a composition parameter (II) expressed in terms of the cation fractions, X_i(Dixon, 1997):

$$\text{II} = -6.50(X_{\text{Si}^{4+}} + X_{\text{Al}^{3+}}) + 20.17(X_{\text{Ca}^{2+}} + 0.8X_{\text{K}^+} + 0.7X_{\text{Na}^+} + 0.4X_{\text{Mg}^{2+}} + 0.4X_{\text{Fe}^{2+}}) \quad (2)$$

However, based on the strong correlation between II and SiO₂ in a suite of lavas from the North Arch Volcanic Field, Dixon (1997) simplify the X_{CO₃²⁻}^m(P₀, T₀) from equation 6 of Dixon et al. (1995) solely as a function of melt SiO₂ content:

$$X_{\text{CO}_3^{2-}}^{\text{m}}(\text{P}_0, \text{T}_0) = 8.70 \times 10^{-6} - 1.70 \times 10^{-7}[\text{SiO}_2]^{\text{wt}\%} \quad (3)$$

236 Where $X_{\text{CO}_3^{2-}}^m(P_0, T_0)$ is the mole fraction of carbonate in equilibrium with fluid with a fugacity of
 237 carbon dioxide specified by $f_{\text{CO}_2}(P_0, T_0)$ at 1473.15 K and 1 bar. Fugacities are calculated using the
 238 Redlich-Kwong equation of state (Holloway, 1977), with the correction of Flowers (1979).

239 This simplified expression was designed to aid the investigations of volatile solubility in the suite
 240 of lavas from the North Arch, where it effectively captures the observed $5\times$ decrease in CO_2 solubility
 241 between 40 and 49 wt% SiO_2 . However, this simplified parameterization became very widely used in
 242 a wide variety of tectonic settings following its implementation in the excel-based tool VolatileCalc
 243 (Newman and Lowenstern, 2002). Here, we refer to this model as VolatileCalc-Basalt, to differentiate
 244 it from the full Π parameterization of Dixon (1997).

245 The advantage of the Π - SiO_2 simplification is that users only have to input the concentration of
 246 one oxide component (melt SiO_2) in addition to melt temperature and melt volatile contents to cal-
 247 culate saturation pressures or degassing paths. The limited number of inputs required by this model
 248 meant that users can calculate saturation pressures for large numbers of melt inclusions relatively
 249 quickly compared to more recent models such as Iacono-Marziano et al. (2012) and MagmaSat (which
 250 require users to input 8–14 oxide concentrations).

251 However, extreme care must be taken when using this simplified model to calculate CO_2 solubil-
 252 ity. Firstly, the North Arch lavas span SiO_2 contents of only 40-49 wt%. Because of the rapid drop in
 253 Π with increasing SiO_2 , extrapolation beyond 51.2 wt% SiO_2 yields a negative value for $X_{\text{CO}_3^{2-}}^m(P_0,$
 254 $T_0)$, corresponding to a negative amount of dissolved CO_2 . To avoid this issue, VolatileCalc-Basalt
 255 returns an error, and will not perform the calculation if users enter a SiO_2 content >49 wt%. Most
 256 studies extrapolate beyond this by simply entering $\text{SiO}_2=49$ wt% into VolatileCalc-Basalt if their
 257 melts have higher silica contents (e.g. Sides et al., 2014a, 2014b; Tucker et al., 2019), and this ap-
 258 proach is implemented in VESICAL for consistency. Newman and Lowenstern (2002) suggest that this
 259 extrapolation will be “generally applicable for other basaltic rocks with <52 wt% SiO_2 ”. However,
 260 if a large proportion of a sample suite has SiO_2 contents with >49 wt% SiO_2 , the simplified Π - SiO_2
 261 parameterization treats all melts as if they have the same composition, neglecting variations in sol-
 262 ubility that may exist within that suite (see Wieser et al., 2020). Additionally, even if samples have
 263 SiO_2 contents between 40–49 wt%, this simplification can yield spurious results for melts which do not
 264 follow the same trend in Π - SiO_2 space to the North Arch lavas (see section 4.2.3). Thus, we suggest
 265 that any users wishing to apply VolatileCalc-Basalt to their system first check whether their melt com-
 266 positions lie close to the trend defined by the North Arch lavas using the Jupyter notebook provided in
 267 the supplementary information of Iacovino et al. (2021).

268 It is also worth nothing that, because VolatileCalc-Basalt parameterizes the effect of melt com-
 269 position in terms of the absolute concentration of SiO₂ (rather than other empirical models which
 270 use cation fractions), it is extremely sensitive to normalization. For example, consider the MORB2
 271 composition of Table 1 with a measured SiO₂ content of 47.4 wt%, and an anhydrous total of 97.375
 272 wt%. For 1000 ppm CO₂ and T=1200°C, using raw data (SiO₂=47.4 wt%) the calculated saturation
 273 pressure is 1206 bars. However, it is reasonably common in the literature that major elements (exclud-
 274 ing volatiles) are scaled to sum to 100%, while volatile concentrations are left unchanged. This would
 275 cause the melt SiO₂ content to increase to 48.68 wt% SiO₂, corresponding to a saturation pressure
 276 of 1765 bar respectively (1.7× higher!). We encourage users not to normalize their data, as we note
 277 that the II-SiO₂ plot of North Arch Glasses show in Dixon (1997) are best recreated using unnormal-
 278 ized data (see Supporting Fig. S4). However, as the analytical totals of the North Arch lavas only
 279 vary from 97.38–100 wt%, extreme care should be taken when applying this model to more hydrous
 280 magmas (where it has not been calibrated). Unnormalized data is used throughout this review for all
 281 VolatileCalc-Basalt outputs, which gives results comparable to those produced in the VolatileCalc-
 282 Basalt spreadsheet when users enter the SiO₂ contents given in Table 1.

283 **3.2 VolatileCalc-Rhyolite: Newman and Lowenstern, 2002**

284 In addition to the functionality for basalts described above, the VolatileCalc spreadsheet also
 285 allows users to calculate saturation pressures, degassing paths, isobars and isopleths for rhyolitic mag-
 286 mas (hereafter, VolatileCalc-Rhyolite). For CO₂, VolatileCalc-Rhyolite uses the simple thermodynamic
 287 model from Stolper et al. (1987) that was later applied to rhyolitic melts by Fogel and Rutherford
 288 (1990). The molar enthalpy change for CO₂ dissolution in the melt is from Fogel and Rutherford
 289 (1990), the single-O melt mass from Silver et al. (1990), and the CO₂ molar volume and solubility at
 290 standard state from Blank et al. (1993). The thermodynamic basis for the H₂O model is the same
 291 as that used in VolatileCalc Basalt. The fitted parameters for H₂O solubility in the standard state
 292 is from Silver (1988), and the single-O melt mass and molar enthalpy change for H₂O dissolution in
 293 the melt from Silver et al. (1990). The partial molar volume of H₂O was adjusted to 5 cm³/mol to
 294 provide a better fit to experimental data. There are two main differences of the rhyolite model relative
 295 to the basaltic model. Firstly, while both the rhyolite and basalt models use a temperature-dependent
 296 equation of state, the rhyolitic model also contains a term for the heat of solution of volatile solubility,
 297 causing VolatileCalc-Rhyolite to display strong temperature dependence. Secondly, unlike the basaltic
 298 calculations which require users to enter melt SiO₂ contents, calculations for rhyolites magmas do not
 299 incorporate a compositional factor. Thus, Newman and Lowenstern (2002) caution that this model
 300 may not be applicable for strongly peralkaline or peraluminous rhyolites.

3.3 M-1998 (Moore et al., 1998)

The Moore et al. (1998) model calculates the solubility of H₂O for a wide range of silicate melt compositions using an empirical expression valid between 700–1200°C and 0–3000 bars:

$$2 \ln(X_{\text{H}_2\text{O}}^{\text{melt}}) = \frac{a}{T} + \sum_i b_i X_i \frac{P}{T} + c \ln(f_{\text{H}_2\text{O}}^{\text{fluid}}) + d \quad (4)$$

Where $X_{\text{H}_2\text{O}}^{\text{melt}}$ is the mole fraction of H₂O dissolved in the melt, T is the temperature in Kelvin, P is the pressure in bars, and X_i is the anhydrous molar fraction of each oxide component. $f_{\text{H}_2\text{O}}^{\text{fluid}}$ is the fugacity of H₂O in the fluid, calculated using the modified version of the Redlich-Kwong equation of state provided in the appendix of Holloway and Blank (1994). Equation 4 is associated with the following fit parameters (\pm standard error):

| Coefficient | a | $b_{\text{Al}_2\text{O}_3}$ | b_{FeO_T} | $b_{\text{Na}_2\text{O}}$ | c | d |
|-------------------------|--------------------|-----------------------------|-------------------------|---------------------------|-----------------------|-----------------------|
| Value ($\pm 1\sigma$) | 2565 (± 362) | -1.997 (± 0.706) | -0.9275 (± 0.394) | 2.736 (± 0.871) | 1.171 (± 0.069) | -14.21 (± 0.54) |

As equation 4 includes a term for the fugacity of H₂O in the fluid, this model can be integrated with CO₂ models implemented in VESICAL (e.g., the II-SiO₂ simplification of Dixon, 1997, Liu et al., 2005, Iacono-Marziano et al., 2012, Shishkina et al., 2014, Allison et al., 2019) to investigate mixed H₂O-CO₂ fluids.

The model calibration dataset combines the authors pure H₂O experiments with literature data, spanning sub-alkaline basaltic to rhyolitic compositions, as well as some alkaline compositions (Fig. 2). As with other fully-empirical models implemented in VESICAL, or those including empirical expressions, extreme care must be taken when extrapolating this model outside of the calibration range. In particular, the authors warn against extrapolating this model to pressures exceeding 3 kbar, in part due to the complexities of the critical behavior of fluids at higher pressures.

3.4 L-2005 (Liu et al., 2005)

The Liu et al. (2005) model calculates the solubility of H₂O and CO₂ in metaluminous, high-silica rhyolitic melts using empirical expressions, valid between 700–1200°C, and 0–5000 bars. The following expression is used to calculate CO₂ solubility:

$$[\text{CO}_2]^{ppm} = \frac{P_{\text{CO}_2}(b_1 + b_4 P_W)}{T} + P_{\text{CO}_2}(b_2 P_W^{0.5} + b_3 P_W^{1.5}) \quad (5)$$

T is temperature in Kelvin, b_1 – b_4 are fit parameters, and the P_W and P_{CO_2} terms account for the partial pressures of each volatile species in the co-existing fluid, with:

$$P_{\text{CO}_2} = X_{\text{CO}_2}^f P \quad (6)$$

$$P_W = X_W^f P \quad (7)$$

Where P is pressure in MPa, $X_{\text{CO}_2}^f$ is the mole fraction of CO_2 in the fluid, and X_{W}^f is the mole fraction of H_2O in the fluid. These empirical terms mean that no equation of state is used (unlike M-1998 and VolatileCalc-Basalt). The fit parameters associated with equation 5 are shown below (\pm error):

| Coefficient | b_1 | b_2 | b_3 | b_4 |
|---------------|--------------------|-------------------------|---|-----------------------|
| Value (Error) | 5668 (± 127) | 0.4133 (± 0.0491) | 2.041×10^{-3} ($\pm 0.285 \times 10^{-3}$) | -55.99 (± 8.36) |

Similarly, they provide the following expression for H_2O :

$$[\text{H}_2\text{O}_t]_{\text{wt}\%} = \frac{a_1 P_w^{0.5} + a_2 P_w + a_3 P_w^{1.5}}{T} + a_4 P_w^{1.5} + P_{\text{CO}_2} (a_5 P_w^{0.5} + a_6 P_w) \quad (8)$$

Using the following fit parameters:

| Coefficient | a_1 | a_2 | a_3 | a_4 |
|---------------|--|-----------------------|--|-------------------------------|
| Value (Error) | 354.94 (± 4.55) | 9.623 (± 0.923) | -1.5223 (± 0.0722) | 0.0012439 (± 0.0000499) |
| | a_5 | | a_6 | |
| | -1.084×10^{-4} ($\pm 0.406 \times 10^{-4}$) | | -1.362×10^{-5} ($\pm 0.352 \times 10^{-5}$) | |

The model calibration dataset combines pure H_2O solubility experiments by the authors between ~ 1 and 250 bars with literature experiments investigating the solubility of pure H_2O , $\text{H}_2\text{O}-\text{H}_2$, CO_2 and $\text{CO}_2-\text{H}_2\text{O}$ fluids, spanning significantly higher pressures (up to 5000 bars). Unlike the M-1998 model, their empirical expressions do not incorporate a term for melt composition, so care is needed when applying this model to melts with different major element compositions to the calibration dataset (Fig. 2).

3.5 P-2006 (Papale et al., 2006)

Papale et al. (2006) present a fully non-ideal thermodynamic model for H_2O and CO_2 solubility, which is a recalibration of the earlier models of Papale (1999) and Papale (1997). This updated model capitalizes on the large amount of volatile solubility experiments performed since 1997, which nearly doubled the size of the calibration dataset, and allowed experimental data on CO_2 solubility collected prior to 1980 to be discarded (removing systematic errors associated with different analytical techniques, see Papale, 1999). Unlike the models discussed above which are calibrated on a specific subregion of compositional space and use empirical parametrizations to account for the effect of melt composition, the models of Papale et al. (2006) and Papale (1999) treat the composition of the silicate liquid using a thermodynamic approach based on Ghiorso et al. (1983). Papale et al. (2006) note that this thermodynamic approach means that for any specific region of composition space (e.g., comparing model results to a specific experiment), the fit may not be as good as an empirical model tuned to that composition. However, carefully calibrated thermodynamic models will be significantly more successful than empirical models when applied to melts which are not represented in the calibration dataset.

P-2006 considers a silicate liquid in mechanical, thermal and chemical equilibrium with a fluid phase containing H₂O and CO₂. The model uses the modified Redlich-Kwong equation of state of Kerrick and Jacobs (1981) to describe the fluid phase, and considers only the dissolution of CO₂ and H₂O in the melt (while natural silicate melts contain molecular CO₂ and CO₃²⁻ species, and molecular H₂O and OH⁻ species). The model calculates the Gibbs free energy of mixing, considering 10 major oxide components in addition to CO₂ and H₂O. Binary interaction coefficients, denoted by w_{ij} , account for the attractive-repulsive behaviour between an oxide and volatile component. For example, $w_{CO_2, MgO}$ describes the interaction of MgO with CO₂. Interaction coefficients for CO₂ are expressed as a function of pressure (relative to a reference pressure of 0.1 MPa) requiring two coefficients, while those for H₂O are invariant of pressure (requiring 1 coefficient):

$$w_{CO_2,i} = w_{CO_2,i}^0 + w_{CO_2,i}^1 \ln \frac{P}{P_0} \quad (9)$$

$$w_{H_2O,i} = w_{H_2O,i}^0 \quad (10)$$

P-2006 uses interaction terms for SiO₂, Al₂O₃, MgO, CaO, Na₂O, K₂O, FeO and Fe₂O₃. The presence of two Fe terms means that the model is sensitive to melt redox. Papale et al. (2006) show that the inclusion of w terms for MnO and TiO₂ lead to overfitting, so the effect of these oxides on model outputs is only through the dilution of the concentration of components allocated w terms. The values of the 24 w terms, as well as 5 terms accounting for molar volumes and fugacities, are calculated from a calibration dataset comprising ~ 1100 solubility experiments with pure CO₂, pure H₂O and mixed CO₂-H₂O fluids. While the calibration dataset contains well populated clusters for basaltic and rhyolitic compositions, intermediate compositions and basaltic melts with high alkali contents are poorly represented, particularly for CO₂ (Fig. 2).

Papale et al. (2006) demonstrate that despite the addition of hundreds of new experimental datapoints for H₂O, there are no significant changes in coefficients compared to those which were published with their 1999 model. The percent errors on these coefficients in the 2006 model are $< 10\%$ for all species (defined as $100 * \sigma / \text{coefficient}$). In contrast, the addition of new CO₂ data to the calibration dataset resulted in significant changes in model parameters, and the percentage errors on these coefficients in the 2006 model remained large ($\sim 800\%$ for FeO, $\sim 150\%$ for Na₂O, $\sim 190\%$ for MgO, Table 3). Based on these large error values, these coefficients would likely change again if this model was recalibrated to include all new CO₂ experiments published since 2006.

Finally, the pressure-dependence of the CO₂ melt interaction terms, combined with the fact that the w_0 and w_1 terms have different signs for all oxides except FeO, means that a given change in melt chemistry may cause an increase in CO₂ solubility at one pressure, but a decrease at another pressure (see Section 4.1). Ghiorso and Gualda (2015) note that the coefficient for the compressibil-

367 ity of CO₂ in the P-2006 model is negative, which is physically impossible (implying volume of the
 368 CO₂ fluid increases when pressure is increased), which they suggest may arise from the inclusion of
 369 pressure-dependent w-terms.

P-2006

| Element | CO ₂ | | | | H ₂ O | |
|--------------------------------|-----------------|--------------|----------------|---------|------------------|---------|
| | w ₀ | % error (1σ) | w ₁ | % error | w ₀ | % error |
| SiO ₂ | -59,962 | 18 | 6049 | 19 | -34,093 | 1.85 |
| Al ₂ O ₃ | -590,957 | 32 | 41,395 | 47 | -189,117 | 2.54 |
| Fe ₂ O ₃ | 4,469,623 | 9 | -529,301 | 9 | 135,935 | 9.32 |
| FeO | 21,666 | 806 | 1214 | 1500 | -195,751 | 3.13 |
| MgO | 52,866 | 189 | -13,446 | 78 | -86,418 | 7.06 |
| CaO | -328,792 | 23 | 12,789 | 63 | -209,997 | 1.67 |
| Na ₂ O | 140,034 | 146 | -35,213 | 60 | -322,253 | 1.42 |
| K ₂ O | 309,070 | 48 | -58,010 | 27 | -349,798 | 1.79 |

MagmaSat

| Element | CO ₂ -CO ₃ ²⁻ | | | | H ₂ O | |
|---|--|--------------|------------------------|---------|------------------|---------|
| | W (CO ₂) | % error (1σ) | W (CaCO ₃) | % error | W | % error |
| SiO ₂ | | | 63.281 | 2.52 | 27.557 | 0.065 |
| TiO ₂ | -19.266 | 24.3 | -79.203 | 0.46 | 88.199 | 2.87 |
| Al ₂ O ₃ | | | 46.716 | 2.52 | 11.768 | 21.8 |
| Fe ₂ O ₃ | -3.187 | 4.9 | 65.509 | 0.26 | 50.105 | 17.0 |
| Fe ₂ SiO ₄ | -32.465 | 44.5 | -72.997 | 0.40 | 30.936 | 18.8 |
| Mg ₂ SiO ₄ | -40.854 | 164.3 | -24.873 | 4.17 | 20.910 | 21.5 |
| CaSiO ₃ | 30.012 | 80.0 | 37.534 | 2.70 | 9.715 | 27.5 |
| Na ₂ SiO ₃ | | | -311.011 | 0.24 | -82.460 | 2.9 |
| KAlSiO ₄ | | | -27.865 | 8.21 | 1.057 | 112 |
| Ca ₃ (PO ₄) ₂ | -3.473 | 172.6 | 37.534 | 0.13 | 44.133 | 0.76 |

Figure 3. Interaction coefficients for P-2006 and MagmaSat. Percentage errors calculated as 100*1σ/coefficient. Error are colored green if they are <10%, light pink if 10-25%, and red if >25%.

3.6 IM-2012 (Iacono-Marziano et al. 2012)

The Iacono-Marziano et al. (2012) model expresses the solubility of H₂O and CO₂ in mafic melts by combining simplified thermodynamic expressions for melt-fluid thermodynamics with empirical formulations accounting for melt composition. For CO₂, they present the following expression:

$$\begin{aligned}
 \ln[\text{CO}_2]^{\text{ppm}} &= X_{\text{H}_2\text{O}}d_{\text{H}_2\text{O}} + X_{\text{Al}}d_{\text{Al}} + X_{\text{FeO}+\text{MgO}}d_{\text{FeO}+\text{MgO}} + X_{\text{Na}_2\text{O}+\text{K}_2\text{O}}d_{\text{Na}_2\text{O}+\text{K}_2\text{O}} \\
 &+ a_{\text{CO}_2}\ln[\text{P}_{\text{CO}_2}] + b_{\text{CO}_2}\left[\frac{NBO}{O}\right] + B_{\text{CO}_2} + C_{\text{CO}_2}\frac{P}{T} \quad (11)
 \end{aligned}$$

Where P is the pressure in bars, T is the temperature in Kelvin, $X_{\text{H}_2\text{O}}$ is the molar fraction of H_2O in the melt and P_{CO_2} is the partial pressure of CO_2 in bars. The partial pressure of CO_2 is calculated from the pressure multiplied by the mole fraction of CO_2 in the fluid. This means that this model does not rely on an equation of state (as with the L-2005 model). The other terms account for the effect of melt composition using molar fractions calculated on a hydrous basis; $X_{\text{FeO}+\text{MgO}}$ is the sum of molar fractions of FeO_t and MgO , $X_{\text{Na}_2\text{O}+\text{K}_2\text{O}}$ is the sum of the molar fractions of Na_2O and K_2O , and X_{AI} is the aluminic index (AI):

$$X_{\text{AI}} = \frac{X_{\text{Al}_2\text{O}_3}}{X_{\text{CaO}} + X_{\text{K}_2\text{O}} + X_{\text{Na}_2\text{O}}} \quad (12)$$

The NBO/O term represents the number of non-bridging oxygens divided by oxygen, expressing the availability of oxygen to form carbonate groups within the melt. NBO/O can be calculated from mol fraction of different oxides, X_i , in two ways (termed anhydrous or hydrous basis):

$$\frac{\text{NBO}}{\text{O}}^{\text{Anhyd}} = \frac{2(X_{\text{K}_2\text{O}} + X_{\text{Na}_2\text{O}} + X_{\text{CaO}} + X_{\text{MgO}} + X_{\text{FeO}} - X_{\text{Al}_2\text{O}_3})}{2X_{\text{SiO}_2} + 2X_{\text{TiO}_2} + 3X_{\text{Al}_2\text{O}_3} + X_{\text{MgO}} + X_{\text{FeO}} + X_{\text{CaO}} + X_{\text{Na}_2\text{O}} + X_{\text{K}_2\text{O}}} \quad (13)$$

$$\frac{\text{NBO}}{\text{O}}^{\text{Hyd}} = \frac{2(X_{\text{H}_2\text{O}} + X_{\text{K}_2\text{O}} + X_{\text{Na}_2\text{O}} + X_{\text{CaO}} + X_{\text{MgO}} + X_{\text{FeO}} - X_{\text{Al}_2\text{O}_3})}{2X_{\text{SiO}_2} + 2X_{\text{TiO}_2} + 3X_{\text{Al}_2\text{O}_3} + X_{\text{MgO}} + X_{\text{FeO}} + X_{\text{CaO}} + X_{\text{Na}_2\text{O}} + X_{\text{K}_2\text{O}} + X_{\text{H}_2\text{O}}} \quad (14)$$

In both cases, mole fractions are calculated on a hydrous basis (Iacono-Marziano, written comms). Iacono-Marziano give coefficients for equation 11 for both cases ($\pm 2\sigma$), leading to two forms of this model: IM-2012-A (anhydrous) and IM-2012-H (hydrous):

| Coefficient | $d_{\text{H}_2\text{O}}$ | d_{AI} | $d_{\text{FeO}+\text{MgO}}$ | $d_{\text{Na}_2\text{O}+\text{K}_2\text{O}}$ | a_{CO_2} | b_{CO_2} | c_{CO_2} | B_{CO_2} |
|--|--------------------------|------------------|-----------------------------|--|-------------------|-------------------|--------------------|-------------------|
| Hydrous (\pmerror) | -16.4 (\pm 1.2) | 4.4 (\pm 0.4) | -17.1 (\pm 0.9) | 22.8 (\pm 1.1) | 1 (\pm 0.03) | 17.3 (\pm 0.9) | 0.12 (\pm 0.02) | -6 (\pm 0.4) |
| Anhydrous (\pmerror) | 2.3 (\pm 0.5) | 3.8 (\pm 0.4) | -16.3 (\pm 0.9) | 20.1 (\pm 1.1) | 1 (\pm 0.03) | 15.8 (\pm 0.9) | 0.14 (\pm 0.02) | -5.3 (\pm 0.4) |

We note for completeness that in the original publication, equation 11 was incorrectly expressed in terms of $\ln[\text{CO}_3^{2-}]$ (Iacono-Marziano, written. comms).

For H_2O , the authors state that it is statistically unjustified to include d_i terms similar to those in the CO_2 expression, due to the relatively small effect of melt composition on H_2O solubility. The effect of melt composition is incorporated only through the NBO/O term:

$$\ln [\text{H}_2\text{O}]^{\text{wt}\%} = a_{\text{H}_2\text{O}} \ln [P_{\text{H}_2\text{O}}] + b_{\text{H}_2\text{O}} \left[\frac{\text{NBO}}{\text{O}} \right] + B_{\text{H}_2\text{O}} + C_{\text{H}_2\text{O}} \frac{P}{T} \quad (15)$$

Where $P_{\text{H}_2\text{O}}$ is the partial pressure of H_2O in bars. As for CO_2 , coefficients are provided for NBO/O calculated on a hydrous and anhydrous basis. The hydrous coefficients in the published paper differ from those used in the web app over the last decade (although a new web app using the published coefficients appeared briefly in 2021). VESICAL uses the web app hydrous coefficients by default, as recommended by Iacono-Marziano (Pers. Comms). The coefficients in the published paper were from an older version of the model, and predict extremely high H_2O solubility at ~ 10 kbar ($>100\text{wt}\%$).

| Coefficient | a_{H_2O} | b_{H_2O} | B_{H_2O} | C_{H_2O} |
|--|--------------------|--------------------|---------------------|---------------------|
| Hydrous (\pmerror) | 0.53 (\pm 0.02) | 2.35 (\pm 0.28) | -3.37 (\pm 0.13) | -0.02 (\pm 0.02) |
| Anhydrous (\pmerror) | 0.54 (\pm 0.02) | 1.24 (\pm 0.28) | -2.95 (\pm 0.17) | 0.02 (\pm 0.02) |
| Web App | 0.52096846 | 2.11575907 | -3.24443335 | 0.02238884 |

The authors state that the differences between calculations performed with NBO/O calculated on a hydrous and anhydrous basis are relatively small, but that a slightly better fit to experimental data is obtained using the hydrous model (particularly for H₂O-rich, and CO₂-poor melts). For completeness, we perform calculations using both versions (referred to as IM-20120-H and IM-2012-A). Interestingly, we show that the anhydrous version is most similar to other models for MORB-like compositions, while the hydrous versions seems to perform better for alkaline melts (see section 4.2.1).

The calibration dataset for CO₂ combines the authors experiments with those from a variety of literature studies for mixed H₂O-CO₂ fluids, spanning temperatures between 1100 and 1400°C, and pressures between 100 and 10,000 bars (but mostly <5000 bars). The calibration dataset for H₂O incorporates pure H₂O experiments from the literature (spanning 163–6067 bars, and 1000–1250°C), as well as the experiments on H₂O-CO₂ fluids used to calibrate the CO₂ expression. Melt compositions are predominantly mafic, spanning subalkaline-alkaline basalts to basaltic andesites (45–57 wt% SiO₂ for mixed H₂O-CO₂ experiments, and 46–63 wt% SiO₂ for pure H₂O).

The empirical nature of the fitting terms incorporating melt composition, pressure and temperature means that users should be cautious when extrapolating this model to conditions lying outside the P-T-X range of the calibration dataset. In particular, Iacono-Marziano et al. (2012) highlight five weaknesses of their model:

1. The effect of melt MgO and FeO contents on CO₂ solubility is poorly constrained, because of the small variation in the concentrations of these oxides in the calibration database.
2. While their compositional terms for the effect of melt composition on CO₂ solubility gives equal weight to Na₂O and K₂O, the calibration dataset only includes K₂O-rich melts with a range of pressures, so the effect of substituting Na and K is poorly constrained.
3. The effect of temperature on the solubility of mixed H₂O-CO₂ is poorly constrained because the majority of experiments in the calibration dataset were performed at 1200-1300°C.
4. The relative role of molecular H₂O vs. OH⁻ on melt structure, which in turn influences CO₂ solubility, needs to be evaluated further.
5. The model was calibrated assuming that all Fe was Fe²⁺, so calculated solubilities are not sensitive to melt redox (unlike the model of P-2006).

These limitations are explored in more detail in sections 5 and 6.

3.7 S-2014 (Shishkina et al., 2014)

The Shishkina et al. (2014) model calculates the solubility of H₂O and CO₂ using fully-empirical expressions. Their expression for CO₂ solubility was calibrated on a dataset of mixed H₂O-CO₂ experiments on predominantly mafic compositions between 1200–1300°C, and 500–5000 bars:

$$\ln[\text{CO}_2]^{\text{ppm}} = 1.150 \ln(P) + 6.71 \Pi^* - 1.345 \quad (16)$$

P is the pressure in MPa, and Π^* is a compositional parameter expressed in terms of the cation fractions of 7 species:

$$\Pi^* = \frac{X_{\text{Ca}^{2+}} + 0.8 X_{\text{K}^+} + 0.7 X_{\text{Na}^+} + 0.4 X_{\text{Mg}^{2+}} + 0.4 X_{\text{Fe}^{2+}}}{X_{\text{Si}^{4+}} + X_{\text{Al}^{3+}}} \quad (17)$$

We note for completeness that the expression provided in Shishkina et al. (2014) incorrectly states that CO₂ in equation 16 was in wt%, rather than ppm.

Their expression for H₂O solubility was calibrated on a dataset of pure H₂O experiments with mafic to intermediate compositions between 1200–1250°C, and 485–5009 bars. It incorporates a composition parameter expressed in terms of the anhydrous cation fractions of Na and K:

$$[\text{H}_2\text{O}]^{\text{wt}\%} = (3.36 \times 10^{-7} P^3 - 2.33 \times 10^{-4} P^2 - 0.0711 P - 1.1309)(X_{\text{Na}} + X_{\text{K}}) \quad (18)$$

$$- 1.2 \times 10^{-5} P^2 + 0.0196 P + 1.1297 \quad (19)$$

In general, the compositional range of the Shishkina et al. (2014) dataset includes a larger variety of mafic compositions than that of Iacono-Marziano et al. (2012), particularly with respect to alkali-rich, or highly depolymerized melts (Fig. 2). However, as for Iacono-Marziano, the empirical nature of the compositional term means that extreme care is needed when extrapolating this model beyond the compositional range of the calibration dataset (see section 6).

One caveat of the implementation of this model in VESICAL is the treatment of mixing between CO₂ and H₂O. Shishkina et al. (2014) note that their experimental data shows evidence for significant non-ideality, with isobars remaining almost horizontal between 0–4 wt% H₂O (see their Fig. 6). However, the isobars shown on their plots are fitted to experimental data, rather than derived from their equations for CO₂ and H₂O solubility. These fits cannot be applied to melts with different compositions, and the authors give no guidance as to how to combine their equations for pure CO₂ and pure H₂O to reproduce this non-ideal behaviour for any given melt composition. Thus, due to an absence of other information, VESICAL treats mixing between H₂O and CO₂ as ideal in this model. To emphasize this difference, this mixed model is called ShishkinaIdealMixing in VESICAL.

3.8 MagmaSat: Ghiorso and Gualda (2015)

Ghiorso and Gualda (2015) present a comprehensive thermodynamic model (MagmaSat) for mixed H₂O-CO₂ solubility, calibrated on the most chemically-diverse set of natural silicate melt

438 compositions of all the models discussed thus far (Fig. 2). Thus, it is the default model in VESIcal.
 439 MagmaSat uses the equation of state of Z. Duan and Zhang (2006) for the CO₂-H₂O fluid, and is the
 440 volatile solubility model implemented in rhyolite-MELTS v.1.2 (Gualda et al., 2012). Thus, it is cur-
 441 rently the only model which can be directly integrated with phase equilibrium calculations (e.g., to
 442 track microlite growth during degassing upon ascent, or post-entrapment modification to melt inclu-
 443 sions). Like P-2006, the model considers the Gibbs free energy of solution using interaction parameters
 444 (denoted with a capital W in this model), although, unlike in P-2006, these terms are independent
 445 of pressure (as well as temperature). The exact choice of components differs from that of P-2006, as
 446 MagmaSat adapts the formulation from Rhyolite-MELTS (e.g., Mg is considered as Mg₂SiO₄, Ghiorso
 447 & Sack, 1995). Unlike P-2006, MagmaSat considers the dissolution of CO₂ as both molecular CO₂
 448 and carbonate species (as CaCO₃), with a set of *W* coefficients for each. It is apparent from the per-
 449 centage errors on these coefficients that the effect of melt composition on carbonate solubility is much
 450 better constrained than the effect of melt composition on molecular CO₂ solubility (percentage errors
 451 < 10% vs. errors up to 170%, Table 3). MagmaSat assumes that water dissolves entirely as a hy-
 452 droxyl species, rather than considering both hydroxyl and molecular species like Dixon (1997). This
 453 helps to reduce the number of interaction parameters for volatile-melt species, and seems to be a jus-
 454 tified simplification based on available experimental data (see Ghiorso and Gualda, 2015 for a more
 455 detailed discussion).

456 The calibration dataset for H₂O spans 550–1420°C, and pressures of 0–20,000 bars, and for CO₂
 457 spans 1140–1400 °C and 0–30,000 bars. Importantly, unlike P-2006, Magmasat is not calibrated for
 458 synthetic liquids (e.g., compositions only containing a small number of oxide species like Albite), so
 459 should only be applied to natural silicate liquid compositions.

460 **3.9 A-2019: Allison et al. (2019)**

461 Allison et al. (2019) present thermodynamic models to calculate CO₂ solubility for six different
 462 basaltic compositions from Stromboli (alkali basalt), Etna (trachybasalt), Vesuvius (phonotephrite),
 463 Erebus (phonotephrite), Sunset Crater (alkali basalt), and the San Francisco Volcanic Field (basaltic
 464 andesite, Fig. 2). Specifically, they performed experiments at 1200°C, and ~4000–6000 bars to address
 465 the paucity of experiments examining CO₂ solubility in alkali systems at mid crustal pressures. In
 466 addition to these experiments, their models for Vesuvius, Etna and Stromboli incorporate experiments
 467 from the literature, extending the calibration range of these three models to upper crustal pressures
 468 (see Fig. 1). Unlike models which incorporating the effect of changing melt composition empirically
 469 (e.g., Newman & Lowenstern, 2002; Iacono-Marziano et al., 2012; Shishkina et al., 2014), Allison et
 470 al. (2019) determine the parameters $\Delta V_r^{0,m}$ (the molar volume change of the condensed components

471 of the reaction) and $K_0(P_0, T_0)$ (the equilibrium constant at the reference pressure and temperature)
 472 within their thermodynamic equation empirically for each of the six compositions they examine, and
 473 create 6 separate models (each of which shows no compositional dependence). The A-2019 models use
 474 the modified Redlich-Kwong equation of state provided in the appendix of Holloway and Blank (1994).

475 Interestingly, Allison et al. (2019) show that CO_2 solubility does not simply scale with total al-
 476 kali contents. Erebus melts have $\text{Na}_2\text{O}+\text{K}_2\text{O}=8.8$ wt%, but dissolve less CO_2 than Etna and Vesuvius
 477 melts ($\text{Na}_2\text{O}+\text{K}_2\text{O}=5.2$ and 7.8 wt% respectively). They suggest that CaO, MgO and Al_2O_3 may play
 478 a role in the lower solubility of Erebus compared to Etna, but the fact that 5 of the 7 major elements
 479 they examine show notable differences between these melt compositions make it difficult to conclu-
 480 sively determine the origin of solubility variations. Ideally, users would apply the A-2019 Etna model
 481 to lavas erupted at Etna, the Stromboli model to lavas erupted at Stromboli and so on. The absence of
 482 an empirical term for melt composition means that extreme care should be taken when applying these
 483 equations to alkaline lavas with different major element contents to those used in the experiments of
 484 Allison et al. (2019), even if the lavas originated from one of the 6 volcanoes they examine.

485 Allison et al. (2019) only present equations for CO_2 solubility, as their experiments weren't de-
 486 signed to have a wide range of H_2O contents at different pressures, and their high $X_{\text{CO}_2}^f$ values mean
 487 that errors in their fluid fraction measurements propagate into large errors for H_2O fugacity (relative
 488 to the insignificant errors for CO_2 fugacity). In their supplementary spreadsheet, they integrate their
 489 CO_2 solubility models with an Etna power law fit for water solubility (Equation 2 of Lesne, Scaillet,
 490 Pichavant, Iacono-Marziano, & Beny, 2011). In VESICAL, users can combine any of the A-2019 carbon
 491 models with H_2O models from M-1998, IM-2012 and S-2014, or write their own.

492 4 Model Comparisons

493 To aid comparisons between models, a number of silicate melt compositions (Table 1) are used
 494 to examine the relationship between volatile solubility and pressure, the treatment of mixing between
 495 H_2O and CO_2 (manifested in the shapes of isobars), as well as sensitivity to parameters such as tem-
 496 perature and oxygen fugacity. For basalts, we example four compositions; two mid-ocean ridge basalts
 497 (termed MORB1 and MORB2), one alkali basalt and one arc basalt (grey crosses on Fig. 2). MORB1
 498 from Dixon et al. (1995) has 50.8 wt% SiO_2 , MORB2 from table 3 of Ghiorso and Gualda (2015)
 499 has 47.4 wt% SiO_2 (originally from Allan et al., 1989), and the Etna alkali basalt from Allison et al.
 500 (2019) has 48.8 wt% SiO_2 . Comparisons between these three compositions were performed at 1200°C .
 501 To investigate model sensitivities with relevance to mafic melt inclusion studies in volcanic arcs, we use
 502 the composition of a Fuego melt inclusion from Lloyd et al. (2013) with 49.7 wt% SiO_2 at 1000°C .

503 For rhyolitic magmas, we perform calculations at 800°C for a rhyolite from Mono Craters (East-
 504 ern California) and Aluto (African Rift). The Mono Craters composition is a high-Si, metaluminous
 505 rhyolite with 77.19 wt% SiO₂ from Liu et al. (2005). The Aluto composition is a peralkaline rhyolitic
 506 melt inclusion with 73.5 wt% SiO₂ from Iddon and Edmonds (2020). The Aluto rhyolite has much
 507 lower Al₂O₃ and higher FeO contents than the Mono Craters Rhyolite (Table 1).

Table 1. Representative compositions used for comparisons. MORB1 is a Mid-Oceanic Ridge Basalt tholeiite from Dixon et al. (1995). MORB2 is the MORB composition given in Table 3 of Ghiorso and Gualda (2015), originally from Allan et al. (1989). Etna is sample ET-8 from the supplementary information of Allison et al. (2019). Fuego is the composition of a melt inclusion from Lloyd et al. (2013). Mono Craters is from Table 1 of Liu et al. (2005). Aluto Rhyolite is the composition of a quartz-hosted melt inclusion from the East African Rift (MI70 from sample MER055A; Iddon & Edmonds, 2020).

| Name | MORB1 | MORB2 | Etna | Fuego | Mono Craters | Aluto Pumice |
|--------------------------------|-------|-------|-------|-------|--------------|--------------|
| SiO ₂ | 50.8 | 47.4 | 48.77 | 49.67 | 77.19 | 73.51 |
| TiO ₂ | 1.84 | 1.01 | 1.79 | 1.17 | 0.06 | 0.23 |
| Al ₂ O ₃ | 13.7 | 17.64 | 16.98 | 16.50 | 12.8 | 9.18 |
| Fe ₂ O ₃ | 2.1 | 0.89 | 2.51 | 1.65 | 0.26 | 1.41 |
| FeO | 10.5 | 7.18 | 6.44 | 8.43 | 0.71 | 3.81 |
| MnO | 0 | 0 | 0.18 | 0.19 | 0 | 0.25 |
| MgO | 6.67 | 7.63 | 6.33 | 4.38 | 0.03 | 0 |
| CaO | 11.5 | 12.44 | 11.26 | 7.90 | 0.53 | 0.2 |
| Na ₂ O | 2.68 | 2.65 | 3.65 | 3.37 | 3.98 | 4.18 |
| K ₂ O | 0.15 | 0.03 | 1.79 | 0.79 | 4.65 | 4.22 |
| P ₂ O ₅ | 0.19 | 0.08 | 0.53 | 0.22 | 0 | 0 |

508 4.1 Redox sensitivity

509 Before proceeding with these comparisons, it is worth noting that the vast majority of studies
 510 report whole-rock, melt inclusion and matrix glass compositions in terms of FeO_t, because the propor-
 511 tions of FeO vs. Fe₂O₃ are difficult to determine precisely using common analytical techniques such as
 512 electron probe microanalysis (EPMA) and x-ray fluorescence (XRF). VolatileCalc-Rhyolite and L-2005
 513 have no compositional terms, and VolatileCalc-Basalt is only parametrized in terms of the melt SiO₂
 514 content, so these 3 models are not sensitive to the choice of FeO vs. Fe₂O₃ for the representative com-
 515 positions in Table 1. Similarly, IM-2012 and M-1998 are parameterized using an FeO_t term, so also
 516 show no sensitivity to melt redox. S-2014 is technically slightly redox-sensitive for CO₂, because their
 517 Π* is expressed in terms of Fe²⁺ species (equation 17). However, given that the model was calibrated
 518 assuming Fe²⁺=Fe_T, any sensitivity to redox is likely spurious, so VESiCal calculates Π with Fe_T for
 519 consistency with their calibration. We show calculations performed for different Fe³⁺ ratios for com-
 520 pleteness in Fig. 4, but the rest of the figures in the manuscript using the S-2014 model are calculated

521 using Fe_T . H_2O solubility in S-2014 is not redox sensitive, because the effect of melt composition is
 522 only parametrized in terms of cation fractions of Na and K (equation 19). Both P-2006 and MagmaSat
 523 have interaction parameters for Fe^{2+} and Fe^{3+} -bearing species, so are redox sensitive for both CO_2
 524 and H_2O solubility.

525 To examine the sensitivity of our calculations of volatile solubility to melt redox by performing
 526 calculations for 0, 10 and 20% Fe^{3+} for MORB2, and 0, 30 and 60% Fe^{3+} for Etna (the higher re-
 527 dox accounting for the highly oxidising conditions of experiments on Etna melts, e.g., Lesne, Scaillet,
 528 Pichavant, & Beny, 2011).

529 Briefly, pure H_2O solubility in MagmaSat is relatively insensitive to redox, predicting only 2-
 530 3% more dissolved H_2O for 0% Fe^{3+} vs. 60% Fe^{3+} for the Etna melt composition (well within model
 531 error; Fig. 4a). Pure CO_2 solubility in MagmaSat is more redox sensitive than H_2O , predicting ~20-
 532 30% more H_2O for 0% Fe^{3+} vs. 60% Fe^{3+} (Fig. 4b). Pure H_2O solubility in P-2006 shows the same
 533 directionality as MagmaSat, but is more sensitive to redox ($1.8\times$ more H_2O dissolves at 0.1 kbar for
 534 0% Fe^{3+} vs. 60% Fe^{3+} , dropping to $1.2\times$ at > 2 kbar). Pure CO_2 solubility in P-2006 is extremely
 535 redox-sensitive, with melts with 0% Fe^{3+} vs. 60% Fe^{3+} dissolving $25\times$ more CO_2 at 0.5 kbar, but
 536 $0.5\times$ less at 5 kbar. S-2014 is slightly less redox sensitive than MagmaSat for CO_2 . Varying Fe^{3+} pro-
 537 portions between 0-20% for MORB2 produces similar patterns, with changes lying within model error
 538 for MagmaSat and S-2014, but showing significant differences for P-2006 (Fig. 4c-d). Isobars for this
 539 composition are also shown (Fig. 4e-f). For the smaller changes in Fe^{3+} proportions considered for
 540 MORB2, changes in dissolved H_2O and CO_2 contents for MagmaSat and S-2014 are well within model
 541 uncertainty (generally stated as 10-20%). In contrast, P-2006 shows changes in dissolved CO_2 which
 542 are significantly larger than quoted errors on solubility models.

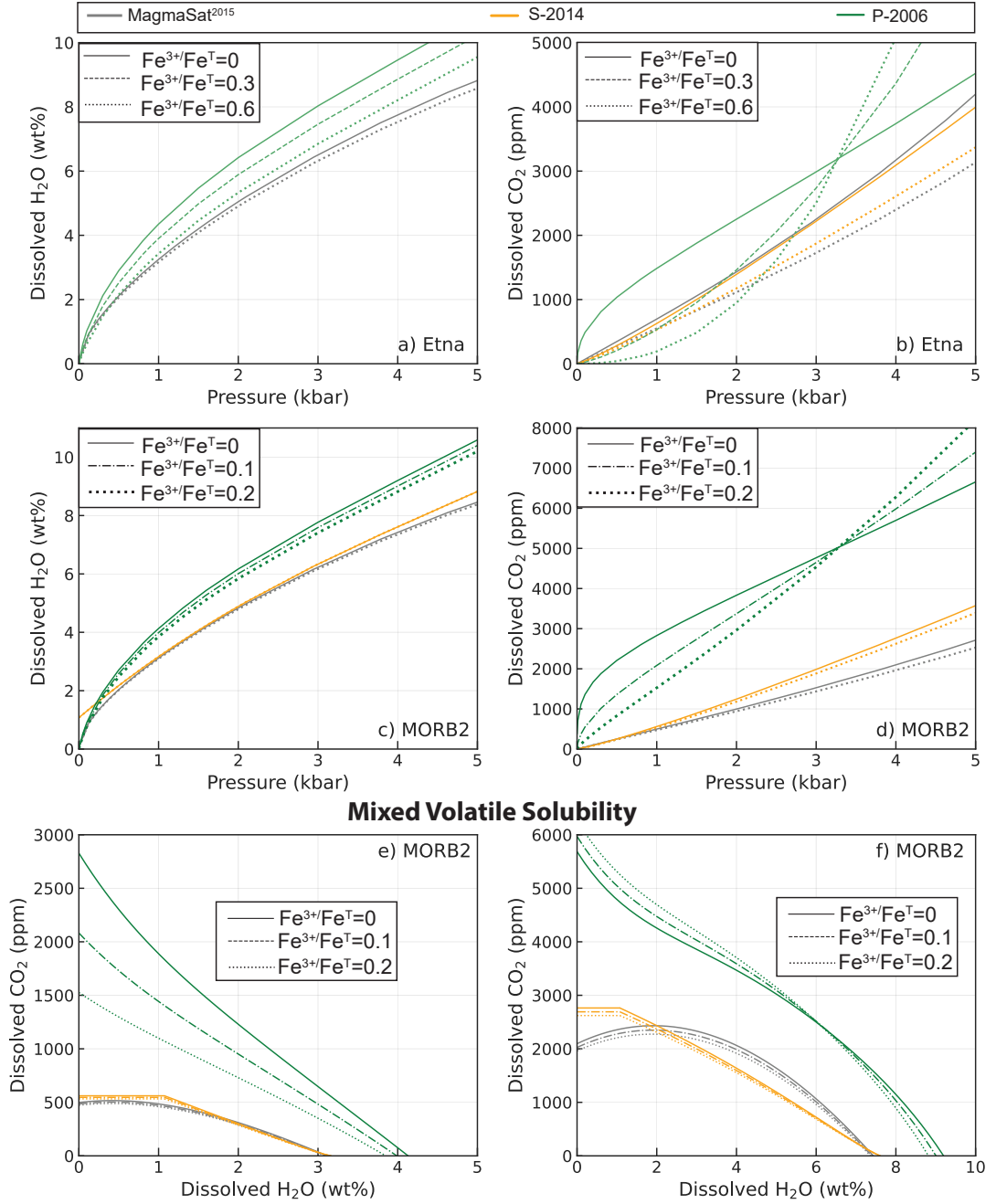


Figure 4. Relationship between volatile solubility and the proportion of Fe^{3+} for: a-b) the Etna composition at 1200°C ; c-d) the MORB2 composition at 1200°C , with isobars shown in e) for 1 kbar, and f) 4 kbar.

543

The different sensitivities of MagmaSat and P-2006 are apparent from examining the interaction coefficients in Table 3. In MagmaSat, the $W_{\text{Fe}_2\text{O}_3, \text{H}_2\text{O}}$ coefficient is only $1.6\times$ bigger than $W_{\text{Fe}_2\text{SiO}_4, \text{H}_2\text{O}}$ (~ 50 vs. 31), and these two coefficients overlap within $\pm 1.5\sigma$ of the uncertainty of these coefficients. This accounts for the relatively weak effect of redox on calculated H_2O solubility.

546

547 For the CaCaO_3 component representing the carbonate ion, the coefficients have similar magnitudes,
 548 but opposite signs ($W_{\text{Fe}_2\text{O}_3, \text{CaCO}_3} \sim 66$, $W_{\text{Fe}_2\text{SiO}_4, \text{CaCO}_3} \sim -73$), and this difference is much larger
 549 than the error on the coefficients (accounting for the stronger effect of melt redox on CO_2 solubility
 550 compared with H_2O). The Fe_2O_3 and Fe_2SiO_4 coefficients for the CO_2 component (which becomes
 551 more dominant in more evolved compositions) are also significantly different outside the quoted error
 552 but have the same sign ($W_{\text{Fe}_2\text{O}_3, \text{CO}_2} \sim -32$, $W_{\text{Fe}_2\text{SiO}_4, \text{CO}_2} \sim -3$).

553 In P-2006, the $w_{\text{H}_2\text{O}-\text{FeO}}^0$ coefficient is of similar magnitude, but opposite sign to $w_{\text{H}_2\text{O}-\text{Fe}_2\text{O}_3}^0$
 554 (1.4×10^5 vs. -2×10^5), and clearly distinct outside the error on each coefficient. This accounts for the
 555 slightly stronger sensitivity of H_2O in P-2006 to redox compared with MagmaSat. In stark contrast
 556 to all the comparisons thus far, the $w_{\text{CO}_2-\text{Fe}_2\text{O}_3}^0$ coefficient is $>200\times$ larger than $w_{\text{CO}_2-\text{FeO}}^0$. In fact,
 557 $w_{\text{CO}_2-\text{Fe}_2\text{O}_3}^0$ is $\sim 8\times$ higher than the next largest coefficient, suggesting that for a given mole fraction
 558 in the melt, it has the largest effect on carbonate ion solubility. The $w_{\text{CO}_2-\text{Fe}_2\text{O}_3}^1$ coefficient in P-2006
 559 model, which become more dominant at higher pressures, has the opposite sign to that for w_0 . This
 560 accounts for the fact that at low pressures (<3 kbar), increasing proportions of Fe^{3+} cause a decrease
 561 in CO_2 solubility, while at higher pressures, increasing proportions of Fe^{3+} cause CO_2 solubility to
 562 increase.

563 It is difficult to trust the extreme sensitivity of CO_2 in P-2006 to redox given the large uncer-
 564 tainty associated with the proportions of Fe^{3+} in volatile solubility experiments. For example, S-2014
 565 note that only 7 of the 48 experiments in their calibration dataset contain non-zero values of Fe_2O_3 .
 566 Similarly, in the P-2006 dataset, only 6 studies used in the calibration directly determined the propor-
 567 tion of Fe^{3+} , and only a further 9 reported the experimental oxygen fugacity. Thus, for the vast ma-
 568 jority of their experimental calibration dataset, Papale et al. (2006) calculate the proportion of Fe^{3+}
 569 assuming the oxygen fugacity is controlled by the $\text{H}_2\text{O}-\text{H}_2$ equilibrium at the stated experimental con-
 570 ditions. However, this method requires accurate measurements of fluid composition, is affected by Fe
 571 and H^+ -loss during experiments, and it is unclear how applicable this method is for mixed $\text{H}_2\text{O}-\text{CO}_2$
 572 experiments (Botcharnikov et al., 2006). The P-2006 calibration dataset contains some very surprising
 573 values: in the calibration dataset for pure CO_2 experiments, the experiments of Fogel and Ruther-
 574 ford (1990) have been allocated $\text{Fe}^{3+}/\text{Fe}_T$ ratios of $\sim 0.9-1$, despite the authors debating whether their
 575 experiments were actually reducing enough to stabilize a CO species. Similarly, the mixed $\text{CO}_2-\text{H}_2\text{O}$
 576 experiments of Paonita et al. (2000) have been allocated $\text{Fe}^{3+}/\text{Fe}_T$ ratios of ~ 0.9 , despite the starting
 577 materials having $\text{Fe}^{3+}/\text{Fe}_T$ ratios of 0.01 and 0.45 for rhyolites and basalts respectively. Although it
 578 might seem that a few such studies will not influence the overall result, it is worth noting that the
 579 model is relatively over constrained for CO_2 . While there are 10 coefficients for H_2O calibrated using

865 datapoints of pure-H₂O solubility, there are 20 coefficients for CO₂, and only 173 datapoints for
 581 pure-CO₂ solubility and 84 for mixed fluids. In particular, the main problem is that these highly
 582 oxidising Fe³⁺/Fe_T ratios are present for experiments with low CO₂ contents and pressures, making
 583 it difficult to deconvolve the differential effects of these parameters in a model with a large number of
 584 coefficients being calibrated on a relatively small calibration dataset.

585 Finally, we wish to draw attention to the very large error on the CO₂-FeO coefficients ($w_0 \sim$
 586 800% and $w_1 \sim 1500\%$), but the relatively small error on the CO₂-Fe₂O₃ coefficients in the P-2006
 587 model ($w_0 \sim 9\%$ and $w_1 \sim 9\%$; Fig. 3). It is likely that the error on the FeO coefficient accurately
 588 represents the large uncertainty on the effect of melt redox on CO₂ solubility, while the 9% error on
 589 the CO₂-Fe₂O₃ coefficients is unrealistically optimistic, given the very large uncertainties associated
 590 with estimating Fe³⁺/Fe_T proportions from experiments which did not report any information on
 591 redox conditions.

592 In sections 4.2 to 5, we show calculations using the Fe³⁺/Fe_T proportions in Table 1, as these
 593 best-estimates for each center are representative of what a user would select when calculating melt
 594 inclusion saturation pressures, dissolved volatile contents etc. For MORB1, MORB2, and Fuego, these
 595 proportions are from the original publications. For Etna, Fe₂O₃ was calculated from FeO_t assuming
 596 Fe³⁺/Fe_T=0.26 after Gaborieau et al. (2020). For Mono Craters and the Aluto pumice, Fe³⁺/Fe_T was
 597 set at 0.25 based on available data on other rhyolites (e.g., Ghiorso and Gualda, 2015), and modelling
 598 studies of the fractional crystallization path at Aluto (Gleeson et al., 2017).

599 4.2 Mafic Compositions

600 4.2.1 Pure H₂O

601 The 7 models applicable to H₂O in basaltic systems predict a sharp rise in pure H₂O solubility with
 602 increasing pressure (Fig. 5). For all three melt compositions, S-2014, IM-2012-A, VolatileCalc-Basalt,
 603 and M-1998 predict H₂O concentrations within $\pm 10\%$ of MagmaSat (grey envelope) between $\sim 1-5$
 604 kbar. For MORB1 and MORB2, IM-2012-H begins to deviate to higher H₂O contents than MagmaSat
 605 at >1 kbar. For Etna, IM-2012-H follows a similar trajectory between 0-3 kbar to the solubility model
 606 of Lesne, Scaillet, Pichavant, Iacono-Marziano, and Beny (2011) developed specifically for Etna melts
 607 (yellow line, Fig. 5d). In contrast, P-2006 plots to substantially higher H₂O solubilities compared to
 608 all other models at >0.5 kbar (although P-2006 and IM-2012-H intercept at higher pressures).

609 The fact that IM-2012-H predicts higher H₂O solubility relative to the cluster of other models ly-
 610 ing within the error window of MagmaSat is an interesting observation. Iacono-Marziano et al. (2012)
 611 favour their hydrous model, particularly for CO₂-poor, H₂O-rich melts, based on regressions between
 612 predicted and measured H₂O contents, and by comparing the two models to experiments conducted

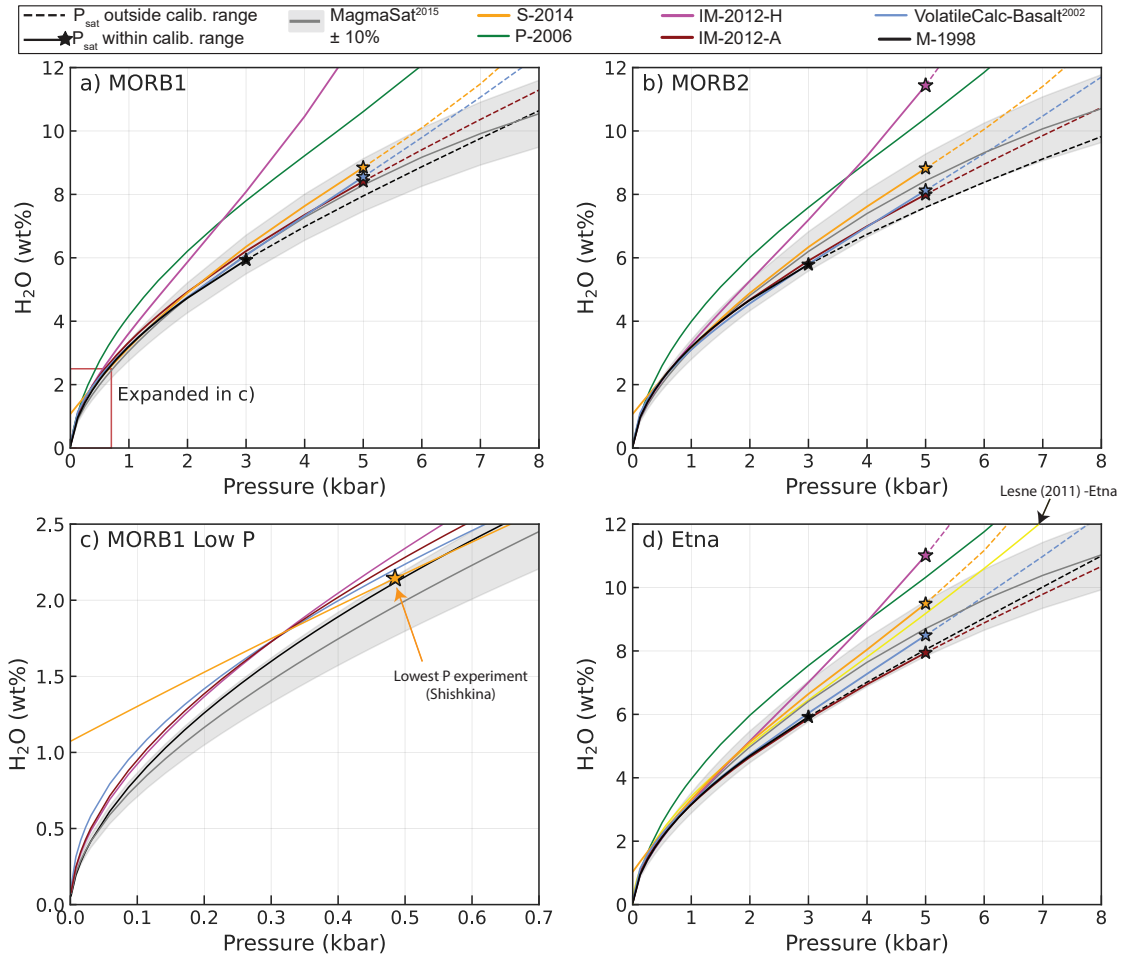


Figure 5. Relationship between pure H₂O solubility and pressure for MORB1, MORB2 and Etna melts at 1200°C. The grey field shows a $\pm 10\%$ error window around MagmaSat. Model lines are dashed when extrapolated above the recommended pressure range. The low pressure region of a) is expanded in c), emphasizing the non-zero solubility of H₂O at P=0 bar in the S-2014 model.

613 between 1 and 4 kbar on Etna melts (their Figure 7a). However, their Figure 8c, which compares dis-
 614 solved volatile contents calculated by the model for the entire calibration dataset, shows that predicted
 615 H₂O contents using the hydrous version are overestimates for experimental products with >6–7 wt%
 616 H₂O (although these predictions still lie within the $\sim 17\%$ error associated with their H₂O model).
 617 Our comparisons suggest that the anhydrous model appears more suitable than the hydrous model at
 618 higher pressures (and for tholeiitic compositions like MORB1 and MORB2 at all pressures).

Another notable oddity is the nearly linear trajectory of H₂O vs. P in S-2014 at <0.5 kbar, causing this model to predict a non-zero solubility of H₂O at 0 bar (Fig. 5c). This contrasts with the

power-law shapes followed by the other models which intercept very close to the origin. This anomalous behaviour is because the S-2014 equation for H₂O solubility (equation 19) simplifies at P=0 to:

$$[\text{H}_2\text{O}]^{\text{wt}\%} = -1.1309(X_{\text{Na}} + X_{\text{K}}) + 1.1297 \quad (20)$$

In the S-2014 calibration dataset, $X_{\text{Na}} + X_{\text{K}}$ varies from 0.05 to 0.25, which corresponds to solubilities of 0.85–1.07 wt% H₂O at 0 bar. This demonstrates the issue with extrapolating empirical expressions beyond the calibration range (the lowest pressure experiment in the calibration dataset of S-2014 was conducted at 485 bar). When combined with the assumption of ideal mixing used in VESical, this non-zero solubility of H₂O at 0 bar results in S-2014 predicting unusual degassing paths and isobar shapes relative to other models. For example, if a melt has <1 wt% H₂O, S-2014 predicts that the co-existing fluid contains no H₂O, despite abundant evidence that volcanic plumes in low H₂O systems such as Hawai'i are dominated by H₂O at low pressures (Gerlach, 1986). It also causes isobars to be entirely flat at low H₂O contents (see section 4.2.2, Fig. 6).

Overall, these comparisons show that, excluding P-2006, IM-2012-H and S-2014 (based on the anomalous behavior at low H₂O contents), 4 of the most popular solubility models predict dissolved H₂O concentrations within error of one another at pressures lower than the upper calibration limit. This likely reflects the relatively small effect of melt composition of H₂O solubility, meaning that more recent models calibrated on a wider compositional range display similar behavior to older models (G. Moore & Carmichael, 1998; Papale et al., 2006). The larger deviation between models at higher pressures reflect the fact that very few pure-H₂O solubility experiments have been performed at > 5 kbar (Table 1). One reason for this shortage of higher pressure experimental data results from the fact that it is very difficult to quench silicate melts with >9 wt% to a glass phase which can be analysed by FTIR or SIMS (Gavrilenko et al., 2019; Mitchell et al., 2017).

4.2.2 *Mixed H₂O-CO₂*

The majority of experiments used to derive expressions for pure-CO₂ solubility contained dissolved H₂O and CO₂ (e.g., Iacono-Marziano et al., 2012; Shishkina et al., 2014; Allison et al., 2019), requiring authors to extrapolate to determine the behavior of pure fluids. Thus, it makes sense to consider the treatment of mixing between CO₂ and H₂O species in each model before considering predictions of pure CO₂ solubility which are affected by assumptions of mixing. The treatment of H₂O-CO₂ mixing is best demonstrated using isobar diagrams, which show the solubility of H₂O and CO₂ in a given silicate melt composition at a given pressure for proportions of $X_{\text{H}_2\text{O}}^f$ in the co-existing fluid ranging from 0 (interception with the y axis) to 1 (interception with the x axis). The treatment of mixed fluids differs quite considerably in each model.

648 VolatileCalc-Basalt models mixed fluids under the assumption of Henrian (ideal) mixing in the
 649 fluid and melt phase. Thus, the addition of H₂O always causes the solubility of CO₂ to decrease (and
 650 vice versa), and isobars possess a negative gradient, with a slightly sloping plateau at low H₂O con-
 651 tents merging into a concave-down shape (Fig. 6).

652 S-2014 does not provide an equation for the treatment of non-ideal mixing, despite their experi-
 653 ments showing that increasing H₂O contents at high pressure cause almost no change in CO₂ solubil-
 654 ity. Using the assumption of ideal mixing in VESIcal, S-2014 isobars exhibit a flat plateau at low H₂O
 655 contents, merging into a negative slope at higher H₂O contents. This flat plateau results from the fact
 656 that there are no partial pressures at which S-2014 yields H₂O < 1 wt%, so the y co-ordinate for lower
 657 H₂O contents is equal to the solubility of pure CO₂.

658 The P-2006 is fully non-ideal, which causes isobars to have complex shapes, exhibiting both posi-
 659 tive and negative gradients. In detail, the shape of isobars calculated using P-2006 differ as a function
 660 of both melt composition and temperature (see Fig. 12 of Papale, 1999). For the basaltic compositions
 661 considered here, isobars display an kick-up to higher CO₂ contents at very low H₂O contents (Fig. 6a,
 662 c), because the model predicts a decrease in CO₂ solubility following the addition of small quantities of
 663 H₂O.

664 IM-2012-A and IM-2012-H incorporate empirical representations of non-ideality through the
 665 inclusion of a term for the molar fraction of H₂O in the melt in their expression for CO₂ solubility
 666 (equation 11). This means that their model predicts that maximum CO₂ solubility occurs at non-zero
 667 H₂O concentrations, causing isobars to display prominent domed shapes (Fig. 6). Isobars calculated
 668 using the anhydrous version of Iacono-Marziano show a more extreme peak than the hydrous version.
 669 This reflects differences in the coefficient d_{H_2O} attached to the term for the molar fraction of H₂O in
 670 the melt. In the anhydrous version, d_{H_2O} is positive (2.3 ± 0.5), so the addition of small amounts of
 671 H₂O to the melt causes X_{H_2O} , and therefore CO₂ solubility to increase. In the hydrous expression,
 672 this coefficient is negative (-16.4 ± 1.2). Alone, this would cause the solubility of CO₂ to decrease with
 673 the addition of small amounts of water to the melt. However, NBO/O calculated on a hydrous basis
 674 increases with the addition of H₂O (because X_{H_2O} appears twice in the numerator, but only once in
 675 the denominator of the NBO/O term; equation 11), and the NBO/O term is attached to a positive
 676 coefficient (17.3 ± 0.9). This increase in NBO/O overwhelms the product of the negative coefficient
 677 multiplied by X_{H_2O} .

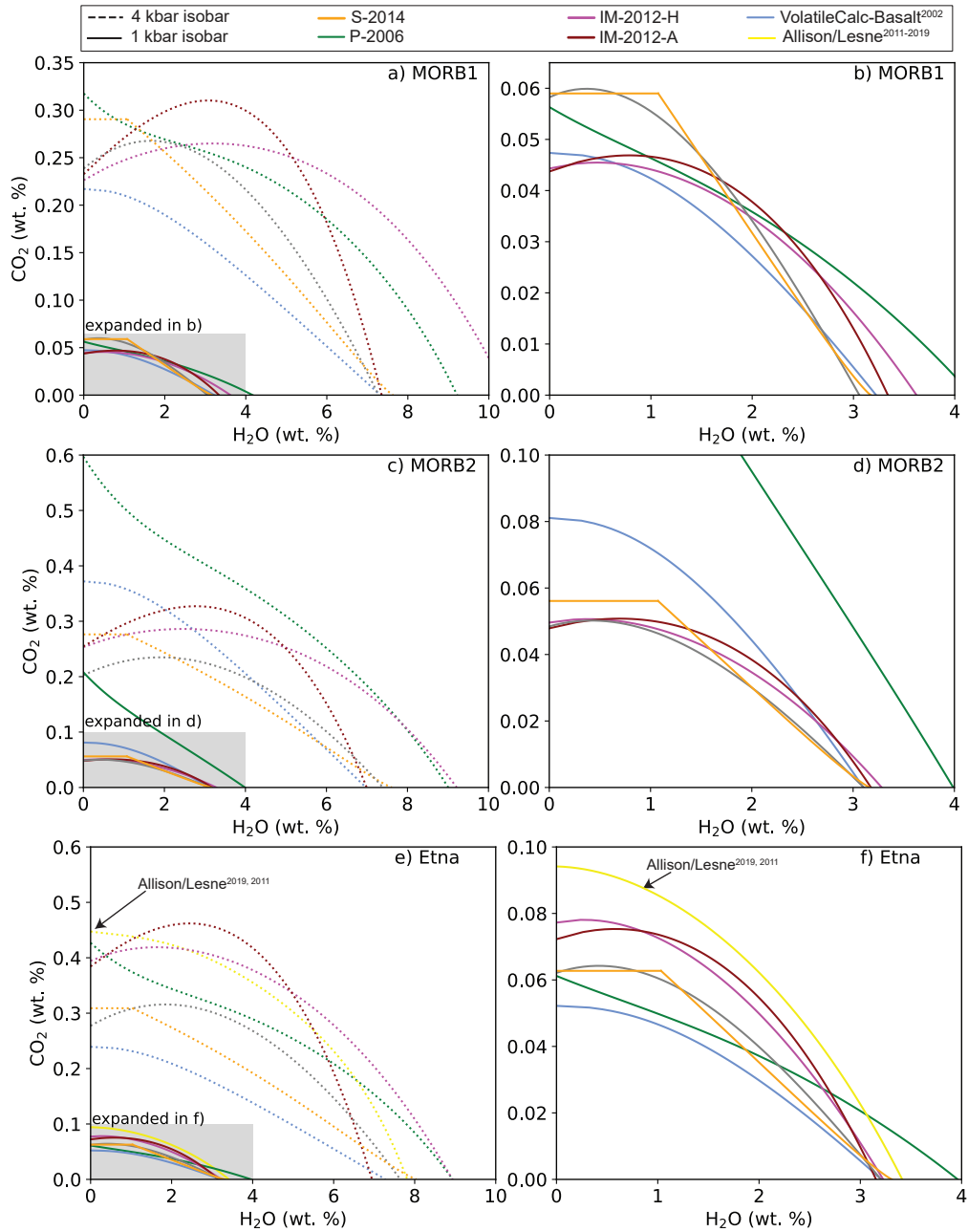


Figure 6. 1 and 4 kbar isobars for MORB1 (a-b) and MORB2 (c-d) and Etna (e-f) at 1200°C. The 1 kbar isobar is expanded in b), d) and e). The distinctive shapes of isobars from different models reflects different treatment of H₂O-CO₂ mixing. This is most apparent at higher pressures. The prominent plateau at <1 wt% H₂O for S-2014 at all pressures results from the non-zero solubility of H₂O at low pressures.

678

Like P-2006, MagmaSat is fully non-ideal. However, unlike P-2006, the treatment of non-ideality in MagmaSat predicts that the addition of small amounts of H₂O always causes the solubility of CO₂

679

680 to increase (causing isobars to peak at non-zero H₂O concentrations; Fig. 6, c). This peak becomes
 681 more pronounced at higher pressures, but is generally smaller than that predicted by IM-2012.

682 These different assumptions result in large discrepancies between the predicted volatile solu-
 683 bilities for melts in equilibrium with mixed H₂O-CO₂ fluids, particularly at higher pressures where
 684 non-ideal behavior is more pronounced. For example, while IM-2012-A predicts similar pure CO₂ and
 685 pure H₂O solubilities to VolatileCalc-Basalt and MagmaSat for MORB1 at 4 kbar (interception with
 686 x and y axis on Fig. 6a), IM-2012-A predicts that melts with ~ 4 wt% H₂O can dissolve more than
 687 twice as much CO₂ as that predicted by VolatileCalc-Basalt.

688 **4.2.3 Pure CO₂**

689 All basaltic compositions and models show a large increase in the solubility of pure CO₂ with
 690 increasing pressure (Fig. 7). The solubility of pure CO₂ is approximately an order of magnitude lower
 691 than for H₂O (compare Fig. 7 with Fig. 5). This solubility difference accounts for the fact that Mid
 692 Oceanic Ridge (MOR) magmas, which have similar concentrations of H₂O and CO₂ (~ 0.07 wt%
 693 H₂O, 0.1-0.2 wt% CO₂; Le Voyer et al., 2019), are almost always CO₂ saturated during crustal stor-
 694 age (Saal et al., 2002) but only exsolve measurable quantities of H₂O if erupted at very low pressures
 695 (Le Voyer et al., 2019).

696 For MORB1, IM-2012-A and H, and VolatileCalc-Basalt lie within, or close to the $\pm 10\%$ error
 697 window on MagmaSat at <5 kbar, and S-2014 lie within $\pm 20\%$. The deviation at higher pressures
 698 is expected, because only P-2006 and MagmaSat are calibrated on large numbers of experiments per-
 699 formed above this pressure (Fig. 1). For example, the relationship between Π and CO₂ solubility
 700 of Dixon (1997) used in VolatileCalc-Basalt was based on experiments at 1 kbar, and Newman and
 701 Lowenstern (2002) suggest that it should not be extrapolated above 5 kbar. Similarly, only the ex-
 702 periments of Jakobsson (1997) in the IM-2012 database were conducted at >5 kbar, and there are
 703 no experiments in the calibration dataset of S-2014 performed at >5 kbar. Unlike for pure H₂O, IM-
 704 2012-A and H predict very similar pure CO₂ solubilities to one another. This reflects the fact the
 705 coefficients for CO₂ between these 2 model versions are very similar (apart from the d_{H_2O} term, which
 706 is multiplied by a zero when calculating pure CO₂ solubility). In contrast, P-2006 plots to significantly
 707 higher pressures than the other models (approximately $2\times$ higher at ~ 8 kbar).

708 MORB2 shows a significantly larger discrepancy between different models at all pressures (Fig.
 709 7b), although S-2014, IM-2012-H and A follow very similar trajectories at >5 kbar. Most notably, P-
 710 2006 predicts that MORB2 dissolves ~ 3370 ppm CO₂ at 2 kbar while MagmaSat predicts only ~ 950
 711 ppm (factor of $3.5\times$). VolatileCalc-Basalt also predicts higher CO₂ solubility relative to MagmaSat by
 712 a factor of $1.8\times$ at 2 kbar.

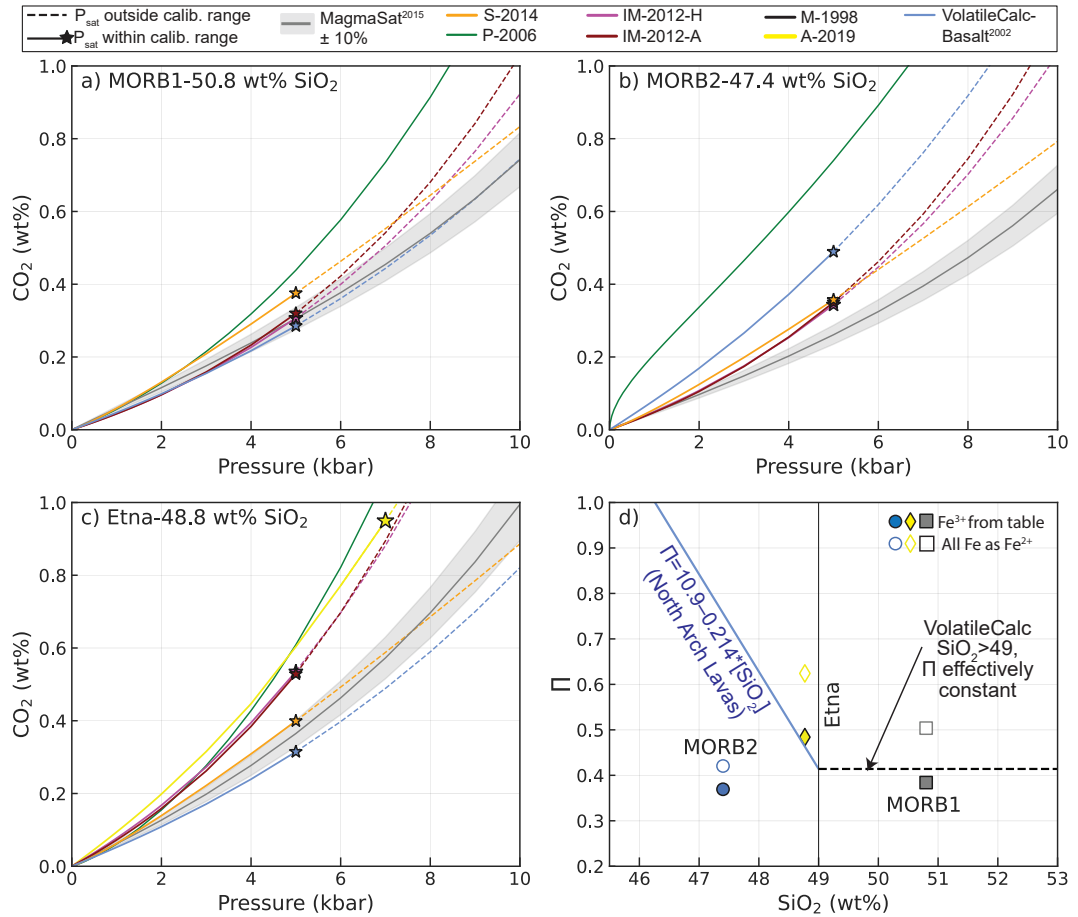


Figure 7. Relationship between pure CO₂ solubility and pressure for three mafic melts at 1200°C: a) MORB1 from Dixon et al. (1995), b) MORB2 from Ghiorso and Gualda (2015), and c) Etna from Allison et al. (2019). Models extrapolated beyond their calibrated pressure range are shown as dashed lines, with the colored star marking the recommended upper calibration limit. d) The relationship between Π and SiO₂ defined by the North Arch lavas is shown in blue (Dixon, 1997). Generally, VolatileCalc-Basalt is applied to melts with >49 wt% SiO₂ by setting SiO₂=49 wt%; the black dashed line represents this extrapolation. These simplified relationships incorporated into VolatileCalc-Basalt (blue and black lines) underestimate the true Π value for Etna, and overestimate it for MORB2.

713 The high CO₂ solubility predictions by P-2006 relative to other models and experimen-
 714 tations has also been noted by Shishkina et al. (2010), Shishkina et al. (2014) and Mangan et al.
 715 (2021). This may result from the fact that the P-2006 has a negative compressibility for the CO₂ fluid
 716 (Ghiorso & Gualda, 2015), as well as the large errors on the CO₂ w coefficients (which likely accounts
 717 for the stronger discrepancy for MORB1 vs. MORB2). Alternatively, Shishkina et al. (2010) suggest
 718 that it may result from the inclusion of anomalously high CO₂ contents from the experiments of Freise

(2004) in the calibration dataset of P-2006 (these values have now been revised to lower numbers, as the original FTIR thickness correction factor is thought to have been incorrect).

The fact that VolatileCalc-Basalt plots close to other models for MORB1 but not MORB2 is a good example of the main caveat of the Π -SiO₂ simplification used in this model to account for the effect of melt composition on CO₂ solubility. For melts with 40–49 wt% SiO₂, VolatileCalc-Basalt assumes that the relationship between CO₂ solubility and SiO₂ is identical to that defined by the North Arch lavas, shown in Π vs. SiO₂ space as a blue line in Fig. 7d. This is a reasonable approximation for the MORB1 composition, which has a Π value similar to North Arch Lavas with 49 wt% SiO₂. However, the MORB2 composition lies significantly below the line defined by North Arch lavas, so has a lower Π value, and therefore a lower CO₂ solubility at a given SiO₂ content compared to the North Arch Lavas. Thus, VolatileCalc-Basalt likely overpredicts the solubility of CO₂ in this melt composition.

Furthermore, VolatileCalc-Basalt predicts that MORB2 dissolves ~ 1.7 times more CO₂ at a given pressure than MORB1. This is because MORB2 has 3.4 wt% less SiO₂ than MORB1, and VolatileCalc-Basalt predicts that CO₂ solubility increases drastically with decreasing SiO₂. P-2006 also predicts that MORB2 dissolves 5–6 \times more CO₂ at 0.4 kbar, and 1.9 \times more at 4 kbar than MORB1. In contrast, the models of S-2014, IM-2012, and MagmaSat predict that MORB1 and MORB2 dissolve similar amounts of CO₂ (MORB2/MORB1= $\sim 0.99\times$, $\sim 1.125\times$ and ~ 0.81 – $0.89\times$ respectively). These three more recent models utilize significantly larger basaltic calibration datasets to parametrize the effect of multiple oxide species melt on CO₂ solubility (Fig. 2), so likely predict more realistic solubility relationships than VolatileCalc-Basalt and P-2006. CO₂ solubility in melt compositions that do not follow a similar trajectory in Π -SiO₂ space as the North Arch Lavas (Fig. 7d) is unlikely to be accurately predicted by VolatileCalc-Basalt.

There is also significant deviation between different models for Etna melts (Fig. 7c), which is far greater than that observed for H₂O (Fig. 5). The A-2019 model, developed specifically for the composition of Etna magmas, predicts much higher CO₂ solubility at a given pressure than VolatileCalc-Basalt, S-2014, and MagmaSat, while P-2006 and IM-2012-H and -A follow similar trajectories to A-2019. The success of both IM-2012 models likely reflects the large number of alkaline compositions in their calibration dataset, including some from Etna. VolatileCalc-Basalt predicts the lowest CO₂ solubility (factor of 0.5–0.6 \times that of Allison). The calculated Π value for Etna lies significantly above the line defined by North Arch lavas (so VolatileCalc-Basalt predicts lower CO₂ solubility; Fig. 7d). However, even the full Π expression of Dixon (1997) is unlikely to be successful, because alkaline magmas show considerable variation in CO₂ solubility at a given Π value (Allison et al., 2019). As S-2014's

752 expression for CO₂ solubility incorporates a Π^* term very similar to the Π term of Dixon (1997), the
 753 deviation of this model from that of A-2019 (0.6–0.7 \times) may also result from variations in CO₂ solubil-
 754 ity that are not incorporated by this simplified melt composition parameter (Allison et al., 2019).

755 Interestingly, MagmaSat also underpredicts CO₂ concentrations at a given pressure relative to
 756 A-2019 by a factor of 0.6–0.7 \times , despite incorporating CO₂ experiments on Etna basalts from Lesne,
 757 Scaillet, Pichavant, and Beny (2011) and Iacono-Marziano et al. (2012) in its calibration dataset. This
 758 is a good example of the main pitfall of comprehensive models such as MagmaSat and P-2006 which
 759 can predict volatile solubility in the entire range of natural silicate melt compositions (Papale et al.,
 760 2006). For any specific melt composition, the model is highly unlikely to be as well tuned as models
 761 calibrated on melts from a specific volcanic center (e.g., Allison et al., 2019) or heavily weighted to-
 762 wards a specific region of compositional space (e.g., Iacono-Marziano et al., 2012, for alkaline basalts).
 763 Tuning MagmaSat to provide a better fit to Etna would almost certainly cause this model to show
 764 larger discrepancies for experiments conducted on different melt compositions.

765 **4.3 Silicic Compositions**

766 **4.3.1 Pure H₂O**

767 All five H₂O models calibrated for silicic magmas (MagmaSat, P-2006, L-2005, VolatileCalc-
 768 Rhyolite and M-1998) predict very similar H₂O concentrations at <1–1.5 kbar for the Mono Craters
 769 rhyolite composition (Fig. 8a, Table 1). At higher pressures, P-2006, and to a much lesser extent L-
 770 2015, show a smaller increase in H₂O solubility with pressure compared to MagmaSat, M-1998 and
 771 VolatileCalc-Rhyolite (the difference in H₂O solubility between all models reaches \sim 4 wt% at 5 kbar).

772 L-2005 and VolatileCalc-Rhyolite have no compositional dependence, so follow identical trajec-
 773 tories for the Mono Craters rhyolite and the peralkaline Aluto rhyolite (Fig. 8b). MagmaSat and M-
 774 1998 also show very similar trends for these two compositions. In contrast, the P-2006 model predicts
 775 higher H₂O concentrations at <2 kbar than the other models for Aluto (and higher H₂O concentra-
 776 tions than predicted for Mono Craters). At >3 kbar, the P-2006 Aluto model shows a rapid reduction
 777 in gradient, and predicts lower H₂O concentrations than L-2005 (although the discrepancy between
 778 these models at > 2 kbar is much less than for Mono Craters).

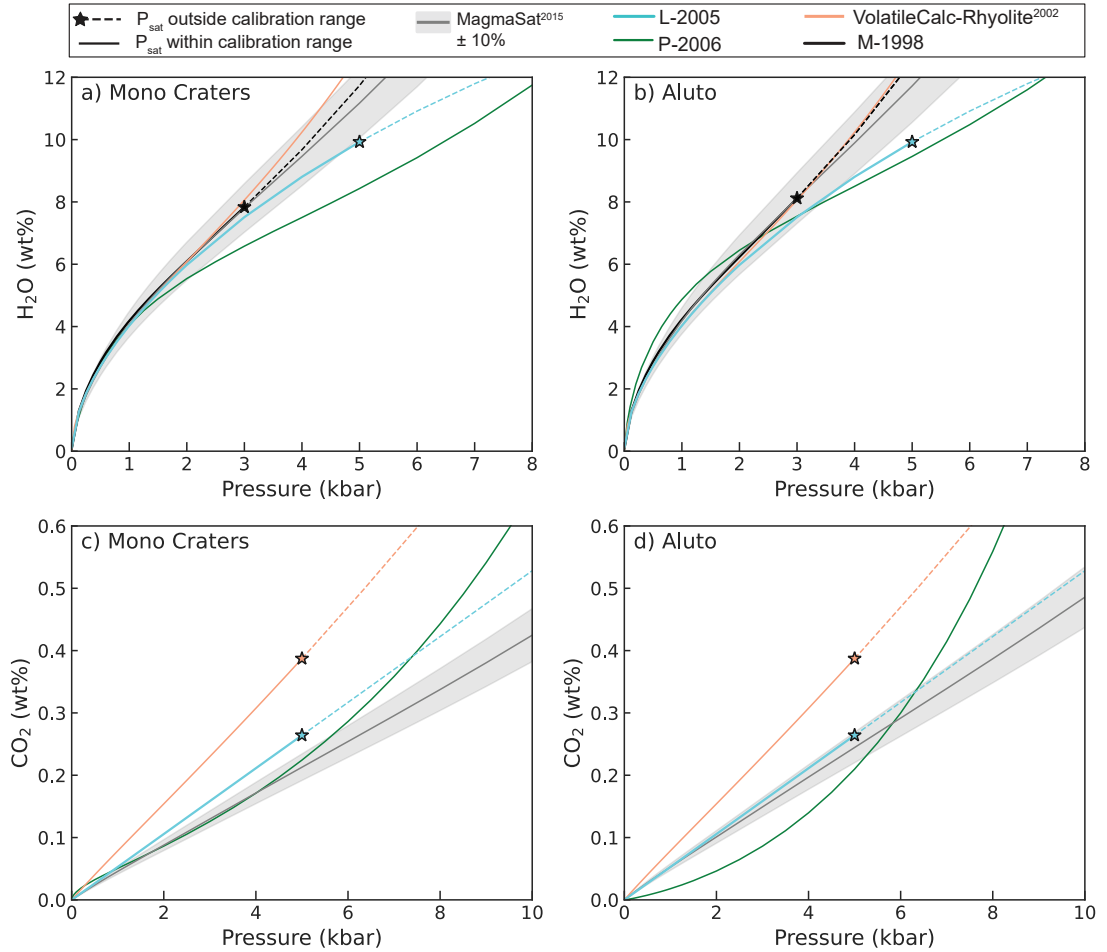


Figure 8. Relationship between pure H₂O (a-b) and pure CO₂ (c-d) solubility and pressure at 800°C for the Mono Lake rhyolite from Liu et al. (2005), and a peralkaline Rhyolite from Aluto in the East African Rift (Iddon and Edmonds, 2020). Models extrapolated beyond their calibrated pressure range are shown as dashed lines, with the colored star marking the recommended upper calibration limit.

4.3.2 Mixed H₂O-CO₂

Differences in the treatment of H₂O-CO₂ mixing for rhyolitic melts are more subtle than for basaltic compositions (Fig. 9). Unlike for basalts, the differences in isobar positions mostly result from large differences between the pure CO₂ solubility predicted by different models rather than treatment of mixing. Only VolatileCalc-Rhyolite assumes ideal mixing of H₂O-CO₂, causing isobars to have a negative gradient at all pressures. L-2005 accounts for non-ideal mixing through the inclusion of a term for the mole fraction of H₂O in the fluid in their expression for CO₂ solubility (equation 5). This empirical representation of non-ideality causes isobars to exhibit a prominent peak at low H₂O contents (Fig. 9). MagmaSat and P-2006, which include a fully non-ideal treatment of mixing, show a far

788 less prominent peak than L-2005. The slight up-tick in the P-2006 isobars at very low H₂O contents is
 789 much smaller than for basaltic compositions (e.g., Fig. 6).

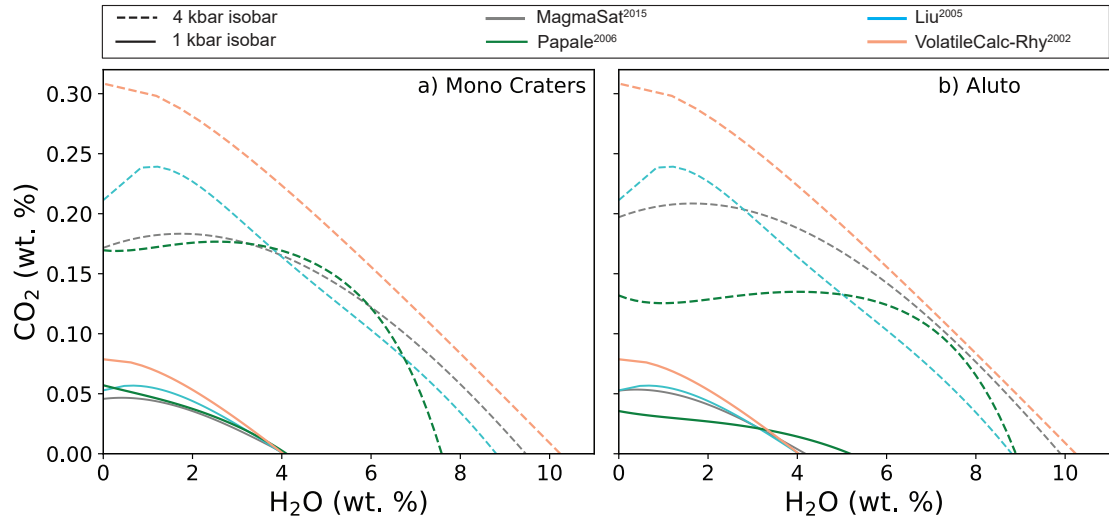


Figure 9. 1 and 4 kbar isobars for Mono Craters (a) and the Aluto Rhyolite (b) at 800°C.

790 4.3.3 Pure CO₂

791 Unlike the relatively good correspondence between rhyolite H₂O models (particularly at low pres-
 792 sures), there is substantial divergence between CO₂ models at all pressures (Fig. 8c, d). For the Mono
 793 Craters rhyolite, VolatileCalc-Rhyolite predicts $\sim 1.8\times$ more dissolved CO₂ than MagmaSat at 2 kbar,
 794 while Liu, P-2006 and MagmaSat plot reasonably close to each other at <5 kbar. As VolatileCalc-
 795 Rhyolite and L-2005 have no compositional dependence, the model lines are identical for Mono Craters
 796 and Aluto. MagmaSat predicts that the Aluto composition has slightly higher CO₂ solubility at a
 797 given pressure compared to the Mono Lake composition (factor of $\sim 1.2\times$), so the discrepancy between
 798 MagmaSat, VolatileCalc-Rhyolite and L-2005 is smaller for Aluto than Mono Craters.

799 The P-2006 model shows a substantially different trajectory for CO₂ vs. pressure compared to
 800 the other three solubility models for both rhyolite compositions, showing a strongly concave-up shape
 801 compared to the near linear trajectory of L-2005 and VolatileCalc-rhyolite, and the slightly concave-up
 802 shape of MagmaSat (Fig. 8c-d). For Mono Craters, P-2006 predicts similar CO₂ solubility to Mag-
 803 maSat at <4 kbar, but rapidly rises to higher CO₂ contents at higher pressures, predicting almost as
 804 much dissolved CO₂ as VolatileCalcRhyolite at ~ 12 kbar (Fig. 8c). For Aluto, the curvature of the
 805 P-2006 model is even more prominent, predicting drastically lower CO₂ contents than all other models
 806 at <6 kbar, and then rapidly rising, predicting higher CO₂ solubility than even VolatileCalc-Rhyolite

at >9 kbar (Fig. 8d). These large deviations between models, as well as the large errors on the interaction terms for CO_2 solubility in MagmaSat (Table 3) demonstrate that while H_2O solubility in rhyolites is well constrained, more work is required to pin down the effect of melt composition on CO_2 solubility at a range of pressures and temperatures.

4.4 Comparisons between Basalts and Rhyolites

* Simon suggested we could move this to the supplement - what are your thoughts? In this section, we briefly discuss the differences in solubility between basalts (using the MORB1 composition) and rhyolites (using the Mono Craters composition). To differentiate the effect of melt composition from temperature (because basaltic melts tend to have higher temperatures), we perform calculations at 800 and 1000°C for Mono Craters, and 1000°C and 1200°C for MORB1.

When all solubility models are compared (4 applicable to rhyolites, 6 to basalts), there is substantial overlap between curves calculated for MORB1 at 1200°C and Mono Craters at 800°C (compare Fig. 11a vs. Fig. 8a). To get around this problem of large differences between models, we compare the predictions from the three models which can be applied to both Rhyolites and Basalts: MagmaSat (Fig. 10a-b), P-2006 (Fig. 10c-d) and VolatileCalc-Basalt and -Rhyolite (Fig. 10e-f).

MagmaSat and VolatileCalc (Rhyolite vs. Basalt) predict that Mono Craters dissolves more H_2O than MORB1, even if these melts are at the same temperature (1000°C). In MagmaSat, the difference in solubility between Basalt and Rhyolite is enhanced by the fact that basalts tend to be hotter (the curves get closer when compositions are compared at 1000°C). In contrast, P-2006 predicts that Mono craters at 800°C dissolves less H_2O than MORB1 at 1200°C, although their solubilities are nearly identical when compared at 1000°C.

MagmaSat and P-2006 predict that MORB1 dissolves more CO_2 than Mono Craters, with the difference increasing rapidly as a function of pressure. In contrast, VolatileCalc predicts that, at 800°C, Mono Craters dissolves more CO_2 than MORB1 at 1000°C or 1200°C, while the model predicts very similar CO_2 solubility when Mono Craters and MORB1 are both at 1000°C.

Overall, these comparisons demonstrate that at <5 kbar, the difference in solubility between basalts and rhyolites is relatively subtle, and easily overwhelmed by differences in predictions from different solubility models (particularly given some models predict that solubility increases with temperature, and others predict the opposite).

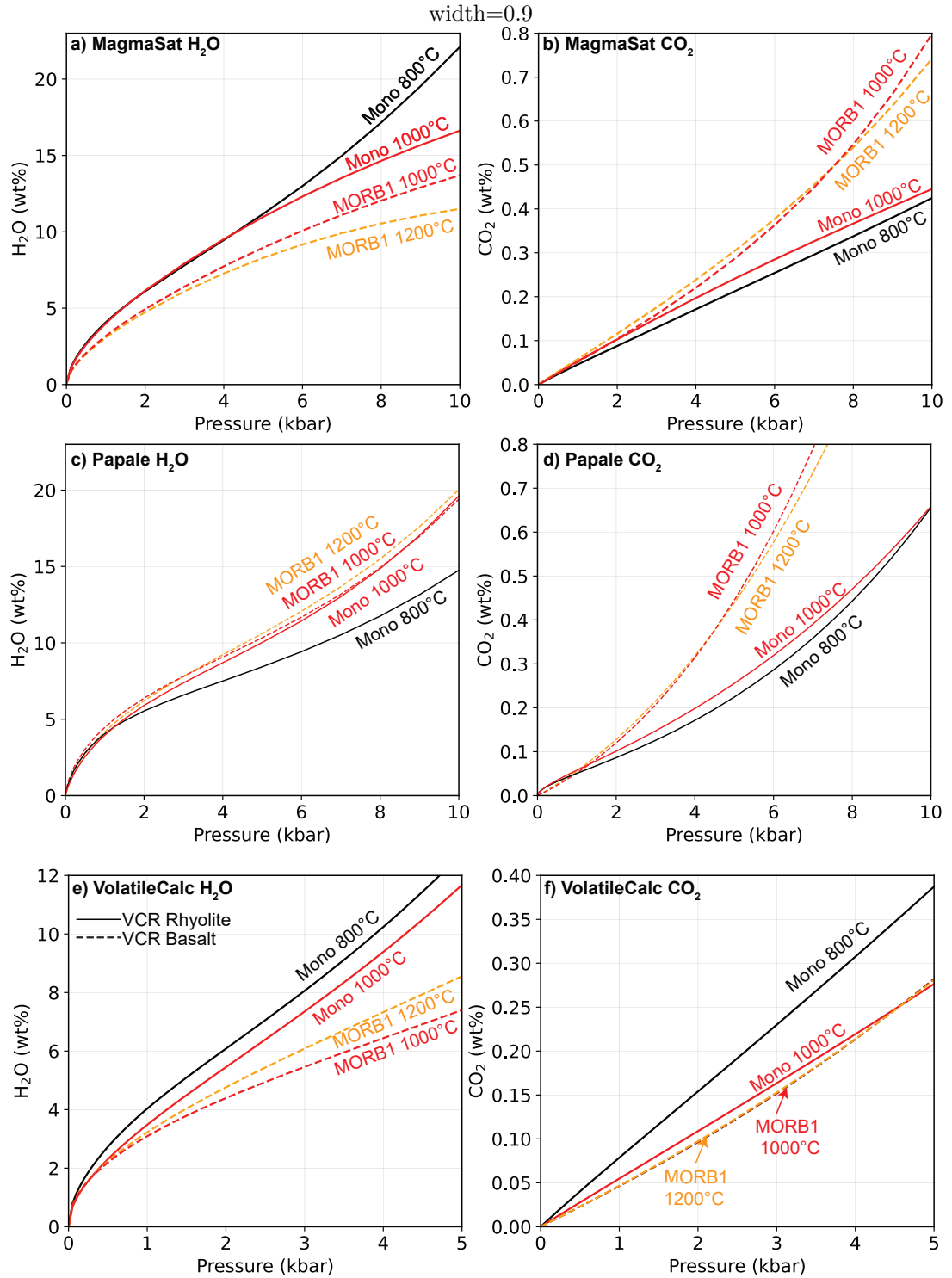


Figure 10. Comparison of solubility of Basalt (represented by MORB1) to Rhyolite (represented by Mono Craters) using MagmaSat (a-b), P-2006 (c-d) and VolatileCalc-Basalt and Rhyolite (d-e). Solubility curves are calculated for 1200°C and 1000°C for basalt, and 1000°C and 800°C for rhyolite.

5 Model Sensitivities

In this section, we explore the sensitivity of the different models to parameters such as temperature and variable proportions of H₂O and CO₂. Specifically, we consider how these inputs affect calculations of the pressure at which a melt inclusion was trapped (termed the saturation pressure). To calculate saturation pressures, the initial concentration of major and volatile elements as well as the temperature must be estimated at the time of melt inclusion entrapment. However, a number of processes, such as crystallization of the host mineral on the wall of the inclusion (termed post-entrapment crystallization, or PEC), growth of a vapour bubble or daughter phases within the inclusion, and diffusive re-equilibration with a changing carrier liquid composition can make it difficult to reconstruct initial major element and volatile contents (Lowenstern, 1995). Similarly, diffusive re-equilibration of the major elements in the melt inclusion and host mineral, as well as the errors associated with mineral-melt and melt-only thermometers, can lead to uncertainties in the entrapment temperature, which propagates into the saturation pressure. By investigating the effect of varying these parameters within realistic limits, insight can be gained into the uncertainties associated with estimating magma storage depths using melt inclusions.

5.1 Relationship between saturation pressure and dissolved H₂O content

Melt inclusion H₂O contents are vulnerable to diffusional re-equilibration with the melt surrounding the crystal (here termed the carrier melt), because of the fast diffusion rate of H⁺ through silicate minerals (Portnyagin et al., 2008). H⁺ diffusion is particularly fast in olivine (Gaetani et al., 2012), with melt inclusions losing significant amounts of water in hours to days (Bucholz et al., 2013). Thus, this discussion focuses on mafic compositions, where olivine-hosted melt inclusions are frequently analysed.

In relatively H₂O-poor mafic systems such as MORs and ocean islands (e.g., Hawai'i), diffusive re-equilibration can increase melt inclusion H₂O contents if crystals are mixed into more H₂O-rich carrier melts (Hartley et al., 2015), or, more commonly, cause melt inclusion H₂O contents to drop if the crystal is in contact with a carrier melt that has degassed its H₂O upon eruption (Gaetani et al., 2012; Bucholz et al., 2013). To assess how uncertainty in initial H₂O contents translates into errors on saturation pressures, we calculate saturation pressures for the MORB1 melt composition with 200, 1000, and 3000 ppm CO₂ (representing melt inclusions trapped at low, medium and high pressures) for H₂O contents between 0–1.5 wt% (Fig. 11a-c). CO₂ contents are held constant while H₂O contents are varied, simulating the changes undergone by melt inclusions during diffusive re-equilibration (which strongly affects H₂O contents in the inclusion, but does not change the total CO₂ budget of the inclusion).

869 The relationship between saturation pressure and dissolved H₂O predicted by each solubility
 870 model is strongly dependent on the amount of CO₂ in the melt, and therefore the pressure. To quan-
 871 tify model sensitivity to H₂O, saturation pressures calculated at H₂O=1.5 wt% are divided by the
 872 saturation pressure calculated at H₂O=0 wt%, representing the possible discrepancy between the cal-
 873 culated saturation pressure and the real saturation pressure for melt inclusions which have undergone
 874 complete H⁺ re-equilibration with a fully degassed erupted melt at 0 bar. At low pressures (200 ppm
 875 CO₂), all models show a decrease in calculated saturation pressure with decreasing H₂O contents, with
 876 entrapment pressures being 1.2–1.8× higher before complete H₂O-loss (Fig. 11a). MagmaSat shows
 877 the strongest sensitivity to H₂O content, and both IM-2012 models the weakest. At moderate pres-
 878 sures (1000 ppm CO₂), loss of H₂O causes a significantly smaller decrease in saturation pressure for
 879 VolatileCalc-Basalt, P-2006 and S-2014 compared to the 200 ppm CO₂ scenario (Fig. 11b, 1.1–1.2×).
 880 Saturation pressures for 1000 ppm CO₂ calculated using MagmaSat and IM-2012-H first decrease, then
 881 increase with H₂O loss. This is because these models predict that the maximum CO₂ solubility occurs
 882 at H₂O contents at ~0.5–1.25 wt% (see Fig. 6). This effect is also seen in terms of the change in slope
 883 of these models at 200 ppm, but is more subtle because lower pressure isobars are less prominently
 884 domed (Fig. 6). At higher pressures (3000 ppm CO₂), VolatileCalc-Basalt, P-2006 and S-2014 are only
 885 1.04–1.1× higher at 1.5 wt% vs. 0 wt% H₂O. In contrast, saturation pressures continually increase
 886 with H⁺-loss for IM-2012-H and -A and MagmaSat, because these models predict that maximum CO₂
 887 solubility is found at H₂O contents >1.5 wt% at these pressures (Fig. 6).

888 Within a given suite of MORB or OIB melt inclusions, the range of measured H₂O contents, and
 889 the uncertainty involved in reconstructing initial H₂O contents following diffusional re-equilibration,
 890 is likely significantly smaller than the 1.5 wt% H₂O considered here (Koleszar et al., 2009; Sides et
 891 al., 2014a; Wieser et al., 2020). Thus, except at low pressures (<1 kbar), uncertainties in saturation
 892 pressures due to diffusive re-equilibration of H₂O in relatively anhydrous systems are likely compa-
 893 rable to the analytical errors associated with the measurements of volatile species by FTIR or SIMS
 894 (±5-10%), errors on each solubility model (~10-20%), and significantly smaller than the differences
 895 between solubility models.

896 The higher H₂O contents of melt inclusions from subduction zones (~2–6 wt%; Plank et al.,
 897 2013) mean that substantially more H₂O can be lost following diffusive re-equilibration with a de-
 898 gassed carrier melt upon eruption. Additionally, arc melt inclusions are vulnerable to diffusive re-
 899 equilibration during crustal storage. This is because these relatively hydrous magmas saturate in a
 900 H₂O-rich fluid at high pressures in the crust. Thus, as a melt and its crystal cargo ascends from a
 901 deeper storage reservoir to a shallower storage reservoir, significant quantities of H₂O will be degassed

902 and the H₂O contents of melt inclusions will rapidly diffusively re-equilibrate with the new carrier melt
 903 composition (Gaetani et al., 2012). Even if samples are rapidly quenched upon eruption (preventing
 904 syn-eruptive H₂O diffusion), only the volatile contents of melt inclusions trapped in the shallowest
 905 storage reservoir can be reliably converted into saturation pressures (Gaetani et al., 2012). This con-
 906 trasts with more H₂O-poor systems such as mid-oceanic ridges and oceanic islands, where H₂O only
 907 degasses in the upper few hundred metres of the crust, so ascent to a shallower reservoir is not accom-
 908 panied by a drop in melt H₂O contents (although diffusive re-equilibration could occur if the resident
 909 melts in the shallower reservoir have different H₂O contents; Hartley et al., 2015).

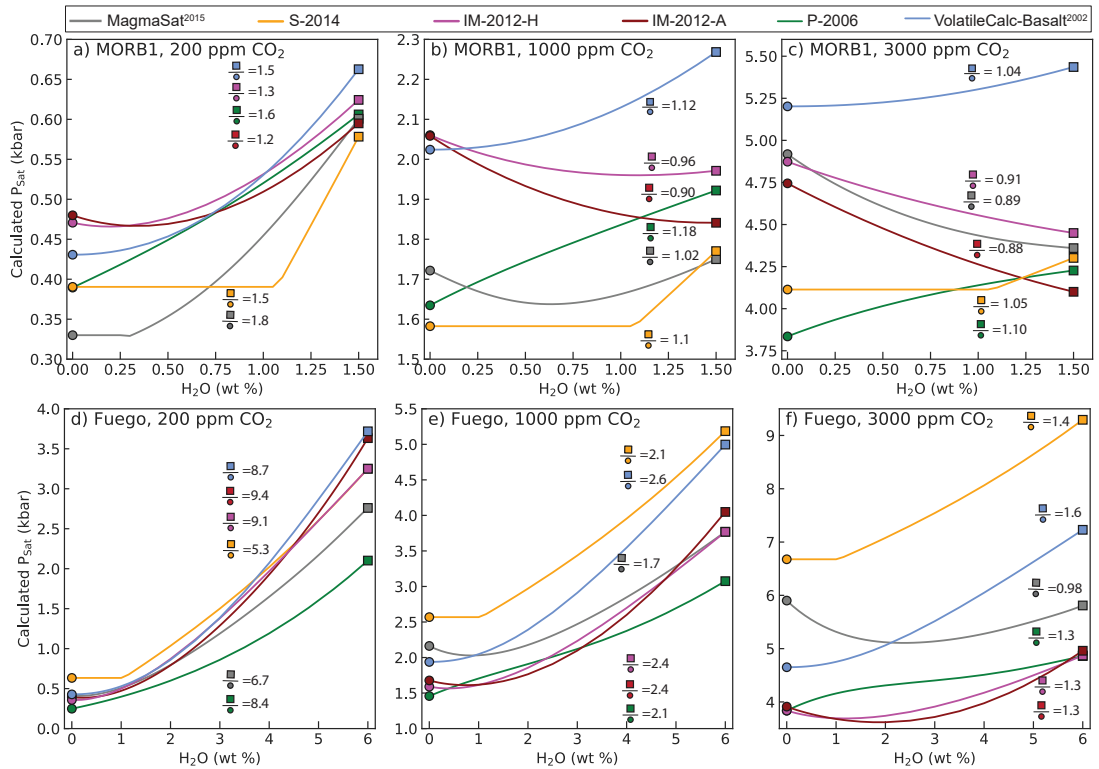


Figure 11. a-c) Relationship between saturation pressure and melt H₂O content for water-poor melts (using the MORB1 composition at 1200°C). Three different melt CO₂ contents (200, 1000, 3000 ppm) are shown in part a, b and c) respectively. The numbers on the graphs show the saturation pressure at 1.5 wt% H₂O (square symbol) divided by the saturation pressure at 0 wt% H₂O for each model. d-f) Sensitivity tests using the composition of a Fuego melt inclusion (Table 1) at 1000°C, and H₂O contents between 0–6 wt%.

910 To investigate the effect of H₂O re-equilibration on melt inclusion saturation pressures in arcs,
 911 we repeat the sensitivity test described above, using the major element composition of a Fuego melt

inclusion with 49.7 wt% SiO₂ from Lloyd et al. (2013, Table 1) and H₂O contents between 0–6 wt% (Fig. 11d-f). For melt inclusions with 200 ppm CO₂, complete diffusive loss of H₂O may result in saturation pressures being underestimated by a factor of $\sim 5\text{--}10\times$. Even for melts with 3000 ppm CO₂ (the highest pressure regime examined, and thus the best case scenario), diffusive loss can affect saturation pressures by factors of 0.93–1.6 \times (similar in magnitude to the sensitivity displayed by H₂O-poor melts at the lowest pressures; Fig. 11a vs. f). Only saturation pressures calculated in MagmaSat for the most CO₂-rich melts displays variations with variable H₂O-loss similar in magnitude to analytical errors. Thus, it is extremely important to determine whether melt inclusions have undergone H₂O-loss during ascent to a shallower reservoir or syn-eruptive degassing before using saturation pressures to deduce magma storage depths in water-rich volcanic systems.

5.2 Relationship between saturation pressure and dissolved CO₂ content

Estimating the initial CO₂ contents of melt inclusions is also challenging. While the total CO₂ content of the inclusion is not affected by diffusive re-equilibration, CO₂ may be partitioned from the melt phase into a vapour bubble. Cooling following melt inclusion entrapment is accompanied by the formation of a denser mineral phase from a less dense silicate melt, and differential thermal contraction of the melt and crystal. These processes cause the internal pressure of the inclusion to drop (Steele-Macinnis et al., 2011; MacLennan, 2017), driving the nucleation and growth of a vapour bubble. This may be enhanced by the diffusive loss of H₂O, which also causes a pressure drop in the melt inclusion because of the high molar volume but low molecular weight of H₂O (Gaetani et al., 2012; Aster et al., 2016). A drop in pressure, combined with a decrease in the solubility of CO₂ in the melt phase because of changes to the major element composition accompanying post-entrapment crystallization, causes CO₂ to partition strongly into the vapour bubble (L. R. Moore et al., 2015; Steele-Macinnis et al., 2011; MacLennan, 2017; Wieser et al., 2020). A number of recent studies have quantified the amount of CO₂ in vapour bubbles using Raman Spectroscopy, and demonstrated that between 15–99% of the total CO₂ budget of the inclusion may be held within the bubble (Hartley et al., 2014; L. R. Moore et al., 2015; Wieser et al., 2020; Allison et al., 2021). This means that a large proportion of literature melt inclusion data, which only measured the CO₂ content of the glass phase, may have significantly underestimated initial CO₂ contents (and therefore saturation pressures).

In relatively H₂O-poor systems such as Hawai'i and Iceland, where melt inclusion CO₂ contents have the dominant control on saturation pressures (shown by the near horizontal slopes of most model isobars at low H₂O contents; Fig. 6), it is readily apparent that saturation pressures will be significantly underestimated if a CO₂-rich vapour bubble is not measured. However, in arcs, H₂O contents inferred from melt inclusions or mineral hygrometers are sometimes used to place first order con-

945 straints on saturation pressures (e.g. Plank et al., 2013; Blundy & Cashman, 2005; Goltz et al., 2020).
 946 However, even in very H₂O-rich melts, the non-vertical orientation of isobars at high H₂O contents
 947 implies that CO₂ contents still have an important role in determining the saturation pressure (Fig. 6).
 948 Additionally, only a very small number of studies have measured CO₂ in melt inclusion vapour bubbles
 949 from arc systems (L. R. Moore et al., 2015; Aster et al., 2016; Venugopal et al., 2020; Mironov et al.,
 950 2020). Thus, it is vital to determine the effect of CO₂ on saturation pressures in H₂O-rich systems.

951 Using a similar method to that for H₂O discussed above, we use the composition of a Fuego
 952 melt inclusion from Lloyd et al. (2013). They report a mean melt inclusion glass CO₂ content of 340
 953 ppm (range of 59–786 ppm). However, Raman analyses of vapour bubbles in the same sample set by
 954 L. R. Moore et al. (2015) reveals that 993–4776 ppm of CO₂ has migrated from the glass phase into
 955 the vapour bubble following melt inclusion entrapment. Thus, we calculate saturation pressures for
 956 CO₂ contents between 0–5000 ppm at 1000°C for 2, 4 and 6 wt% H₂O respectively (after Plank et al.,
 957 2013).

958 S-2014 is most sensitive to CO₂ content, and IM-2012-H and -A the least sensitive. With increas-
 959 ing H₂O, the change in saturation pressure with increasing CO₂ becomes smaller, but is still significant
 960 (Fig. 12). For example, calculating a H₂O-only saturation pressure for a melt inclusion with H₂O=6
 961 wt% in MagmaSat would underestimate magma storage depths by a factor of 1.5 if the melt inclusion
 962 had 1000 ppm CO₂, and a factor of 3 if the inclusion had 5000 ppm CO₂. For a melt inclusion with 4
 963 wt% H₂O, H₂O-only saturation pressures underestimate by a factor of ~2.2 for 1000 ppm CO₂, and
 964 5.4 for 5000 pm CO₂. These variations in saturation pressure overwhelm the other errors associated
 965 with melt inclusion barometry (e.g., uncertainty in crustal density profiles, analytical errors associ-
 966 ated with volatile measurements by FTIR or SIMS, differences between solubility models). Further
 967 investigation of the prevalence of CO₂-rich vapour bubbles in arc lavas is clearly required to have con-
 968 fidence in published barometric estimates in studies which did not measure the vapour bubbles, or
 969 used mineral hygrometers.

970 Saturation pressures in rhyolitic magmas are also very sensitive to melt CO₂ contents (Fig. 13).
 971 For example, saturation pressures calculated for 1000 ppm CO₂ vs. 0 ppm CO₂ differ by factors of
 972 5.7–8.9× for 2 wt% H₂O, and 1.6–2× for 6 wt% H₂O. Even saturation pressures calculated for 300
 973 ppm CO₂ (0.03 wt%) vs 0 ppm CO₂ are a factor of ~2-3× higher for 2 wt% H₂O, and still 1.2-1.3×
 974 higher for 6 wt% H₂O. The strong effect of CO₂ on saturation pressure is important to recognise when
 975 calculating saturation pressures using only melt H₂O contents, such as studies using mineral-melt
 976 hygrometers (Waters & Lange, 2013), or volatiles-by-difference methods to estimate H₂O contents
 977 of melt inclusions. It is also interesting to note that, to our knowledge, there are no published Ra-

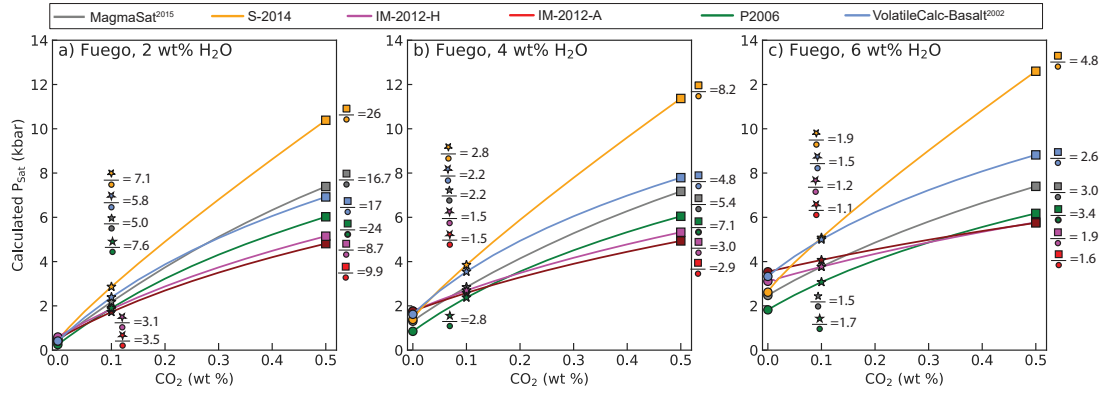


Figure 12. Relationship between saturation pressures and melt CO_2 contents for water-rich melts (using the composition of a Fuego melt inclusion at 1000°C ; Table 1). Three different melt H_2O contents (2, 4 and 6 wt%) are shown in part a, b and c) respectively. The numbers on the graphs show the saturation pressure at 5000 ppm CO_2 (square symbol) divided by the saturation pressure at 0 ppm CO_2 (square), and the saturation pressure at 1000 ppm (star symbol) divided by the saturation pressure at 0 ppm CO_2 (square) for each model.

978 man measurements of CO_2 in vapour bubbles which grew after melt inclusion entrapment in dacitic-
 979 rhyolitic melt compositions. While the extremely low CO_2 contents of many rhyolitic melt inclusions
 980 are commonly interpreted to result from shallow crustal storage, it is becoming increasingly recog-
 981 nised that mafic melt inclusions with CO_2 below detection limit contain large quantities of CO_2 in
 982 the bubble (Wieser et al., 2020). Thus, examination of vapour bubbles in melt inclusions from more
 983 silicic systems (e.g., Fig. 1 of Lowenstern, 2001) is likely warranted, to rule out the possibility that
 984 these melts crystallized at greater depths than calculated using measurements of CO_2 hosted in just
 985 the glass phase.

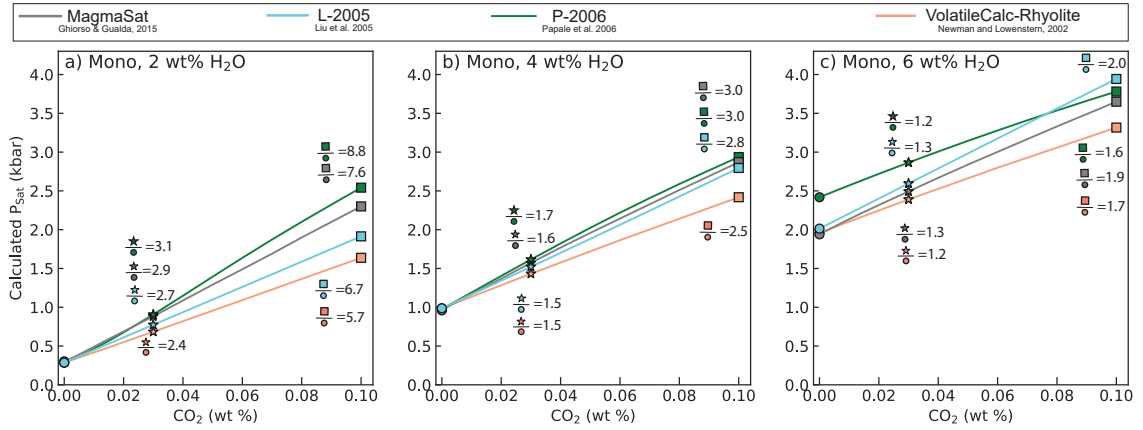


Figure 13. Sensitivity of saturation pressures for the Mono Craters rhyolite to melt CO₂ contents at three different H₂O contents (2, 4 and 6 wt%). Ratios of saturation pressures at 0.02 wt% CO₂ (300 ppm; star symbol) vs. 0 wt% (circle), and 0.1 wt% (1000 ppm; square symbol) vs. 0 wt% CO₂ are shown on the figure.

5.3 Sensitivity to Temperature

The temperature of the melt at the time of entrapment is another source of uncertainty when calculating saturation pressures, as melt or mineral-melt thermometers are relatively imprecise. For example, the liquid MgO thermometer of Putirka (2008) has a standard error of $\pm 71^\circ\text{C}$, while their clinopyroxene-liquid thermometer has a standard error of $\pm 61^\circ\text{C}$. Changes in the major element compositions of the melt inclusion during PEC and diffusive H₂O-loss can also introduce errors when estimating entrapment temperatures (as most thermometers are highly sensitive to the MgO and H₂O content of the melt). Additionally, almost all solubility experiments are performed at supra-liquidus conditions, while melt inclusion formation must take place at sub-liquidus conditions, so extrapolation to lower temperatures is an unfortunate necessity.

To investigate the sensitivity of different models to temperature, we calculate the 0.5 and 2 kbar isobars for the MORB1 composition at 1000°C and 1400°C. Only S-2014 shows no temperature dependency, because there is neither a temperature or fugacity term in their equations. Interestingly, there is considerable disagreement between the other models as to whether a hotter magma dissolves more or less volatiles. MagmaSat and P-2006 predict an increase in pure CO₂ solubility with increasing temperature, while VolatileCalc-Basalt and IM-2012-A and -H predict a much smaller decrease (Fig. 14a-c). In all models but IM-2012-A, isobars calculated for different temperatures intercept at higher H₂O contents, so the temperature dependency of H₂O solubility is opposite to that for CO₂ solubility. To visualize the effect of these trends on calculated saturation pressures for the MORB1 composition,

1005 the calculated saturation pressures for melts with volatile contents represented by the yellow and cyan
 1006 stars on Fig. 14b are plotted against temperature (between 1000-1400°C; Fig. 14c-d). MagmaSat and
 1007 P-2006 show the strongest temperature sensitivity, with a slope opposite to that of the more subtle
 1008 changes predicted by VolatileCalc-Basalt and IM-2012.

1009 The lack of consensus as to whether increasing temperature increases or decreases the solubility
 1010 of H₂O and CO₂ indicates that this effect is relatively subtle, and overwhelmed by analytical errors
 1011 associated with measuring experimental products (and other sources of experimental scatter; e.g., Fig.
 1012 16a-b). This makes it very difficult for empirical models to fully constrain the temperature sensitiv-
 1013 ity, particularly given that the experiments conducted by any given study are usually performed at a
 1014 single temperature. For example, all the experiments used to calibrate the VolatileCalc-Basalt model
 1015 were conducted at 1200°C, so the temperature dependency of this model results from the fugacity
 1016 function, and 1/T terms from Dixon et al. (1995), rather than experimental observations.

1017 IM-2012 is calibrated on experiments mostly performed at 1200-1300°C (with a few spanning
 1018 1100-1400°C). Their empirical expressions contain $C_{H_2O} \times \frac{P}{T}$ and $C_{CO_2} \times \frac{P}{T}$ terms in their expressions
 1019 for H₂O and CO₂ solubility respectively (equation 11 and 15), where C_{H_2O} and C_{CO_2} are empirically-
 1020 derived constants, and P and T are pressure and temperature. In the hydrous model, C_{H_2O} is negative
 1021 (-0.02 ± 0.02), so H₂O solubility increases with increasing temperature, while in the anhydrous model
 1022 C_{H_2O} is positive (0.02 ± 0.02), so H₂O solubility decreases with increasing temperature (Fig. 14). As
 1023 the magnitude of these coefficients is small, the temperature effect on H₂O solubility is small, and
 1024 only visible at higher pressures (because of the P part of these terms; Fig. 14a vs. c). It is also worth
 1025 noting that these coefficients in both models are within error of zero, showing that the experimental
 1026 dataset used to calibrate this model showed very little evidence for a change in H₂O solubility with
 1027 temperature. In both the hydrous and anhydrous models, C_{CO_2} is positive (0.12 ± 0.02 and 0.14 ± 0.02
 1028 respectively) and larger in magnitude than C_{H_2O} , so CO₂ solubility decreases with increasing tempera-
 1029 ture (see Fig. 14c).

1030 The approach taken by S-2014 and A-2019 is an interesting alternative when constructing sol-
 1031 ubility models. While S-2014 is calibrated on experiments conducted between 1200–1300°C for CO₂,
 1032 and 1200–1250°C for H₂O, their solubility equations contain no temperature or fugacity term. Instead,
 1033 these authors suggest that the H₂O model should ideally be used between 1150–1250°C. They perform
 1034 additional tests on experiments between 1050–1400°C not used in the calibration, and show that their
 1035 model predicts H₂O solubility within $\pm 10\%$ for 78% of experiments for this wider temperature range.
 1036 The S-2014 testing dataset for CO₂ only has a slightly different temperature range than the calibra-
 1037 tion dataset (1170–1250°C vs. 1200-1250°C), so they do not suggest an expanded temperature range

1038 for CO₂. Similarly, the spreadsheet for A-2019 (and the implementation of this model in VESIcal)
1039 performs all calculations at 1200°C, regardless of the user-input temperature. Allison et al. (2019)
1040 suggest that this approach is likely valid between 1000–1400°C.

1041 Unlike empirical models, the temperature sensitivity of P-2006 and MagmaSat arises from the
1042 entropy differences between melt and fluid components. Given the limited experimental evidence for
1043 changes in solubility with temperature, the directionality inferred by thermodynamical models is more
1044 likely to be correct, as the relative entropy differences between components are easier to constrain than
1045 deconvoluting subtle differences between the solubility of CO₂ and H₂O in experiments run at different
1046 temperatures, and because all empirical models are being extrapolated to lower temperatures than the
1047 supra-liquidus experiments used to calibrate them. Overall, although the differences between mod-
1048 els is interesting, and important to recognise when extrapolating beyond the range of the calibration
1049 dataset, the uncertainty that temperature variations introduce to saturation pressure calculations are
1050 relatively small for mafic melts. For example, an uncertainty in the initial entrapment temperature
1051 of $\pm 100^\circ\text{C}$ introduces an uncertainty similar to that associated with in-situ measurements of melt
1052 inclusion volatile contents ($\pm 5\text{-}10\%$; Fig. 14).

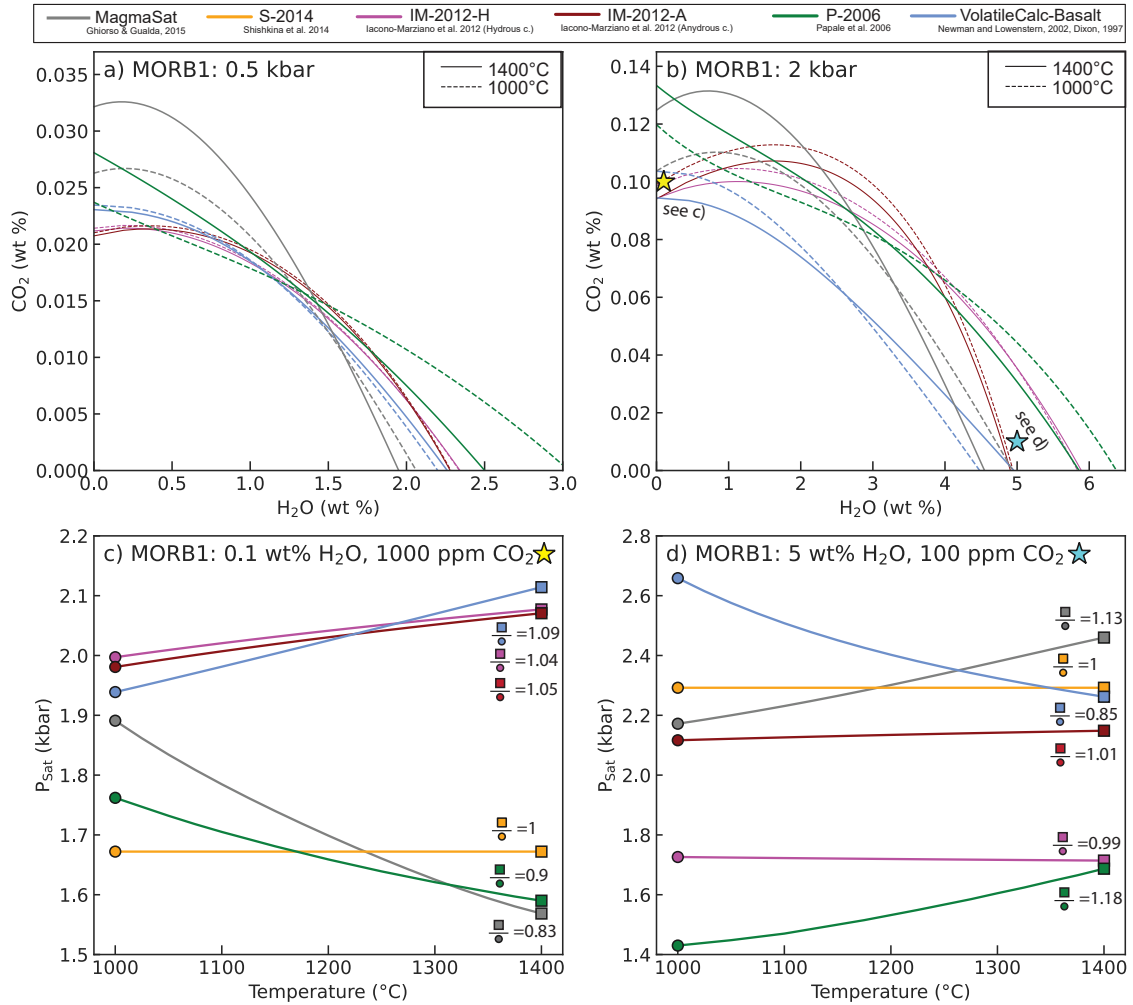


Figure 14. Evaluating model sensitivity to temperature (using the MORB1 composition). a-b) Isobars evaluated at 1000 and 1400°C and 0.5 and 2 kbar. c) Relationship between saturation pressure and temperature for a melt with 1000 ppm CO₂, 0.1 wt% H₂O (yellow star on a), d) 100 ppm CO₂, 5 wt% H₂O (cyan star on b). Ratios of saturation pressures at 1400°C (square symbol) to 1000°C (circle symbol) are shown on the figure.

1053 Similarly, temperature sensitivity in rhyolitic melts was evaluated by calculating isobars at 0.5
 1054 and 2 kbar for 700 and 900°C using the Mono Craters rhyolite composition. As for the basaltic exam-
 1055 ple, the directionality and magnitude of effect of temperature on saturation pressures for melts with
 1056 volatile contents indicated by the colored stars is shown in Fig. 15c-d for temperatures between 700
 1057 and 1000°C. VolatileCalc-Rhyolite shows the strongest temperature sensitivity, predicting that the sol-
 1058 ubility of CO₂ decreases with increasing temperature. L-2005 also predicts decreasing CO₂ solubility
 1059 with increasing temperature, although this effect is smaller than in VolatileCalc-Rhyolite. Decreasing
 1060 solubility of molecular CO₂ with increasing temperature was demonstrated experimentally by Fogel

1061 and Rutherford (1990). In contrast, the two thermodynamic models, P-2006 and MagmaSat, predict
 1062 that pure CO₂ solubility increases with increasing temperature. The effect of temperature on H₂O
 1063 solubility is smaller in VolatileCalc-Rhyolite than for CO₂, but shows the same directionality. At low
 1064 pressures (~0.5 kbar), isobars for MagmaSat and P-2006 intercept, so increasing temperatures causes
 1065 more CO₂, but less H₂O to dissolve, while at higher pressures, higher temperatures increases the solu-
 1066 bility of both volatile species.

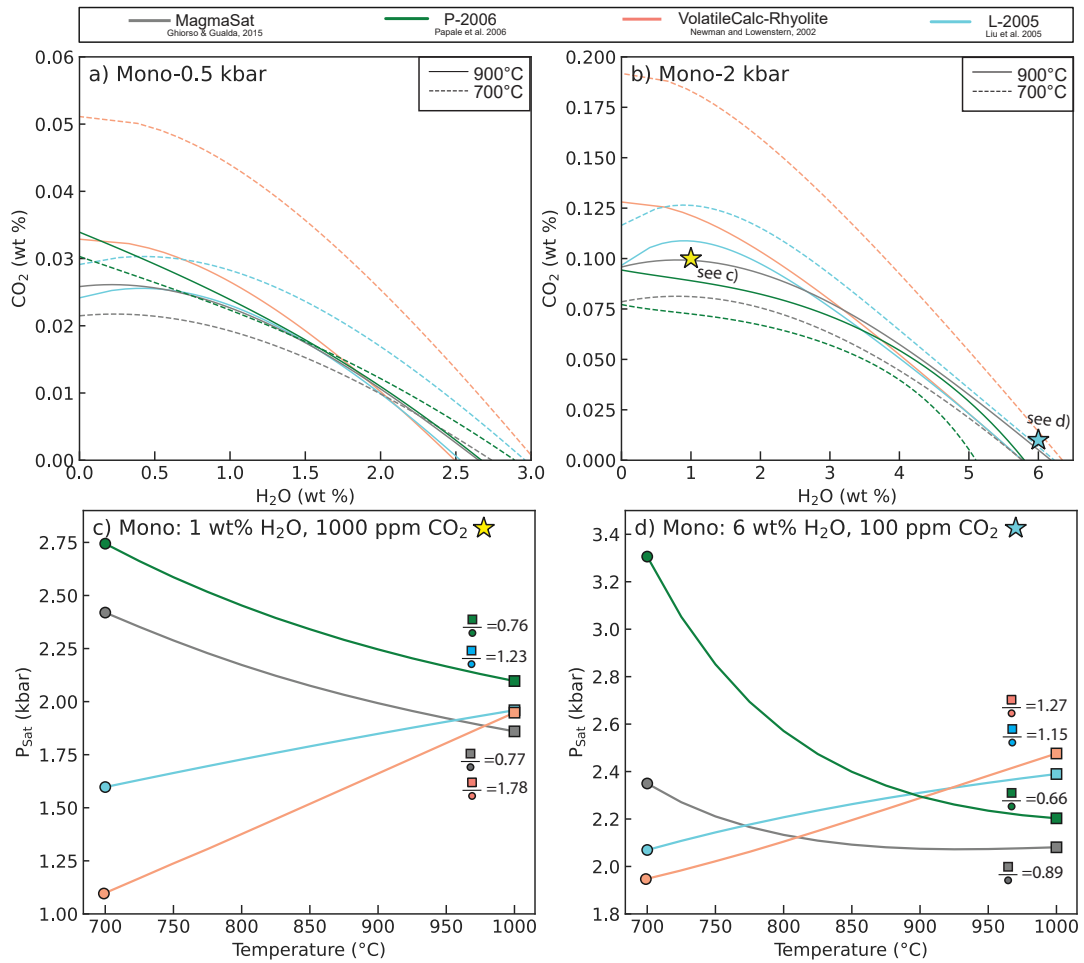


Figure 15. Sensitivity of saturation pressures for the Mono Craters rhyolite to temperature. a-b) Isobars calculated for different solubility models at 700 and 900°C and 0.5 and 2 kbar. c) Relationship between saturation pressure and temperature for a melt with 1000 ppm CO₂, 1 wt% H₂O (yellow star in b), d) 100 ppm CO₂, 6 wt% H₂O (cyan star in b). Ratios of saturation pressures at 900°C (square symbol) to 700°C (circle symbol) are shown on the figure.

1067 It is noteworthy that the temperature sensitivity of CO₂ solubility predicted by L-2005 and
1068 VolatileCalc-Rhyolite is much greater than that shown by any of the basaltic models (Fig. 14d-e vs.
1069 Fig 15d-e), and significant considering other sources of error associated with saturation pressure calcu-
1070 lations. MagmaSat and P-2006 also show a far greater sensitivity to H₂O solubility between 700-850°C
1071 in rhyolites than any of the basaltic models between 1000-1400°C (Fig. 14f vs. Fig 15f), although the
1072 sensitivity to temperature decreases between 800-900°C.

1073 Given the contrasting behaviour of empirical and thermodynamic models, and the relatively
1074 strong effect of temperature in rhyolitic melts, we suggest that users proceed with caution when ex-
1075 trapolating empirical models to temperatures significantly lower or higher than the calibration tem-
1076 perature of each model. It may be best to use empirical models at the calibration temperature (e.g.,
1077 1200°C for VolatileCalc-Basalt, 850°C for VolatileCalc-Rhyolite), which is the approach used by in the
1078 models of S-2014 and A-2019, rather than introduce a temperature sensitivity with the wrong sign.
1079 This is discussed in further detail for VolatileCalc-Rhyolite in section 6.

1080 **6 Intermediate Compositions**

1081 In this section, we compare the predictions of different solubility models for intermediate melt
1082 compositions (andesites to dacites). Lavas with these compositions are dominant within subduction
1083 zones, and volcanoes erupting these compositions are extremely hazardous. Yet, there is a notable
1084 paucity of solubility experiments for andesitic and dacitic compositions relative to basalts and rhyolites
1085 (Fig. 2; King & Holloway, 2002; Botcharnikov et al., 2006). This section builds on the sensitivity tests
1086 performed in section 5 to evaluate possible discrepancies between model outputs and experimental
1087 constraints.

1088 The calibration dataset of MagmaSat has the broadest coverage of andesitic-dacitic composi-
1089 tions of all the models described here (although it is far from extensive). While there are a number
1090 of pure H₂O experiments, MagmaSat only includes one pure CO₂ experiment on an andesitic melt
1091 (conducted at 1 GPa; King & Holloway, 2002), and no pure CO₂ experiments on dacitic melts. Sim-
1092 ilarly for mixed H₂O-CO₂, the calibration dataset for andesitic melts includes only four experiments
1093 from King and Holloway (2002), 21 from Botcharnikov et al. (2006) and three from Botcharnikov et
1094 al. (2007). Dacitic liquids are only represented by the 12 experiments on mixed H₂O-CO₂ solubility
1095 by Behrens et al. (2004). As the P-2006 model had a decade fewer experimental constraints available
1096 for calibration, it only includes the one pure CO₂ and four mixed H₂O-CO₂ andesitic experiments of
1097 King and Holloway (2002). The IM-2012 model includes two pure H₂O experiments that lie within
1098 the andesite field on a TAS diagram, but no H₂O-CO₂ experiments, and no experiments in the dacitic
1099 field. None of the other models contain any andesitic or dacitic melts in their calibration datasets.

6.1 Comparing solubility models to experimental products

The suitability of different solubility models for andesitic-dacitic compositions can be evaluated by calculating isobars using the melt compositions, pressures and temperatures of different experimental studies, and comparing these isobars to measurements of dissolved volatile contents in experimental products (similar to the method used in the supplementary material of Ghiorso & Gualda, 2015). The 2 and 5 kbar experiments of Botcharnikov et al. (2006) are shown in Fig. 16a-b, the 1, 2, and 5 kbar experiments of Behrens et al. (2004) are shown in Fig. 16c-e, and the 10 kbar experiments of King and Holloway (2002) are shown in Fig. 16f. Additional isobar diagrams for the 3-12 kbar experiments of Mangan et al. (2021) are shown in the supporting information.

Isobar diagrams show that S-2014 significantly underpredicts CO₂ for all experiments except the most H₂O-poor composition of King and Holloway (2002). L-2005, VolatileCalc-Basalt and -Rhyolite also mostly plot to lower CO₂ contents than experimental products. IM-2012 H and A do a reasonable job of recreating the most H₂O-poor experiments at <5 kbar, but curve rapidly down to intercept the x axis at lower H₂O contents than experimental products and other models. MagmaSat is a good match to experimental data in Fig. 16d, e and f, but plots to lower CO₂ contents than experiments in Fig. 16 a, b and c. Using Fe³⁺ proportions best representing the experimental conditions, P-2006 only passes through experimental data on Figs. 16a-b, and e, and plots to significantly lower CO₂ contents than experiments (lower than MagmaSat) on Fig. 16c and d. P-2006 also predicts anomalously high CO₂ contents for the 10 kbar experiments in Fig. 16f. P-2006 is a better match to most experiments if Fe³⁺/Fe_T=0, but still overpredicts CO₂ solubility at 10 kbar. Interestingly, none of the available models recreate the near-flat trajectory of dissolved CO₂ contents with increasing H₂O from Botcharnikov et al. (2006).

The underprediction of CO₂ solubility by S-2014 is a good example of the dangers of extrapolating models accounting for the effect of melt composition using empirical expressions beyond the compositional range of the calibration dataset. The S-2014 model expresses CO₂ solubility as a function of the composition parameter, Π^* , with CO₂ solubility increasing as an exponential function of Π^* at a given pressure (equation 16). The melt compositions for the three sets of experimental studies shown in Fig. 16 all plot to much lower Π^* values than any of the melts in the calibration dataset (orange diamonds; Fig. 17a). These low Π^* values mean that the S-2014 model predicts that these melts have very low CO₂ solubilities. However, CO₂ solubility for melts with Π^* values outside the range of the calibration dataset may not follow the same exponential function of this parameter as melt compositions within the calibration range. Additionally, the exponential dependency of CO₂ solubility on Π^* incorporated by S-2014 likely breaks down in more evolved melts, because Π^* represents the ability

1133 of the melt to form carbonate-bearing species, while more evolved melts contain increasing proportions
1134 of molecular CO₂ (Shishkina et al., 2014). For example, the proportion of molecular CO₂ to carbonate
1135 species varies between 0–4 wt% in the experiments of Botcharnikov et al. (2006), and 3–30 wt% in the
1136 dacitic experiments of Behrens et al. (2004), in both cases showing a rapid decrease in the proportion
1137 of molecular CO₂ with increasing melt H₂O content.

1138 VolatileCalc-Basalt and VolatileCalc-Rhyolite underpredict CO₂ solubility for all intermediate
1139 experiments, with VolatileCalc-Rhyolite predicting lower pure CO₂ solubility than VolatileCalc-Basalt.
1140 Yet, many publications have calculated saturation pressures for andesitic and dacitic melts using
1141 VolatileCalc-Rhyolite (e.g., Blundy et al., 2006; Atlas et al., 2006; Cassidy et al., 2015; Koleszar et al.,
1142 2012). In the original publication, Newman and Lowenstern (2002) state: “because many andesites
1143 contain rhyolitic interstitial melt, VolatileCalc may also be applicable to these intermediate composi-
1144 tions.” However, this should not be taken to suggest that VolatileCalc-Rhyolite is safely extrapolated
1145 to andesitic-dacitic melts. Instead, we suggest that this statement is referring to the fact that many
1146 lavas with andesitic bulk compositions have rhyolitic groundmass/melt inclusion compositions (e.g.,
1147 Tamura & Tatsumi, 2002; Reubi & Blundy, 2009), where VolatileCalc-Rhyolite may be applicable.
1148 Interestingly, VolatileCalc-Rhyolite isobars calculated for the reference temperature of this model
1149 (850°C) are a good match to experimental data at < 5 kbar (see Supplementary Fig. S2). Thus, the
1150 main failure of this model in intermediate compositions appears to result from the fact that this model
1151 is extremely sensitive to temperature, and these melts have much higher temperatures than the experi-
1152 ments used to calculate this model. This supports our suggestion in section 4.2.1 that it may be better
1153 run models at their reference temperature, rather than extrapolate beyond the calibration range.

1154 It is also worth noting that all these experimental products have negative values of the Dixon II
1155 parameter (equation 2). As highlighted by G. Moore (2008), the full II expression of Dixon (1997) can-
1156 not be used to calculate CO₂ solubility in calc-alkaline lavas, because II is negative (yielding a negative
1157 solubility of CO₂; Fig. 17).

1158 Differences between experimental data and isobars from IM-2012-H and -A are more compli-
1159 cated, because the discrepancies between models and experiments are very dependent on the pressure.
1160 For example, at 1 kbar, IM-2012-H and -A underpredict H₂O and CO₂ solubility relative to the ex-
1161 periments of Behrens et al. (2004), while at 5 kbar, they overpredict CO₂ solubility, but underpredict
1162 H₂O solubility (Fig. 16c vs.e). These discrepancies likely reflect this model being extrapolated towards
1163 the limits of its calibration dataset in terms of both pressure (most experiments were conducted at <5
1164 kbar) and melt composition (Fig. 17, see the next section for more discussion).

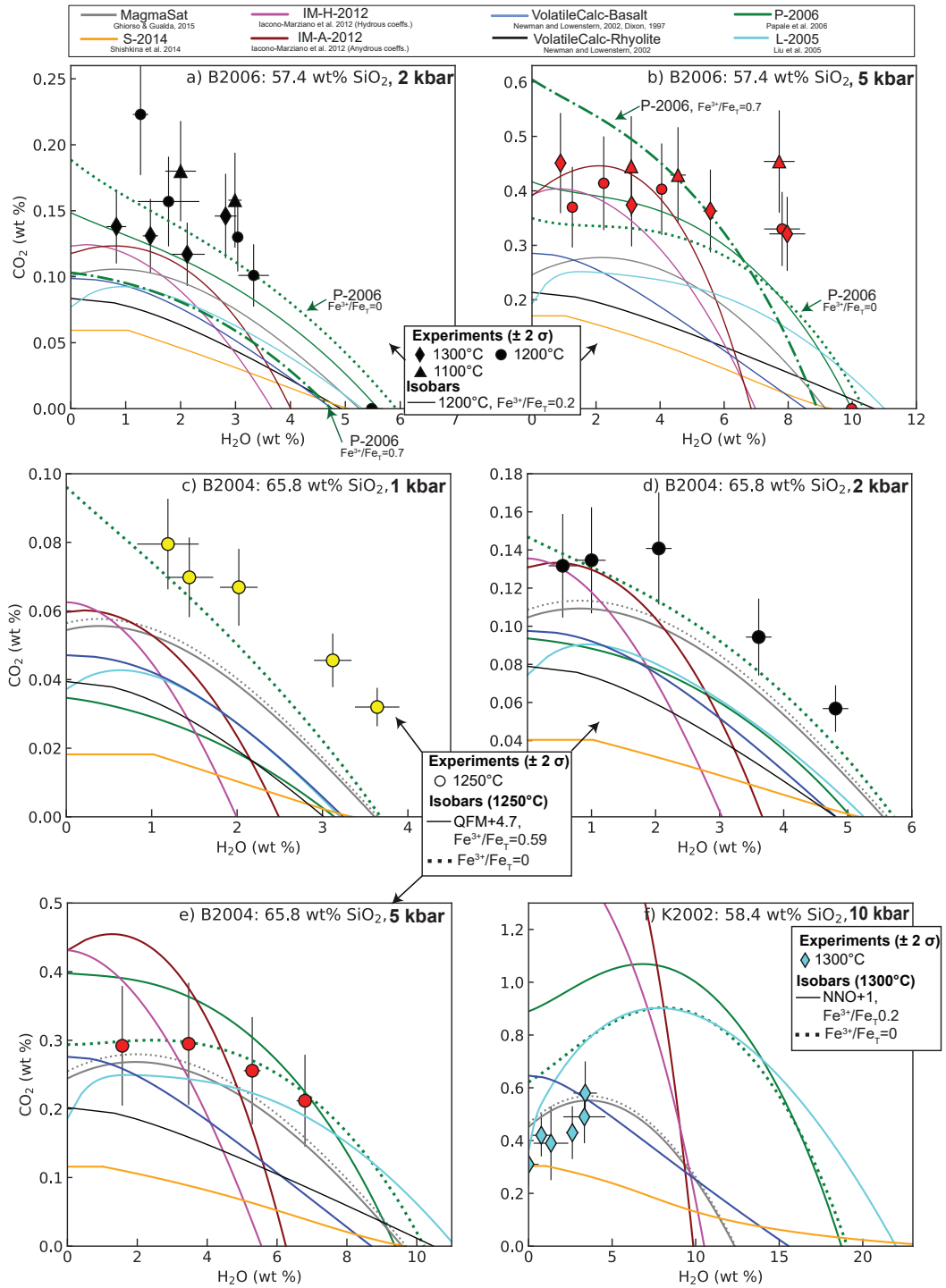


Figure 16. Assessing model fits to experimental data for andesitic and dacitic compositions a-b) Experiments from Botcharnikov et al. (2006). Isobars were calculated for 1200 and Fe³⁺/Fe_T=0.2 (~QFM+1.5). P-2006 isobars are also shown for Fe³⁺/Fe_T=0.7 (the upper estimate of Fe³⁺/Fe_T in experimental products; dash-dotted line), and Fe³⁺/Fe_T=0 (dotted line) c-e) Experiments from Behrens et al. (2004). Isobars are shown for Fe³⁺/Fe_T=0.59 (*f*O₂ of QFM+4.7). For P-2006 and MagmaSat, isobars are also shown for Fe³⁺/Fe_T=0. f) Experiments from King and Holloway (2002). Isobars are shown for Fe³⁺/Fe_T=0.2. For P-2006 and MagmaSat, isobars are also shown for Fe³⁺/Fe_T=0. VolatileCalc-Rhyolite isobars are not shown as the spreadsheet won't calculate isobars above 5 kbar. Error bars on all plots shows the 2σ uncertainties from measurements of volatile contents in experimental products. Fe³⁺/Fe_T ratios were calculated from author-stated buffers using MELTS for excel (Gualda & Ghiorso, 2015).

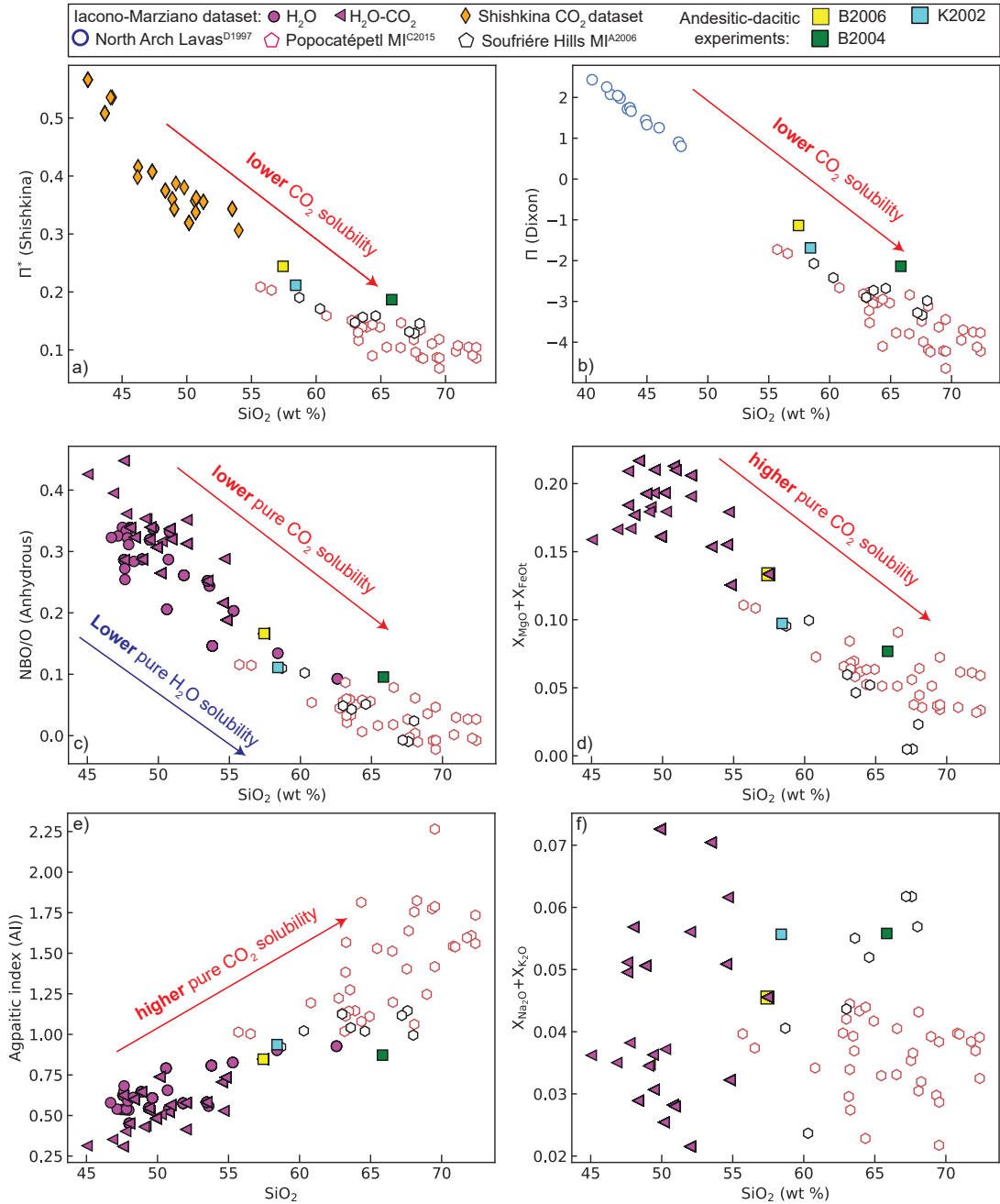


Figure 17. Comparing the calibration datasets of S-2014 and IM-2012 to the andesitic experiments of Botcharnikov et al. (2006): B2006, Behrens et al. (2004): 2004 and King and Holloway (2002): K2002 shown in Fig. 16, and the melt inclusions from Popocatepetl (Atlas et al., 2006) and Soufrière Hills (Cassidy et al., 2015) shown in Fig. 18. a) Π^* for experimental products and both sets of melt inclusions plot to significantly lower values than the calibration dataset of S-2014. b) Experimental products and melt inclusions have negative Π values, showing the issues associated with applying the full Π parameterization of Dixon (1997) to calc-alkaline arc lavas. c) NBO/O (calculated on an anhydrous basis) vs. SiO_2 shows that melt inclusions plot to significantly lower values than the calibration dataset of IM-2012. d) Anhydrous molar fractions of FeO and MgO vs. SiO_2 . Experiments and melt inclusions have far lower molar fractions of MgO and FeO than the calibration dataset of IM-2012. Anhydrous cation fractions are shown because when accounting for discrepancies between isobars, the H_2O content and therefore hydrous cation fraction varies as a function of the pressure.

1165 The fact that no model passes through all available experiments demonstrates that further in-
 1166 vestigation of solubility in andesitic to dacitic melts is warranted. Using representative experimental
 1167 $\text{Fe}^{3+}/\text{Fe}_T$ ratios, MagmaSat is the most accurate model, predicting dissolved volatile contents within
 1168 $\sim 20\%$ of experimental products (considering reported error bars on dissolved volatile contents).

1169 The extreme sensitivity to the $\text{Fe}^{3+}/\text{Fe}_T$ ratio makes it very difficult to assess the accuracy of
 1170 the P-2006 model (particularly given the relatively large uncertainties in the oxygen fugacity of ex-
 1171 perimental run products; King & Holloway, 2002; Botcharnikov et al., 2006). In all of the examples
 1172 shown, P-2006 isobars calculated for $\text{Fe}^{3+}/\text{Fe}_T=0$ are a better fit to the experimental data than iso-
 1173 bars calculated using estimates of the $\text{Fe}^{3+}/\text{Fe}_T$ ratio of experiments. This suggests that, in relatively
 1174 oxidising intermediate melts, P-2006 is overestimating the effect of Fe^{3+} species on volatile solubility.
 1175 It is noteworthy that P-2006 is a particularly poor match to the high pressure andesitic experiments
 1176 of King and Holloway (2002), despite the fact that these are the only intermediate experiments in the
 1177 calibration dataset of this model.

1178 As all the experiments shown were used to calibrate MagmaSat, similar analysis applied to new
 1179 experimental data on andesitic compositions when it becomes available will provide further constraints
 1180 on the accuracy of this model. Isobars for recent solubility experiments on a basaltic-andesite arc
 1181 magma at 400-1200 MPa by Mangan et al. (2021) are shown in the Supplementary Fig. S3 and S4.
 1182 MagmaSat is a much better fit to this new data than P-2006, with experiments performed 400-815
 1183 MPa plotting within error of calculated MagmaSat isobars. In contrast, P-2006 overpredicts CO_2
 1184 solubility (regardless of $\text{Fe}^{3+}/\text{Fe}_T$) at <600 MPa.

1185 6.2 Case Study: Intermediate melt inclusions

1186 To assess the impact of these model differences on the depths of magma storage reservoirs in-
 1187 ferred from melt inclusions in volcanic arcs, we calculate saturation pressures using a variety of models
 1188 for two suites of melt inclusions with andesitic-dacitic liquid compositions: 1) 34 melt inclusions from
 1189 Volcán Popocatepetl, Mexico with 55.7–73.4 wt% SiO_2 (Figs. 2, 18a; Atlas et al., 2006), and 2) 8 melt
 1190 inclusions from Soufrière Hills Volcano, Montserrat with 58.7–68.0 wt% SiO_2 (Figs. 2, 18b; Cassidy
 1191 et al., 2015). Both studies calculated saturation pressures (and therefore magma storage depths) using
 1192 VolatileCalc-Rhyolite.

1193 Cumulative frequency distributions for the Popocatepetl melt inclusions (Fig. 18a) shows that
 1194 P-2006 predicts the lowest saturation pressures, and S-2014 the highest, with MagmaSat, IM-2012-A,
 1195 VolatileCalc-Basalt, VolatileCalc-Rhyolite, and IM-2012-H lying in-between these model extremes.
 1196 Based on our analysis in the previous section suggesting that MagmaSat is the best calibrated model
 1197 for intermediate melt compositions, we ratio saturation pressures from each model to those determined

1198 using MagmaSat (allowing model differences to be quantified). Additionally, because MagmaSat is a
1199 thermodynamic model that has been shown to work well for basaltic and rhyolitic compositions, it is
1200 effectively being interpolated to andesitic-dacitic compositions which are not represented in its calibra-
1201 tion dataset (i.e., these melt inclusion compositions), rather than extrapolated (as for empirical models
1202 such as S-2014, VolatileCalc-Basalt, and IM-2012 which are primarily calibrated on more mafic melt
1203 compositions; Fig. 2).

1204 The median saturation pressure for Popocatepetl melt inclusions calculated for VolatileCalc-
1205 Rhyolite is $1.26\times$ higher than for MagmaSat. The median for MagmaSat is $\sim 1.2\times$ higher than for P-
1206 2006. The deviation relative to MagmaSat increases with SiO_2 content for VolatileCalc-Rhyolite (~ 1.1
1207 to $1.5\times$), VolatileCalc-Basalt (~ 1 to $1.35\times$), and L-2005 (~ 1 to $1.4\times$; Fig. S2). The deviation between
1208 S-2014 and MagmaSat is very large, increasing from a factor of 2 at ~ 55 wt% SiO_2 to $\sim 5.5\times$ at 72.5
1209 wt% SiO_2 . The deviation between IM-2012-H and -A and P-2006 vs. MagmaSat shows no clear cor-
1210 relation with SiO_2 content (Supporting Fig. S5). The presence of discrepancies which correlate with
1211 melt composition is particularly concerning, because it means that choice of an inappropriate solubility
1212 model may introduce systematic error into a dataset as a function of melt inclusion composition.

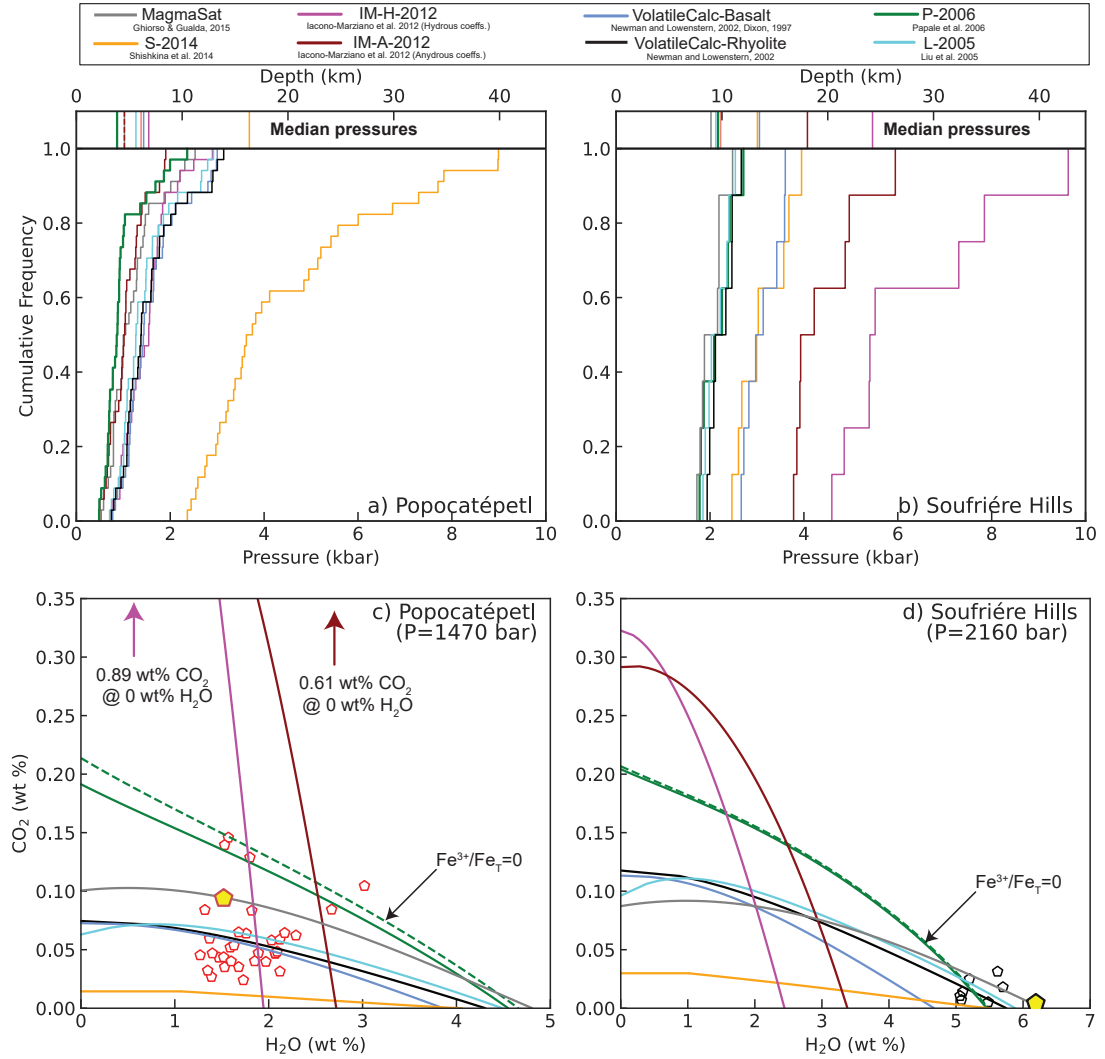


Figure 18. a-b) Cumulative distribution functions of saturation pressures from different models for melt inclusions from a) Popocatepetl (Atlas et al., 2006) and b) Soufrière Hills (Cassidy et al., 2015). Fe^{3+}/Fe_T was set to 0.15. c) Isobars from different models calculated at the saturation pressure from MagmaSat (1470 bar) for the Popocatepetl melt inclusion shown with a yellow pentagon (at 1050°C following Atlas et al., 2006). The scale is trimmed to emphasize the differences between models at lower CO₂ contents, with the interception of the IM-2012 isobars with the y axis labelled on the plot. d) Isobars from different models calculated at the saturation pressure from MagmaSat (2160 bar) for the Soufrière Hills melt inclusion shown with a yellow pentagon (at 1000°C following Cassidy et al., 2015). Isobars are also shown for P-2006 with $Fe^{3+}/Fe_T=0$ (dotted line)

1213

MagmaSat predicts the lowest saturation pressures for the Soufrière Hills melt inclusions, with

1214

L-2005, P-2006, and VolatileCalc-Rhyolite predicting reasonably similar pressures. VolatileCalc-Basalt,

1215 S-2014 and IM-2012-A and -H are offset to higher pressures. Similar to the results for Popocatepetl,
 1216 the ratio of saturation pressures for Soufrière Hills melt inclusions relative to MagmaSat for L-2005
 1217 (~ 1 to $1.1\times$), VolatileCalc-Basalt (~ 1.25 to $1.35\times$) and VolatileCalc-Rhyolite (~ 1.05 to $1.17\times$) in-
 1218 crease with increasing SiO_2 (Supporting Fig. S6). Unlike Popocatepetl melt inclusions, the discrep-
 1219 ancy between IM-2012 and MagmaSat increases dramatically with increasing SiO_2 (from ~ 1.5 to $2.5\times$
 1220 for anhydrous, and 2 to $4.5\times$ for hydrous), while that for S-2014 shows a weak negative correlation
 1221 with SiO_2 (from ~ 1.7 – $1.35\times$).

1222 The large discrepancies shown by IM-2012 (for Soufrière Hills) and S-2014 (for Popocatepetl) are
 1223 best understood by examining an isobar calculated for the inclusion showing the largest deviation rela-
 1224 tive to MagmaSat in each dataset ($\text{SiO}_2=72.4$ wt% for Popocatepetl, and 67.6 wt% for Soufrière Hills;
 1225 yellow pentagon on Fig. 18c-d) at the saturation pressure obtained from MagmaSat. For both sets of
 1226 inclusions, S-2014 isobars intercept the x axis at similar H_2O contents to other models, but intercept
 1227 the y axis at drastically lower CO_2 contents. This underestimation of CO_2 solubility likely results
 1228 from the fact that the Π^* values of these inclusions lie well below that of the calibration dataset (as
 1229 discussed for andesitic experiments; Fig. 17b).

1230 In contrast, IM-2012 predicts very high pure CO_2 solubility, and low pure H_2O solubility relative
 1231 to the other models. Both IM-2012 models express the compositional dependence of H_2O solubil-
 1232 ity in terms of the parameter NBO/O, with melts with higher NBO/O values having higher H_2O
 1233 solubility (equation 15). Both sets of melt inclusions possess much lower NBO/O values than the
 1234 calibration dataset of IM-2012 (Fig. 17c-d). This is problematic, because the empirical relationship
 1235 between NBO/O and pure H_2O solubility incorporated by IM-2012 has not been validated for these
 1236 melt compositions. For example, Shishkina et al. (2014) show that IM-2012 drastically overestimates
 1237 H_2O solubility in their basanite and nephelinite melt compositions. They point out that while IM-2012
 1238 conclude that there is only a small effect of melt composition on H_2O composition, the IM-2012 model
 1239 ends up showing a strong sensitivity to melt composition when extrapolated to the high NBO/O ratio
 1240 in their basanite and nephelinite melts (and we invoke a similar explanation for the lower NBO/O
 1241 ratios in melt inclusions discussed here).

1242 The IM-2012 expression for CO_2 solubility is more complicated, containing terms for the Ag-
 1243 paitic index (AI), NBO/O, $X_{\text{Na}_2\text{O}+\text{K}_2\text{O}}$, $X_{\text{FeO}+\text{MgO}}$ and $X_{\text{H}_2\text{O}}$ (equation 11). These two sets of melt
 1244 inclusions have higher AI, lower NBO/O ratios, similar values of $X_{\text{Na}_2\text{O}+\text{K}_2\text{O}}$, and lower $X_{\text{FeO}+\text{MgO}}$
 1245 values than the calibration dataset (Fig. 17d-f). While the effect of NBO/O is more convoluted be-
 1246 cause it also affects the solubility of H_2O (which feeds back into the expression for CO_2), it is readily
 1247 apparent that the positive coefficient attached to the AI term combined with the negative coefficient

1248 attached to the MgO+FeO term causes this model to predict higher CO₂ solubilities than the calibra-
 1249 tion dataset for the andesitic-dacitic melt inclusions considered here.

1250 The discrepancy between isobars for S-2014 and IM-2012 relative to MagmaSat are relatively
 1251 similar for the Popocatépetl and Soufrière Hills melt compositions, while discrepancies for saturation
 1252 pressures differ markedly (Fig. 18a-b vs. c-d). This is because the volatile contents of Popocatépetl
 1253 melt inclusions are significantly more CO₂-rich (~0.02-0.15 wt% and higher), and H₂O-poor (~1-3
 1254 wt%) than Soufrière Hills melt inclusions (<0.04 wt% CO₂ and 5-6 wt% H₂O). For this reason, cal-
 1255 culated saturation pressures for Popocatépetl melt inclusions are sensitive to the treatment of both
 1256 CO₂ and H₂O in solubility models (Fig. 18b), while those for Soufrière Hills melt inclusions are mostly
 1257 sensitive to pure H₂O solubility. Thus, S-2014 overestimates saturation pressures for Popocatépetl
 1258 melt inclusions because this model drastically underestimates the solubility of pure CO₂. In contrast,
 1259 S-2014 only slightly underestimates H₂O solubility relative to MagmaSat, so only slightly overpredicts
 1260 saturation pressures for H₂O-rich Soufrière Hills melt inclusions. The discrepancy between IM-2012
 1261 and MagmaSat is much smaller for Popocatépetl relative to Soufrière Hills because, fortuitously, the
 1262 IM-2012-H isobar intercepts the MagmaSat isobar at H₂O contents similar to these Popocatépetl melt
 1263 inclusions. IM-2012-H and -A drastically underestimates the solubility of pure H₂O, so overestimates
 1264 saturation pressures for the H₂O-rich Soufrière Hills melt inclusions relative to other models.

1265 It is worth noting that Iacono-Marziano never intended their model to be applied to andesites,
 1266 and when discussing the limitations of their model, they explicitly warn that their empirical expres-
 1267 sions poorly incorporates the effect of MgO and FeO on CO₂ solubility because of the restricted range
 1268 of these oxides in the calibration dataset. We have included this discussion as an extreme example of
 1269 the danger of extrapolating empirical models beyond their calibration range. However, the sensitiv-
 1270 ity of this model to the FeO and MgO content of the melt also presents issues when applied to high
 1271 MgO basaltic liquids. For example, Wieser et al. (2020) show that IM-2012 predicts higher saturation
 1272 pressures for highly primitive (high MgO) melt inclusions from Kīlauea Volcano relative to S-2014 and
 1273 MagmaSat. This likely reflects the higher values of X_{FeO+MgO} in these melt inclusions relative to the
 1274 calibration dataset, which causes IM-2012 to predict lower CO₂ solubility (the opposite directionality
 1275 to that seen for the intermediate melt inclusions discussed here).

1276 The H₂O-rich nature of Soufrière Hills melt inclusions means that VolatileCalc-Rhyolite pre-
 1277 dicts much more similar saturation pressures to MagmaSat (1.07-1.15×; Supporting Figure S6) than
 1278 for Popocatépetl (1.1-1.5× higher; Supporting Figure S5), because the main failure of VolatileCalc-
 1279 Rhyolite for intermediate compositions at moderate to high temperatures (>850 °C) is its prediction
 1280 of pure CO₂ solubility (Figs. 16, 18c-d). The discrepancy for both VolatileCalc models and L-2005

1281 relative to MagmaSat is significantly smaller than for S-2014 and IM-2012. This is because the solu-
 1282 bility differences during evolution for basaltic to rhyolitic compositions are relatively small (30–40%)
 1283 compared to the error associated with the extrapolating an empirical model far beyond its composi-
 1284 tional range. Overall, this case study shows the importance of checking that the calibration dataset of
 1285 a model contains melts similar to those in the sample set of interest, particularly if the effect of melt
 1286 composition is parameterized empirically.

1287 7 Best practices for data visualization and curation

1288 7.1 Isobar Diagrams: limitations and alternatives

1289 As demonstrated by the preceding section, isobar diagrams are a useful tool to visualize vari-
 1290 ations in volatile solubility for a specific melt composition. However, many suites of melt inclusions
 1291 have considerable major element variability (Wieser et al., 2020; Roggensack, 2001; Iacovino et al.,
 1292 2021), which translates into differing solubilities of H₂O-CO₂ at a given pressure, and different isobar
 1293 shapes at a given pressure. To demonstrate this, we use a suite of basaltic melt inclusions from Kone
 1294 and Butajira volcanoes in the Main Ethiopian Rift (Iddon & Edmonds, 2020). Following Iddon and
 1295 Edmonds (2020), we calculate isobars for a representative inclusion composition (BJ08_7; Fig. 19a),
 1296 and compare these to the isobars calculated for each individual melt inclusion composition at 1 and
 1297 3 kbar (Fig. 19b-c). 3 kbar isobars calculated from the composition of each individual melt inclusion
 1298 from Butajira (Fig. 19b) cover the entire region of H₂O-CO₂ space that is bracketed by the 2 and 4
 1299 kbar isobars calculated in MagmaSat for the representative melt inclusion composition (Fig. 19b vs.
 1300 a). The same is true for isobars calculated for Kone melt inclusion compositions. Thus, for a given
 1301 CO₂ and H₂O content, the major element composition of the melt inclusion in question can affect
 1302 the saturation pressure by almost a factor of 2 (and, by extension, visual inspection of melt inclusion
 1303 volatile concentrations plotted on isobar diagrams may be associated with an error of this magnitude).

1304 Isobar plots can also be misleading when evaluating differences in saturation pressures within
 1305 a given suite of melt inclusions. For example, Fig. 19d plots the 3 kbar isobars for 4 Kone melt in-
 1306 clusions which show considerable major element variability (SiO₂=47.1–49.5 wt%, MgO=5.89–7.97
 1307 wt%, FeO_t=7.25–11.84 wt%, Na₂O=2.8–3.7 wt%, K₂O=0.65–1.3 wt%). If a single isobar was drawn on
 1308 this plot, it would appear that the yellow, green, blue and magenta melt inclusions were trapped from
 1309 higher to lower pressures. However, the MagmaSat saturation pressure for the yellow melt inclusion
 1310 shows that it was trapped >1 kbar shallower than the green melt inclusion, despite having a higher
 1311 CO₂ content. This is because the composition of the green melt inclusion corresponds to a lower sol-
 1312 ubility of CO₂ at a given pressure relative to the yellow inclusion (shown by the position of their 3

1313 kbar isobars). Similarly, an isobar diagram would suggest that the blue melt inclusion was trapped at
 1314 a higher pressure than the magenta melt inclusion, when the opposite is true.

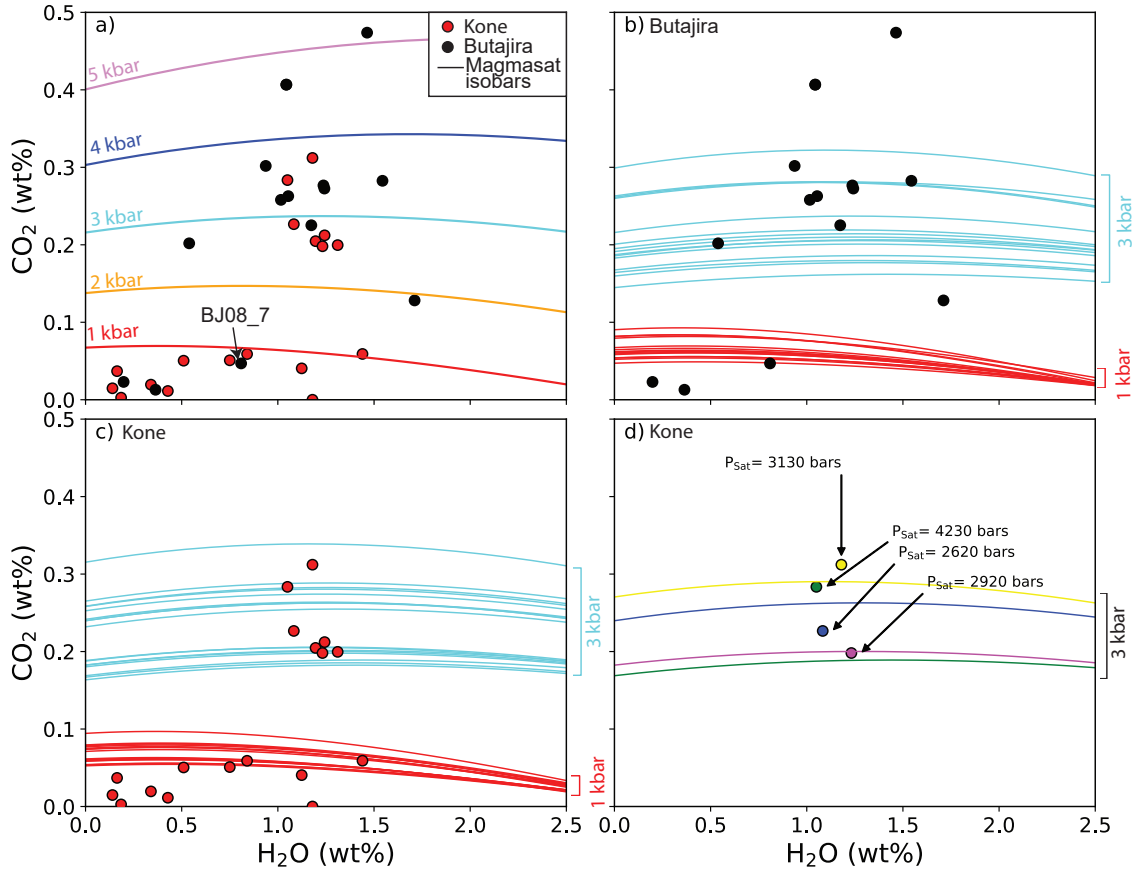


Figure 19. Isobars for olivine-hosted melt inclusions from Iddon and Edmonds (2020) calculated at 1170°C. a) MagmaSat isobars for melt inclusion BJ08.7 from Butajira with melt inclusion volatile data overlain. b) 1 and 3 kbar isobars calculated for the major element composition of each individual melt inclusion from Butajira. c) Same as b) but for melt inclusions from Kone. d) Volatile data for four melt inclusions from Kone and the corresponding 3 kbar isobars (color coded). Despite having the highest CO₂ content, the yellow melt inclusion yields a lower saturation pressure than the green inclusion (3130 vs. 4230 bars), and the blue inclusion was trapped at a lower saturation pressure than the magenta inclusion (2620 vs. 2920 bars). The 3 kbar isobars for these two inclusions plot a long way apart, showing the importance of evaluating solubility using the major element composition of each individual inclusion.

1315 VESICAL solves the problem of potentially misleading isobar diagrams by facilitating rapid calcu-
 1316 lations of saturation pressures for large suites of melt inclusions. For example, calculating saturation

1317 pressures for the 33 melt inclusions in the dataset of Iddon and Edmonds (2020) using VolatileCalc-
1318 Basalt, S-2014, and IM-2012 takes only 4.2 seconds if VESIcal is run on the ENKI server. MagmaSat
1319 is slightly slower, taking 31.5 seconds (still <1 s per sample). MagmaSat calculations may run faster
1320 if thermoengine is installed locally (calculations take 26.3 s using a Dell Inspiron laptop with 16 GB
1321 RAM and an Intel-i7 processor, see <https://gitlab.com/ENKI-portal/ThermoEngine> for installation
1322 help).

1323 Once users have calculated saturation pressures for each inclusion, a number of different x-y plots
1324 will provide more information than isobar diagrams. For example, G. Moore (2008) suggests that users
1325 could plot two graphs, one showing melt inclusion CO_2 content against saturation pressure and one
1326 showing melt inclusion H_2O contents against saturation pressure. This allows clustering of saturation
1327 pressures to be observed, and determination of the importance of each volatile species when calculat-
1328 ing saturation pressure. Alternatively, saturation pressures could be plotted as histograms, cumulative
1329 density functions, or box/violin plots to assess clustering, and to compare distributions from different
1330 crystal populations, eruptions, or different volcanic centres. It may also be advantageous to compare
1331 saturation pressures to host-crystal chemistry. For example, Wieser et al. (2020) show that melt in-
1332 clusions hosted in low forsterite olivine crystals from Kilauea Volcano crystallized at ~ 1 -2 km depth,
1333 while melt inclusions hosted within higher forsterite olivines crystallized at ~ 3 -5 km depth.

1334 7.2 Assessing Errors

1335 The ability to calculate saturation pressures using a number of different models in VESIcal is
1336 advantageous, because it can provide assessment of the systematic errors associated with model choice.
1337 If different solubility models produce saturation pressures which are statistically distinguishable using
1338 tests such as ANOVA or the Kolmogorov-Smirnov test, or differences between models exceed 10-20%
1339 (the approximate quoted error on most models), users need to evaluate their melt compositions, pres-
1340 sures and temperatures in the context of the calibration dataset of each solubility model. Several
1341 Jupyter notebooks aiding these comparisons are provided alongside VESIcal part I (Iacovino et al.,
1342 2021). In general, if a natural silicate melt composition is poorly represented by experimental data,
1343 MagmaSat is probably the best model to use, as its thermodynamic nature is more suitable to extrap-
1344 olation to melt compositions not represented in the calibration dataset than empirical models such
1345 as IM-2012, S-2014, or VolatileCalc-Basalt. However, the comprehensive nature of MagmaSat means
1346 that the fit to experimental data from any specific region of major element space is compromised by
1347 the fact the model is optimizing the overall fit to many different major element compositions. Thus,
1348 where present, models developed for specific volcanic centres, or highly weighted towards specific melt
1349 compositions (e.g. A-2019 for the 6 centers they investigate, or IM-2012 for alkaline compositions) may

1350 return a better fit. While these composition-specific models may be well calibrated in terms of melt
1351 composition, users must also check that they are applying the model within the recommended pressure
1352 and temperature range. We suggest that comparisons between any available experimental data for
1353 relevant melt compositions and different solubility models using a workflow similar to that used here
1354 for andesites (e.g., isobar diagrams as in Fig. 16, plots of melt composition vs. calibration datasets)
1355 will help users select a suitable model. As well as examining melt compositions, users should also eval-
1356 uate whether they are extrapolating temperature-sensitive models beyond the calibration range (as
1357 discussed here for VolatileCalc-Rhyolite).

1358 VESICAL can also be used to explore the effects of uncertainty in input parameters (as in the sen-
1359 sitivity tests presented here). Error bars for calculated saturation pressures are asymmetrical, even for
1360 input parameters with symmetric error distributions. Thus, to calculate an error bar on each inclusion,
1361 three saturation pressure calculations must be performed. Using the older generation of tools, this
1362 would be exceptionally time consuming. Using VESICAL, calculations can be performed automatically,
1363 and users could simply input three spreadsheets, or a spreadsheet with three columns for the uncer-
1364 tain parameter (containing the preferred, maximum and minimum value) to calculate error bars (e.g.,
1365 uncertainties in total CO₂ contents resulting from 2D measurements of bubble volumes and analytical
1366 uncertainties in diad splittings; Wieser et al., 2020).

1367 VESICAL also opens up the capability to handle errors arising from volatile solubility modelling
1368 using the advanced functionality of Python3 packages such as Numpy, SciPy and PyMC to perform
1369 Bayesian statistical techniques (e.g., Markov Chain Monte Carlo methods). This would allow the un-
1370 certainty in all input parameters (e.g., temperature, analytical uncertainties in volatile and major
1371 element contents, uncertainty arising from post-entrapment crystallization corrections) into a resulting
1372 error distribution for each melt inclusion. These techniques are increasingly being utilized by igneous
1373 petrologists, with recent applications including calculating error distributions for diffusion timescales
1374 (Mutch et al., 2019), the contribution of melts from distinct mantle sources (Gleeson et al., 2020), and
1375 propagating uncertainties in vapour bubble growth models (Rasmussen et al., 2020).

1376 7.3 Data Curation

1377 Now that VESICAL makes it possible to calculate saturation pressures for large melt inclusion
1378 datasets in short amounts of time, it is vital that data is published in a way that allows such calcu-
1379 lations to be performed retrospectively so that, for example, literature compilations of melt inclusion
1380 saturation pressure depths can be consistent regarding model choice. The concentration of major
1381 elements and volatile elements should be provided within a single spreadsheet or database, ideally
1382 alongside the composition of the mineral host. Additionally, if melt inclusions are corrected for post-

1383 entrapment crystallization (PEC), both raw and corrected major and volatile element concentrations
1384 should be published. Particularly for more chemically-complex host minerals like pyroxene and plagioclase,
1385 it is highly likely that community standards on the best PEC procedure will change with time.
1386 Even for olivine-hosted melt inclusions, there a variety of correction techniques used in the literature,
1387 which can predict very variable amounts of PEC (Wieser et al., 2020, show that the PEC routine in
1388 Petrolog3 predicts 30% more PEC than corrections based on Mg# disequilibrium between the host
1389 and melt inclusion). Finally, given that numerous recent studies have shown that bubble CO₂ contents
1390 can change calculated saturation pressures by up to an order of magnitude (section 5), authors should
1391 also make note of whether each melt inclusion contained a vapour bubble (and ideally an estimate of
1392 the volume proportion of the bubble). This information may allow the CO₂ contents in vapour bubbles
1393 to be reconstructed theoretically by future studies, given the recent proliferation of vapour bubble
1394 growth models (e.g. Aster et al., 2016; Rasmussen et al., 2020; MacLennan, 2017).

1395 Proper data curation is particularly vital in the world of volatile solubility modelling because it
1396 is very likely that many more experiments will be published over the next decade, allowing the creation
1397 of new solubility models that are calibrated over an even wider region of P-T and compositional
1398 space. Many publications could not be used for comparisons in this study, because there was simply no
1399 way to combine volatile element concentrations and major element concentrations (which were often
1400 reported in different tables with non-unique or non-matching sample names), or not reported at all. It
1401 would be a great shame if published melt inclusion datasets could not be input into these new models
1402 to recalculate saturation pressures, and gain a greater understanding of magma storage in the Earth's
1403 crust.

1404 **8 Future work**

1405 The comparisons drawn in this review highlight several research areas where further experimental
1406 work is required to be able to distinguish which model behaviors are accurate. First, significantly
1407 more experiments are needed on andesitic-dacitic melt compositions. Figure 16 shows that it is currently
1408 impossible to differentiate a failure in any given solubility model from anomalies in any given
1409 set of experiments (e.g., the differential effect of addition of H₂O on CO₂ solubility in different experiments;
1410 Fig. 16b. vs f). One of the challenges when assessing CO₂ solubility in andesitic-dacitic melts
1411 is the fact that CO₂ is present as both carbonate and molecular CO₂, which are difficult to deconvolve
1412 analytically. In particular, the accuracy of FTIR is affected by peak overlap, and uncertainty in
1413 peak backgrounds and absorption coefficients (Botcharnikov et al., 2006; Mangan et al., 2021). SIMS
1414 measurements of experiment products, aided by an increased understanding of the optimal analysis
1415 conditions for volatiles in silicate glasses of the last few decades, may help to resolve these issues, as

1416 SIMS measures total CO₂. However, in addition to its substantial cost relative to FTIR, accurate
1417 SIMS measurements are reliant on having a suite of standards with similar major element composi-
1418 tions and a range of volatile contents (and these standards are often characterized by FTIR, so are
1419 subject to the caveats mentioned above).

1420 Second, the effect of redox on volatile solubility across the range encountered in terrestrial mag-
1421 mas is still poorly constrained (section 5). This discrepancy largely reflects the fact that the redox
1422 conditions at which many experiments in the literature were conducted are uncertain and/or highly
1423 variable (e.g., Botcharnikov et al., 2006). Because of this uncertainty, many calibration datasets are
1424 built without being able to constrain the quantities of Fe₂O₃ and FeO for each experimental run.
1425 While our investigation of intermediate melts indicates that the strong sensitivity of CO₂ solubility to
1426 melt redox shown by P-2006 is likely anomalous because of the presence of experiments with extremely
1427 high calculated Fe³⁺/Fe_T ratios in the calibration dataset, further experiments where Fe₂O₃ and FeO
1428 proportions are accurately measured are needed to be certain that this behaviour is not real. It is also
1429 noteworthy that almost all the andesitic experiments were performed at higher oxygen fugacities than
1430 lavas erupted at volcanic arcs. When the calibration dataset for a given set of compositions is so small,
1431 this makes it difficult to deconvolve changes in volatile solubility with melt composition compared
1432 to redox. Recent advances in measurements of Fe³⁺/Fe_T using Fe K-edge micro-X-ray absorption
1433 near-edge structure (XANES) spectroscopy in hydrous glasses (Cottrell et al., 2018) could provide an
1434 avenue to better constrain this parameter in future (and past) experimental products.

1435 It is also worth noting that all the models discussed here only consider the effect of redox
1436 through terms for Fe²⁺ and Fe³⁺ in the melt, constraining their applicability to melts more oxidising
1437 than the IW buffer. In more reducing conditions, the co-existing CO₂-rich phase may be graphite or
1438 diamond rather than a CO₂-rich vapour phase (Eguchi & Dasgupta, 2018), and the dissolved volatile
1439 species may be CO, CH₄ and H₂ (Mysen et al., 2009). This means that extreme caution is required
1440 when applying these solubility models to highly reducing conditions such as those found on other
1441 planetary bodies (e.g., the Moon, Mars and Mercury; Li et al., 2017).

1442 Third, there is still significant uncertainty regarding the exact nature of H₂O and CO₂ mixing
1443 at higher pressure. This reflects the difficulty in measuring mixed H₂O-CO₂ fluids that were in equi-
1444 librium with the melt during the experiment. If measured at all, methods in the literature span from
1445 puncture and weight loss of frozen capsules (i.e., when frozen the CO₂ is released, but not the H₂O;
1446 Shishkina et al., 2010) to more sophisticated and accurate vacuum line manometry (G. Moore et al.,
1447 2008; Iacovino et al., 2013; Allison et al., 2019). New infinite path laser spectrometry technology may
1448 offer potential improvement of this critical measurement, but challenges associated with small sample

1449 sizes remain. More work determining the pure CO₂ solubility as a function of pressure and tempera-
1450 ture would also be of great benefit in constraining the behavior of H₂O-poor fluids.

1451 Fourth, we show that the sensitivity of dissolved volatile contents to temperature is highly
1452 model-specific. Given the difficulties with constraining temperature sensitivity experimentally (Iacono-
1453 Marziano et al., 2012), we suggest that it may be best to parametrize future empirical model at a
1454 single temperature (e.g., A-2019, S-2014), or incorporate the temperature sensitivity predicted by ther-
1455 modynamical models, rather than introduce a spurious temperature dependency which is not founded
1456 in experimental data, nor consistent with the relative entropy of melt and fluid terms.

1457 Finally, it is worth noting that all of the solubility models discussed only consider H₂O-CO₂ in
1458 the vapour phase, while in reality, natural fluids in volcanic systems may contain relatively large pro-
1459 portions of F, Cl, and S, as well as a separate brine phase (Botcharnikov et al., 2007). Additionally,
1460 at higher pressures and temperatures, significant quantities of major element species) will dissolve into
1461 a H₂O-rich fluid (e.g., Si, Na, K), with silicate melt and hydrous fluids becoming completely miscible
1462 above a critical temperature (Bureau & Keppler, 1999). This causes a pure H₂O model to underesti-
1463 mate the true solubility of H₂O at these conditions. Combined with the fact that it is near-impossible
1464 to quench silicate melts with $>9\pm 1$ wt% H₂O to a glass phase which can be analysed by SIMS or
1465 FTIR (Gavrilenko et al., 2019; Mitchell et al., 2017), quantifying the solubility of H₂O at condition
1466 relevant to lower crustal magma storage will require experimental innovations (e.g. Makhluף et al.,
1467 2020; Mitchell et al., 2017), in addition to developing models capable of calculating equilibria between
1468 a silicic melt phase and a complex aqueous fluid (Ghiorso & Sverjensky, 2016; Sverjensky et al., 2014;
1469 Huang & Sverjensky, 2019).

1470 9 Conclusion

1471 This review uses the new open-source Python3 tool VESIcal (Iacovino et al., 2021), in addition
1472 to VolatileCalc (Newman & Lowenstern, 2002) and Solwcad (Papale et al., 2006) to draw extensive
1473 comparisons between the behaviour of 9 different solubility models for a range of melt compositions.
1474 We show that these models predict surprisingly different volatile solubilities, particularly for pure
1475 CO₂ or mixed CO₂-H₂O fluids. Even for melt compositions that are well represented in the calibra-
1476 tion datasets of multiple models (e.g., MORBs), calculated solubilities for pure CO₂ can deviate from
1477 one another by factors of ~ 2 . Differential treatment of H₂O-CO₂ mixing enhances these differences
1478 when calculating volatile solubility for melts containing both volatile species. The solubility of CO₂
1479 predicted by different rhyolitic models also differs substantially, overwhelming other sources of uncer-
1480 tainty such as analytical errors on measurements of volatile contents or uncertainties in crustal density
1481 profiles. Differences are most pronounced for peralkaline rhyolites where there are fewer experimental

1482 constraints. Overall, these comparisons demonstrate that it is vital to pick a model which is calibrated
1483 for the pressure, temperature, and melt composition of interest. Choice of a poorly calibrated model
1484 could introduce a systematic error of a factor of 2 or more in estimates of saturation pressures. This
1485 has widespread implications for published estimates of magma storage depths within volcanic systems,
1486 and indicates that re-evaluation of published magma storage depths calculated using older models may
1487 be warranted.

1488 We also investigate the sensitivity of different models to variation in parameters such as H₂O
1489 content (with relevance to diffusive re-equilibration), CO₂ content (with relevance to melt inclusion
1490 vapour bubble growth), temperature and oxygen fugacity. We suggest that by performing similar sen-
1491 sitivity tests in the future, the uncertainties affecting calculations of volatile solubility in magmatic
1492 systems (and therefore the limitations of each study) can be quantified. We also demonstrate that
1493 isobar diagrams are a poor visualization method for determining magma storage depths in systems
1494 where melt inclusions possess diverse melt inclusion chemistry, so encourage users to take advantage
1495 of the ease and speed of calculations in VESICAL to determine the saturation pressure for each melt
1496 inclusion of interest. These saturation pressures can then be visualized as various cumulative frequency
1497 distributions, histograms, or violin plots, and plotted against melt inclusion H₂O and CO₂ contents,
1498 or parameters relating to host crystal chemistry, to gain greater insight into the factors controlling
1499 magma storage depths within volcanic systems.

1500 Finally, we identify that further experimental constraints are required to accurately estimate
1501 volatile solubility in andesitic-dacitic melts, and that further work is needed to understand the effect of
1502 temperature, redox, and non-ideal mixing between H₂O-CO₂ on volatile solubility.

1504 **Acknowledgments**

1505 PW acknowledges funding from a NERC DTP studentship (NE/L002507/1) and a National Science
1506 Foundation grant (1948862). KI and GMM were supported by the NASA Jacobs JETS Contract
1507 (NNJ13HA01C). We thank Jackie Dixon, Giada Iacono-Marziano, Paolo Papale, and Mark Ghiorso for
1508 help tracking down and using existing calculation tools, and for help constructing model calibration
1509 datasets.

1510 **Data Availability** The jupyter notebooks and associated Excel spreadsheets used to create
1511 the figures in this manuscript are provided as an electronic supplement, as well as being hosted on
1512 the VESICAL github page. Videos showing how to use VESICAL are hosted on YouTube [https://](https://www.youtube.com/channel/UCpvCCs5KMXz0xXWm0seF8Qw)
1513 www.youtube.com/channel/UCpvCCs5KMXz0xXWm0seF8Qw.

1514 **References**

- 1515 Allan, J. F., BATIZA, R., PERFIT, M. R., FORNARI, D. J., & SACK, R. O. (1989). Petrology of
 1516 lavas from the lamont seamount chain and adjacent east pacific rise, 10 n. *Journal of Petrology*,
 1517 *30*(5), 1245–1298.
- 1518 Allison, C. M., Roggensack, K., & Clark, A. (2021). Highly explosive basaltic eruptions driven by co₂
 1519 exsolution. *Nature Communications*.
- 1520 Allison, C. M., Roggensack, K., & Clarke, A. B. (2019). H₂O–CO₂ solubility in alkali-rich mafic
 1521 magmas: new experiments at mid-crustal pressures. *Contributions to Mineralogy and Petrology*,
 1522 *174*(7), 58.
- 1523 Aster, E. M., Wallace, P. J., Moore, L. R., Watkins, J., Gazel, E., & Bodnar, R. J. (2016). Recon-
 1524 structing CO₂ concentrations in basaltic melt inclusions using raman analysis of vapor bubbles.
 1525 *Journal of Volcanology and Geothermal Research*, *323*, 148–162.
- 1526 Atlas, Z. D., Dixon, J. E., Sen, G., Finny, M., & Martin-Del Pozzo, A. L. (2006). Melt inclusions from
 1527 volcán popocatepetl and volcán de colima, mexico: melt evolution due to vapor-saturated crys-
 1528 tallization during ascent. *Journal of Volcanology and Geothermal Research*, *153*(3-4), 221–240.
- 1529 Behrens, H., Ohlhorst, S., Holtz, F., & Champenois, M. (2004). CO₂ solubility in dacitic melts
 1530 equilibrated with H₂O–CO₂ fluids: Implications for modeling the solubility of CO₂ in silicic melts.
 1531 *Geochimica et Cosmochimica Acta*, *68*(22), 4687–4703.
- 1532 Blank, J., Stolper, E., & Carroll, M. (1993). Solubilities of carbon dioxide and water in rhyolitic melt
 1533 at 850 c and 750 bars. *Earth and Planetary Science Letters*, *119*(1-2), 27–36.
- 1534 Blundy, J., & Cashman, K. (2005). Rapid decompression-driven crystallization recorded by melt inclu-
 1535 sions from mount st. helens volcano. *Geology*, *33*(10), 793–796.
- 1536 Blundy, J., Cashman, K., & Humphreys, M. (2006). Magma heating by decompression-driven crystal-
 1537 lization beneath andesite volcanoes. *Nature*, *443*(7107), 76–80.
- 1538 Botcharnikov, R. E., Behrens, H., & Holtz, F. (2006). Solubility and speciation of C–O–H fluids in an-
 1539 desitic melt at T= 1100–1300 c and P= 200 and 500 mpa. *Chemical Geology*, *229*(1-3), 125–143.
- 1540 Botcharnikov, R. E., Holtz, F., & Behrens, H. (2007). The effect of CO₂ on the solubility of H₂O–Cl flu-
 1541 ids in andesitic melt. *European Journal of Mineralogy*, *19*(5), 671–680.
- 1542 Bowen, N. (1928). The evolution of the igneous rocks, princeton, univ. Press, Princeton, New Jersey.
- 1543 Brooker, R., Kohn, S., Holloway, J., & McMillan, P. (2001). Structural controls on the solubility of CO₂
 1544 in silicate melts: part i: bulk solubility data. *Chemical Geology*, *174*(1-3), 225–239.
- 1545 Bucholz, C. E., Gaetani, G. A., Behn, M. D., & Shimizu, N. (2013). Post-entrapment modification of
 1546 volatiles and oxygen fugacity in olivine-hosted melt inclusions. *Earth and Planetary Science Let-*

- 1547 ters, *374*, 145–155.
- 1548 Bureau, H., & Keppler, H. (1999). Complete miscibility between silicate melts and hydrous fluids in
1549 the upper mantle: experimental evidence and geochemical implications. *Earth and Planetary Sci-*
1550 *ence Letters*, *165*(2), 187–196.
- 1551 Burgisser, A., Alletti, M., & Scaillet, B. (2015). Simulating the behavior of volatiles belonging to the
1552 c–o–h–s system in silicate melts under magmatic conditions with the software d-compress. *Com-*
1553 *puters & Geosciences*, *79*, 1–14.
- 1554 Burnham, C. W. (1979). The importance of volatile constituents. *The evolution of the igneous rocks*,
1555 439–482.
- 1556 Burnham, C. W., & Davis, N. (1971). The role of h₂o in silicate melts; i, pvt relations in the sys-
1557 tem naalsi 3 o 8-h₂o to 10 kilobars and 1000 degrees c. *American Journal of Science*, *270*(1),
1558 54–79.
- 1559 Burnham, C. W., & Davis, N. (1974). The role of h₂o in silicate melts; ii, thermodynamic and phase
1560 relations in the system naalsi 3 o 8-h₂o to 10 kilobars, 700 degrees to 1100 degrees c. *American*
1561 *Journal of Science*, *274*(8), 902–940.
- 1562 Cassidy, M., Edmonds, M., Watt, S. F., Palmer, M. R., & Gernon, T. M. (2015). Origin of basalts by
1563 hybridization in andesite-dominated arcs. *Journal of Petrology*, *56*(2), 325–346.
- 1564 Cocheo, P., & Holloway, J. (1993). The solubility of h₂o in basanitic melts at low pressure. *EOS*
1565 *Transactions of the American Geophysical Union* *74*.
- 1566 Cottrell, E., Lanzirotti, A., Mysen, B., Birner, S., Kelley, K. A., Botcharnikov, R., . . . Newville, M.
1567 (2018). A mössbauer-based xanes calibration for hydrous basalt glasses reveals radiation-induced
1568 oxidation of fe. *American Mineralogist: Journal of Earth and Planetary Materials*, *103*(4),
1569 489–501.
- 1570 Dingwell, D. B. (1986). Volatile solubilities in silicate melts.
- 1571 Dixon, J. E. (1997). Degassing of alkalic basalts. *American Mineralogist*, *82*(3-4), 368–378.
- 1572 Dixon, J. E., Stolper, E. M., & Holloway, J. R. (1995). An experimental study of water and carbon
1573 dioxide solubilities in mid-ocean ridge basaltic liquids. part i: calibration and solubility models.
1574 *Journal of Petrology*, *36*(6), 1607–1631.
- 1575 Duan, X. (2014). A general model for predicting the solubility behavior of h₂o–co₂ fluids in silicate
1576 melts over a wide range of pressure, temperature and compositions. *Geochimica et Cosmochimica*
1577 *Acta*, *125*, 582–609.
- 1578 Duan, Z., & Zhang, Z. (2006). Equation of state of the h₂o, co₂, and h₂o–co₂ systems up to 10 gpa
1579 and 2573.15 k: Molecular dynamics simulations with ab initio potential surface. *Geochimica et*

- 1580 *cosmochimica acta*, 70(9), 2311–2324.
- 1581 Egger, D. (1973). Role of co₂ in melting processes in the mantle. *Carnegie Inst. Wash. Yearb*, 72,
1582 457–467.
- 1583 Eguchi, J., & Dasgupta, R. (2018). A co₂ solubility model for silicate melts from fluid saturation to
1584 graphite or diamond saturation. *Chemical Geology*, 487, 23–38.
- 1585 Fine, G., & Stolper, E. (1986). Dissolved carbon dioxide in basaltic glasses: concentrations and specia-
1586 tion. *Earth and Planetary Science Letters*, 76(3-4), 263–278.
- 1587 Flowers, G. C. (1979). Correction of holloway’s (1977) adaptation of the modified redlich-kwong equa-
1588 tion of state for calculation of the fugacities of molecular species in supercritical fluids of geologic
1589 interest. *Contributions to Mineralogy and Petrology*, 69(3), 315–318.
- 1590 Fogel, R. A., & Rutherford, M. J. (1990). The solubility of carbon dioxide in rhyolitic melts; a quanti-
1591 tative ftir study. *American Mineralogist*, 75(11-12), 1311–1326.
- 1592 Freise, M. (2004). *Differenzierung von basalten einer “large igneous province” am beispiel des kergue-*
1593 *len plateaus. eine experimentelle studie* (Unpublished doctoral dissertation). PhD thesis, Univer-
1594 sity of Hannover.
- 1595 Gaborieau, M., Laubier, M., Bolfan-Casanova, N., Mccammon, C., Vantelon, D., Chumakov, A.,
1596 ... Venugopal, S. (2020). Determination of fe³⁺/σfe of olivine-hosted melt inclusions using
1597 mössbauer and xanes spectroscopy. *Chemical Geology*, 119646.
- 1598 Gaetani, G. A., O’Leary, J. A., Shimizu, N., Bucholz, C. E., & Newville, M. (2012). Rapid reequilibra-
1599 tion of h₂o and oxygen fugacity in olivine-hosted melt inclusions. *Geology*, 40(10), 915–918.
- 1600 Gavrilenko, M., Krawczynski, M., Ruprecht, P., Li, W., & Catalano, J. G. (2019). The quench control
1601 of water estimates in convergent margin magmas. *American Mineralogist: Journal of Earth and*
1602 *Planetary Materials*, 104(7), 936–948.
- 1603 Gerlach, T. M. (1986). Exsolution of h₂o, co₂, and s during eruptive episodes at kilauea volcano,
1604 hawaii. *Journal of Geophysical Research: Solid Earth*, 91(B12), 12177–12185.
- 1605 Ghiorso, M. S., Carmichael, I. S., Rivers, M. L., & Sack, R. O. (1983). The gibbs free energy of mix-
1606 ing of natural silicate liquids; an expanded regular solution approximation for the calculation of
1607 magmatic intensive variables. *Contributions to Mineralogy and Petrology*, 84(2), 107–145.
- 1608 Ghiorso, M. S., & Gualda, G. A. (2015). An h₂o–co₂ mixed fluid saturation model compatible with
1609 rhyolite-melts. *Contributions to Mineralogy and Petrology*, 169(6), 1–30.
- 1610 Ghiorso, M. S., & Sack, R. O. (1995). Chemical mass transfer in magmatic processes iv. a revised
1611 and internally consistent thermodynamic model for the interpolation and extrapolation of liquid-
1612 solid equilibria in magmatic systems at elevated temperatures and pressures. *Contributions to*

- 1613 *Mineralogy and Petrology*, 119(2-3), 197–212.
- 1614 Ghiorso, M. S., & Sverjensky, D. A. (2016). The melts-dew connection: Integration of thermodynamic
1615 models for magmatic systems and aqueous fluids at elevated temperatures and pressures. In *Agu*
1616 *fall meeting abstracts* (Vol. 2016, pp. V33H–04).
- 1617 Gleeson, M. L., Gibson, S. A., & Williams, H. M. (2020). Novel insights from Fe-isotopes into the
1618 lithological heterogeneity of ocean island basalts and plume-influenced morbs. *Earth and Plane-*
1619 *tary Science Letters*, 535, 116114.
- 1620 Gleeson, M. L., Stock, M. J., Pyle, D. M., Mather, T. A., Hutchison, W., Yirgu, G., & Wade, J.
1621 (2017). Constraining magma storage conditions at a restless volcano in the main Ethiopian
1622 rift using phase equilibria models. *Journal of Volcanology and Geothermal Research*, 337, 44–61.
- 1623 Goltz, A. E., Krawczynski, M. J., Gavrilenko, M., Gorbach, N. V., & Ruprecht, P. (2020). Evidence
1624 for superhydrous primitive arc magmas from mafic enclaves at Shiveluch volcano, Kamchatka.
1625 *Contributions to Mineralogy and Petrology*, 175(12), 1–26.
- 1626 Goranson, R. W. (1931). Solubility of water in granite magmas. *Eos, Transactions American Geophys-*
1627 *ical Union*, 12(1), 183–183.
- 1628 Gualda, G. A., & Ghiorso, M. S. (2015). Melts _ e xcel: An Microsoft Excel-based melts interface for re-
1629 search and teaching of magma properties and evolution. *Geochemistry, Geophysics, Geosystems*,
1630 16(1), 315–324.
- 1631 Gualda, G. A., Ghiorso, M. S., Lemons, R. V., & Carley, T. L. (2012). Rhyolite-melts: a modified cal-
1632 ibration of melts optimized for silica-rich, fluid-bearing magmatic systems. *Journal of Petrology*,
1633 53(5), 875–890.
- 1634 Hamilton, D., Burnham, C. W., & Osborn, E. (1964). The solubility of water and effects of oxygen fu-
1635 gacity and water content on crystallization in mafic magmas. *Journal of Petrology*, 5(1), 21–39.
- 1636 Hartley, M. E., MacLennan, J., Edmonds, M., & Thordarson, T. (2014). Reconstructing the deep CO₂
1637 degassing behaviour of large basaltic fissure eruptions. *Earth and Planetary Science Letters*, 393,
1638 120–131.
- 1639 Hartley, M. E., Neave, D. A., MacLennan, J., Edmonds, M., & Thordarson, T. (2015). Diffusive over-
1640 hydration of olivine-hosted melt inclusions. *Earth and Planetary Science Letters*, 425, 168–178.
- 1641 Hauri, E. (2002). SIMS analysis of volatiles in silicate glasses, 2: isotopes and abundances in Hawaiian
1642 melt inclusions. *Chemical Geology*, 183(1-4), 115–141.
- 1643 Hauri, E., Kent, A. J., & Arndt, N. (2002). Melt inclusions at the millennium: toward a deeper under-
1644 standing of magmatic processes. *ChGeo*, 183(1-4), 1–3.
- 1645 Hervig, R., Dunbar, N., Westrich, H. R., & Kyle, P. R. (1989). Pre-eruptive water content of rhyolitic

- 1646 magmas as determined by ion microprobe analyses of melt inclusions in phenocrysts. *Journal of*
1647 *Volcanology and Geothermal Research*, 36(4), 293–302.
- 1648 Hervig, R., & Williams, P. (1988). Sims microanalysis of minerals and glasses for h and d. *SIMS VI*
1649 *Proceedings*, 961–964.
- 1650 Hess, K., & Dingwell, D. (1996). Viscosities of hydrous leucogranitic melts: A non-arrhenian model.
1651 *American Mineralogist*, 81(9-10), 1297–1300.
- 1652 Holloway, J. R. (1977). Fugacity and activity of molecular species in supercritical fluids. In *Thermody-*
1653 *namics in geology* (pp. 161–181). Springer.
- 1654 Holloway, J. R., & Blank, J. G. (1994). Application of experimental results to coh species in natural
1655 melts. *Reviews in mineralogy*, 30, 187–187.
- 1656 Huang, F., & Sverjensky, D. A. (2019). Extended deep earth water model for predicting major element
1657 mantle metasomatism. *Geochimica et Cosmochimica Acta*, 254, 192–230.
- 1658 Huber, C., Townsend, M., Degruyter, W., & Bachmann, O. (2019). Optimal depth of subvolcanic
1659 magma chamber growth controlled by volatiles and crust rheology. *Nature Geoscience*, 12(9),
1660 762–768.
- 1661 Huppert, H. E., & Woods, A. W. (2002). The role of volatiles in magma chamber dynamics. *Nature*,
1662 420(6915), 493–495.
- 1663 Husen, A., Almeev, R. R., & Holtz, F. (2016). The effect of h₂o and pressure on multiple saturation
1664 and liquid lines of descent in basalt from the shatsky rise. *Journal of Petrology*, 57(2), 309–344.
- 1665 Iacono-Marziano, G., Morizet, Y., Le Trong, E., & Gaillard, F. (2012). New experimental data and
1666 semi-empirical parameterization of h₂o–co₂ solubility in mafic melts. *Geochimica et Cosmochim-*
1667 *ica Acta*, 97, 1–23.
- 1668 Iacovino, K., Matthews, S., Wieser, P. E., Moore, G., & Begue, F. (2021). Vesical part i: An open
1669 source thermodynamic model engine for mixed volatile solubility in silicate melts. *EarthArxiv* -
1670 <https://doi.org/10.31223/X5D606>.
- 1671 Iacovino, K., Moore, G., Roggensack, K., Oppenheimer, C., & Kyle, P. (2013). H₂o–co₂ solubility in
1672 mafic alkaline magma: applications to volatile sources and degassing behavior at erebus volcano,
1673 antarctica. *Contributions to Mineralogy and Petrology*, 166(3), 845–860.
- 1674 Iddon, F., & Edmonds, M. (2020). Volatile-rich magmas distributed through the upper crust in the
1675 main ethiopian rift. *Geochemistry, Geophysics, Geosystems*, 21(6), e2019GC008904.
- 1676 Jakobsson, S. (1997). Solubility of water and carbon dioxide in an icelandite at 1400 c and 10 kilobars.
1677 *Contributions to Mineralogy and Petrology*, 127(1-2), 129–135.
- 1678 Kerrick, D., & Jacobs, G. (1981). A modified redlich-kwong equation for h₂o, co₂, and h₂o-co

- 1679 2 mixtures at elevated pressures and temperatures. *American Journal of Science*, 281(6), 735–
1680 767.
- 1681 King, P., & Holloway, J. (2002). Co₂ solubility and speciation in intermediate (andesitic) melts: the
1682 role of h₂o and composition. *Geochimica et Cosmochimica Acta*, 66(9), 1627–1640.
- 1683 Koleszar, A., Kent, A. J., Wallace, P. J., & Scott, W. E. (2012). Controls on long-term low explo-
1684 sivity at andesitic arc volcanoes: Insights from mount hood, oregon. *Journal of Volcanology and
1685 Geothermal Research*, 219, 1–14.
- 1686 Koleszar, A., Saal, A., Hauri, E., Nagle, A., Liang, Y., & Kurz, M. (2009). The volatile contents of
1687 the galapagos plume; evidence for h₂o and f open system behavior in melt inclusions. *Earth and
1688 Planetary Science Letters*, 287(3-4), 442–452.
- 1689 Lesne, P., Scaillet, B., Pichavant, M., & Beny, J.-M. (2011). The carbon dioxide solubility in alkali
1690 basalts: an experimental study. *Contributions to Mineralogy and Petrology*, 162(1), 153–168.
- 1691 Lesne, P., Scaillet, B., Pichavant, M., Iacono-Marziano, G., & Beny, J.-M. (2011). The h₂o solu-
1692 bility of alkali basaltic melts: an experimental study. *Contributions to Mineralogy and Petrology*,
1693 162(1), 133–151.
- 1694 Le Voyer, M., Hauri, E., Cottrell, E., Kelley, K. A., Salters, V. J., Langmuir, C. H., . . . Füre, E.
1695 (2019). Carbon fluxes and primary magma co₂ contents along the global mid-ocean ridge system.
1696 *Geochemistry, Geophysics, Geosystems*, 20(3), 1387–1424.
- 1697 Li, Y., Dasgupta, R., & Tsuno, K. (2017). Carbon contents in reduced basalts at graphite saturation:
1698 Implications for the degassing of mars, mercury, and the moon. *Journal of Geophysical Research:
1699 Planets*, 122(6), 1300–1320.
- 1700 Liu, Y., Zhang, Y., & Behrens, H. (2005). Solubility of h₂o in rhyolitic melts at low pressures and a
1701 new empirical model for mixed h₂o–co₂ solubility in rhyolitic melts. *Journal of Volcanology and
1702 Geothermal Research*, 143(1-3), 219–235.
- 1703 Lloyd, A. S., Plank, T., Ruprecht, P., Hauri, E., & Rose, W. (2013). Volatile loss from melt inclusions
1704 in pyroclasts of differing sizes. *Contributions to Mineralogy and Petrology*, 165(1), 129–153.
- 1705 Lowenstern, J. B. (1995). Applications of silicate-melt inclusions to the study of magmatic volatiles.
1706 *Magma, fluids and ore deposits*, 23, 71–99.
- 1707 Lowenstern, J. B. (2001). Carbon dioxide in magmas and implications for hydrothermal systems. *Min-
1708 eralium Deposita*, 36(6), 490–502.
- 1709 Lowenstern, J. B. (2003). Melt inclusions come of age: volatiles, volcanoes, and sorby’s legacy. In *De-
1710 velopments in volcanology* (Vol. 5, pp. 1–21). Elsevier.
- 1711 Lucic, G., Berg, A.-S., & Stix, J. (2016). Water-rich and volatile-undersaturated magmas at hekla vol-

- 1712 cano, iceland. *Geochemistry, Geophysics, Geosystems*, *17*(8), 3111–3130.
- 1713 MacLennan, J. (2017). Bubble formation and decrepitation control the CO₂ content of olivine-hosted
1714 melt inclusions. *Geochemistry, Geophysics, Geosystems*, *18*(2), 597–616.
- 1715 Makhluף, A. R., Newton, R., & Manning, C. (2020). Experimental investigation of phase relations
1716 in the system NaAlSi₃O₈–H₂O at high temperatures and pressures: liquidus relations, liquid–
1717 vapor mixing, and critical phenomena at deep crust–upper mantle conditions. *Contributions to
1718 Mineralogy and Petrology*, *175*(8), 1–20.
- 1719 Mangan, M. T., Sisson, T. W., Hankins, W. B., Shimizu, N., & Vennemann, T. (2021). Constraints
1720 on deep, CO₂-rich degassing at arc volcanoes from solubility experiments on hydrous basaltic an-
1721 desite of Pavlof volcano, Alaska peninsula, at 300 to 1200 MPa. *American Mineralogist: Journal
1722 of Earth and Planetary Materials*, *106*(5), 762–773.
- 1723 Métrich, N., & Wallace, P. J. (2008). Volatile abundances in basaltic magmas and their degassing
1724 paths tracked by melt inclusions. *Reviews in Mineralogy and Geochemistry*, *69*(1), 363–402.
- 1725 Mironov, N., Tobelko, D., Smirnov, S., Portnyagin, M. V., & Krasheninnikov, S. (2020). Estimation
1726 of CO₂ content in the gas phase of melt inclusions using Raman spectroscopy: Case study of in-
1727 clusions in olivine from the Karymsky volcano (Kamchatka). *Russian Geology and Geophysics*,
1728 *61*(5-6), 600–610.
- 1729 Mitchell, A. L., Gaetani, G. A., O’Leary, J. A., & Hauri, E. H. (2017). H₂O solubility in basalt at up-
1730 per mantle conditions. *Contributions to Mineralogy and Petrology*, *172*(10), 1–16.
- 1731 Moore, G. (2008). Interpreting H₂O and CO₂ contents in melt inclusions: constraints from solubility ex-
1732 periments and modeling. *Reviews in Mineralogy and Geochemistry*, *69*(1), 333–362.
- 1733 Moore, G., & Carmichael, I. (1998). The hydrous phase equilibria (to 3 kbar) of an andesite and
1734 basaltic andesite from western Mexico: constraints on water content and conditions of phenocryst
1735 growth. *Contributions to Mineralogy and Petrology*, *130*(3-4), 304–319.
- 1736 Moore, G., Roggensack, K., & Klonowski, S. (2008). A low-pressure–high-temperature technique for
1737 the piston-cylinder. *American Mineralogist*, *93*(1), 48–52.
- 1738 Moore, G., Vennemann, T., & Carmichael, I. (1998). An empirical model for the solubility of H₂O in
1739 magmas to 3 kilobars. *American Mineralogist*, *83*(1), 36–42.
- 1740 Moore, L. R., Gazel, E., Tuohy, R., Lloyd, A. S., Esposito, R., Steele-MacInnis, M., . . . Bodnar, R. J.
1741 (2015). Bubbles matter: An assessment of the contribution of vapor bubbles to melt inclusion
1742 volatile budgets. *American Mineralogist*, *100*(4), 806–823.
- 1743 Mutch, E. J., MacLennan, J., Shorttle, O., Edmonds, M., & Rudge, J. F. (2019). Rapid transcrustal
1744 magma movement under Iceland. *Nature Geoscience*, *12*(7), 569–574.

- 1745 Mysen, B. O. (1976). The role of volatiles in silicate melts; solubility of carbon dioxide and water in
1746 feldspar, pyroxene, and feldspathoid melts to 30 kb and 1625 degrees c. *American Journal of Sci-*
1747 *ence*, 276(8), 969–996.
- 1748 Mysen, B. O., Eggler, D. H., Seitz, M., & Holloway, J. R. (1976). Carbon dioxide in silicate melts and
1749 crystals; part i, solubility measurements. *American Journal of Science*, 276(4), 455–479.
- 1750 Mysen, B. O., Fogel, M. L., Morrill, P. L., & Cody, G. D. (2009). Solution behavior of reduced coh
1751 volatiles in silicate melts at high pressure and temperature. *Geochimica et Cosmochimica Acta*,
1752 73(6), 1696–1710.
- 1753 Newman, S., & Lowenstern, J. B. (2002). Volatilecalc: a silicate melt–h₂o–co₂ solution model written
1754 in visual basic for excel. *Computers & Geosciences*, 28(5), 597–604.
- 1755 Ochs, F. A., & Lange, R. A. (1999). The density of hydrous magmatic liquids. *Science*, 283(5406),
1756 1314–1317.
- 1757 Paonita, A., Gigli, G., Gozzi, D., Nuccio, P., & Trigila, R. (2000). Investigation of the he solubility
1758 in h₂o–co₂ bearing silicate liquids at moderate pressure: a new experimental method. *Earth and*
1759 *Planetary Science Letters*, 181(4), 595–604.
- 1760 Papale, P. (1997). Modeling of the solubility of a one-component h₂o or co₂ fluid in silicate liquids.
1761 *Contributions to Mineralogy and Petrology*, 126(3), 237–251.
- 1762 Papale, P. (1999). Modeling of the solubility of a two-component h₂o+ co₂ fluid in silicate liquids.
1763 *American Mineralogist*, 84(4), 477–492.
- 1764 Papale, P., Moretti, R., & Barbato, D. (2006). The compositional dependence of the saturation surface
1765 of h₂o+ co₂ fluids in silicate melts. *Chemical Geology*, 229(1-3), 78–95.
- 1766 Papale, P., Neri, A., & Macedonio, G. (1999). The role of water content and magma composition
1767 on explosive eruption dynamics. *Physics and Chemistry of the Earth, Part A: Solid Earth and*
1768 *Geodesy*, 24(11-12), 969–975.
- 1769 Plank, T., Kelley, K. A., Zimmer, M. M., Hauri, E., & Wallace, P. J. (2013). Why do mafic arc mag-
1770 mas contain 4 wt% water on average? *Earth and Planetary Science Letters*, 364, 168–179.
- 1771 Portnyagin, M., Almeev, R., Matveev, S., & Holtz, F. (2008). Experimental evidence for rapid water
1772 exchange between melt inclusions in olivine and host magma. *Earth and Planetary Science Let-*
1773 *ters*, 272(3-4), 541–552.
- 1774 Putirka, K. D. (2008). Thermometers and barometers for volcanic systems. *Reviews in Mineralogy and*
1775 *Geochemistry*, 69(1), 61–120.
- 1776 Rasmussen, D. J., Plank, T. A., Wallace, P. J., Newcombe, M. E., & Lowenstern, J. B. (2020). Vapor-
1777 bubble growth in olivine-hosted melt inclusions. *American Mineralogist: Journal of Earth and*

- 1778 *Planetary Materials*, 105(12), 1898–1919.
- 1779 Reubi, O., & Blundy, J. (2009). A dearth of intermediate melts at subduction zone volcanoes and the
1780 petrogenesis of arc andesites. *Nature*, 461(7268), 1269–1273.
- 1781 Roggensack, K. (2001). Unraveling the 1974 eruption of fuego volcano (guatemala) with small crystals
1782 and their young melt inclusions. *Geology*, 29(10), 911–914.
- 1783 Rohatgi, A. (2017). *Webplotdigitizer*. Austin, Texas, USA.
- 1784 Saal, A. E., Hauri, E., Langmuir, C. H., & Perfit, M. R. (2002). Vapour undersaturation in primitive
1785 mid-ocean-ridge basalt and the volatile content of earth’s upper mantle. *Nature*, 419(6906), 451–
1786 455.
- 1787 Shishkina, T., Botcharnikov, R. E., Holtz, F., Almeev, R., & Portnyagin, M. V. (2010). Solubility
1788 of h₂o-and co₂-bearing fluids in tholeiitic basalts at pressures up to 500 mpa. *Chemical geology*,
1789 277(1-2), 115–125.
- 1790 Shishkina, T., Botcharnikov, R. E., Holtz, F., Almeev, R. R., Jazwa, A. M., & Jakubiak, A. A. (2014).
1791 Compositional and pressure effects on the solubility of h₂o and co₂ in mafic melts. *Chemical Ge-*
1792 *ology*, 388, 112–129.
- 1793 Sides, I., Edmonds, M., MacLennan, J., Swanson, D., & Houghton, B. (2014a). Eruption style at
1794 kīlauea volcano in hawaii ‘i linked to primary melt composition. *Nature Geoscience*, 7(6), 464.
- 1795 Sides, I., Edmonds, M., MacLennan, J., Swanson, D., & Houghton, B. (2014b). Magma mixing and
1796 high fountaining during the 1959 kīlauea iki eruption, hawaii ‘i. *Earth and Planetary Science Let-*
1797 *ters*, 400, 102–112.
- 1798 Silver, L. A. (1988). *Water in silicate glasses* (Unpublished doctoral dissertation). California Institute
1799 of Technology.
- 1800 Silver, L. A., Ihinger, P. D., & Stolper, E. (1990). The influence of bulk composition on the speciation
1801 of water in silicate glasses. *Contributions to Mineralogy and Petrology*, 104(2), 142–162.
- 1802 Silver, L. A., & Stolper, E. (1989). Water in albitic glasses. *Journal of petrology*, 30(3), 667–709.
- 1803 Steele-Macinnis, M., Esposito, R., & Bodnar, R. J. (2011). Thermodynamic model for the effect
1804 of post-entrapment crystallization on the h₂o–co₂ systematics of vapor-saturated, silicate melt
1805 inclusions. *Journal of Petrology*, 52(12), 2461–2482.
- 1806 Stevenson, J. (2015). *Tasplot*. <https://bitbucket.org/jsteven5/tasplot/src/master/>. bitbucket.
- 1807 Stolper, E. (1982). Water in silicate glasses: an infrared spectroscopic study. *Contributions to Mineral-*
1808 *ogy and Petrology*, 81(1), 1–17.
- 1809 Stolper, E., Fine, G., Johnson, T., & Newman, S. (1987). Solubility of carbon dioxide in albitic melt.
1810 *American Mineralogist*, 72(11-12), 1071–1085.

- 1811 Sverjensky, D. A., Harrison, B., & Azzolini, D. (2014). Water in the deep earth: the dielectric constant
1812 and the solubilities of quartz and corundum to 60 kb and 1200 c. *Geochimica et Cosmochimica*
1813 *Acta*, *129*, 125–145.
- 1814 Tamura, Y., & Tatsumi, Y. (2002). Remelting of an andesitic crust as a possible origin for rhyolitic
1815 magma in oceanic arcs: an example from the Izu–Bonin arc. *Journal of Petrology*, *43*(6), 1029–
1816 1047.
- 1817 Tucker, J. M., Hauri, E., Pietruszka, A. J., Garcia, M. O., Marske, J. P., & Trusdell, F. A. (2019). A
1818 high carbon content of the Hawaiian mantle from olivine-hosted melt inclusions. *Geochimica et*
1819 *Cosmochimica Acta*, *254*, 156–172.
- 1820 Tuttle, O. F., & Bowen, N. L. (1958). *Origin of granite in the light of experimental studies in the sys-*
1821 *tem NaAlSi₃O₈-KAlSi₃O₈-SiO₂-H₂O* (Vol. 74). Geological Society of America.
- 1822 Venugopal, S., Schiavi, F., Moune, S., Bolfan-Casanova, N., Druitt, T., & Williams-Jones, G. (2020).
1823 Melt inclusion vapour bubbles: the hidden reservoir for major and volatile elements. *Scientific*
1824 *Reports*, *10*(1), 1–14.
- 1825 Wallace, P. J., Anderson, A. T., & Davis, A. M. (1995). Quantification of pre-eruptive exsolved gas
1826 contents in silicic magmas. *Nature*, *377*(6550), 612–616.
- 1827 Waters, L. E., & Lange, R. A. (2013). Crystal-poor, multiply saturated rhyolites (obsidians) from the
1828 cascade and Mexican arcs: evidence of degassing-induced crystallization of phenocrysts. *Contri-*
1829 *butions to Mineralogy and Petrology*, *166*(3), 731–754.
- 1830 Waters, L. E., & Lange, R. A. (2015). An updated calibration of the plagioclase-liquid hygrometer-
1831 thermometer applicable to basalts through rhyolites. *American Mineralogist*, *100*(10), 2172–
1832 2184.
- 1833 Wieser, P. E., Lamadrid, H., MacLennan, J., Edmonds, M., Matthews, S., Iacovino, K., . . . Ilyinskaya,
1834 E. (2020). Reconstructing magma storage depths for the 2018 Kilauean eruption from melt inclu-
1835 sion CO₂ contents: The importance of vapor bubbles. *Geochemistry, Geophysics, Geosystems*.